# Development and Optimisation of Patterned Optical Immunosensors

By

Helen McEvoy B.Sc. (Hons)

A Thesis presented

to

Dublin City University

For The Degree Of Doctor Of Philosophy

Research Supervisor:

Dr. Colette McDonagh,

School of Physical Sciences,

Dublin City University.

June 2005

## Declaration

I hereby certify that this material, which I now submit for assessment on the programme of study leading to the award of Doctor of Philosophy is entirely my own work and has not been taken from the work of others save and to the extent that such work has been cited and acknowledged within the text of my work.

Signed: Helen M'Evoy (Candidate) ID No.: 99145278

Date: 31/08/05

# Acknowledgements

First and foremost, I wish to thank my supervisor, Dr. Colette McDonagh, for her constant guidance and encouragement during these past few years. I am extremely grateful to you and could not have wished for a more supportive supervisor. I would also like to thank Prof. Brian MacCraith for his invaluable input and assistance with the project direction. Thank you to you both for allowing me this fantastic opportunity.

For creating such an inspiring and enjoyable working atmosphere, I want to thank all the members of the Optical Sensors Laboratory, past and present, in particular Aisling, Kieran, Pat, Jean-Marc, Christoph, Phil, Honza, Henry, John, Ondra, Orla, Adam, Rob and Lionel. Special thanks are due to Bob and Dave all for their input, especially with all things camera and cones related.

I especially want to thank Nigel and Des for all the machining and fabrication. Without the set-ups and chips, this work could not have happened. You both always managed to produce more than I hoped for and quicker than I expected.

Thanks are also due to Lubos Polerecky for his assistance with the design and analysis of the theory verification experiments. I learnt an incredible amount from you. Thanks for your time and patience.

To Carol Lynam, it was great fun (and thankfully productive) working with you. Thanks for putting up with my constant chemistry questions. Thanks to Shannon for this too!

A big thank you is due to the members of Prof. Richard O'Kennedy's group, especially John Quinn, Paul Dillon and Paul Leonard, for their patient instruction and assistance. Thank you for helping to make the collaboration so successful.

I also wish to thank the other members of the NCSR and School of Physical Sciences who have helped make the past few years so productive and enjoyable.

To my friends outside of DCU, thank you all for putting up with my long hours and lack of finance for so long. I promise to be more sociable again now!

The people who really ensured I survived these past years are my family. To my parents and Keith, Paul, Neil, Susan, Ciara (and Mick!), thank you for looking after, supporting and encouraging me. I could never have made it without you.

And finally, to the person who helped more than any other, to Conor, thank you for everything.

# Contents

# Abstract

This work describes the successful design, fabrication and implementation of a generic, optimised immunosensor. The first stage of the work was the establishment of the techniques required to develop an effective immunosensor, in particular, antibody immobilisation strategies, patterning methods and excitation, detection and analysis systems. Once developed, these techniques were integrated and employed, in conjunction with a planar glass substrate, to obtain dose response curves for BSA/antiBSA antibody assays.

In parallel work, theoretical predictions relating to fluorescence emission were verified. It was shown that redirection of surface-confined fluorescence results in the enhancement of the fluorescence capture efficiency, and also that it is possible to discriminate between fluorescence originating at the surface and fluorescence originating from the bulk solution above the surface. These results have important implications for the design of fluorescence-based optical sensor platforms and were used in the design and fabrication of structured polymer biochips with enhanced fluorescence capture efficiency.

The final stage of the work presented here was the incorporation of the structured platforms with the immunosensing systems established previously, in order to produce an optimised, generic, optical immunosensor. The replacement of the planar glass substrate with the enhanced polymer platform necessitated the adaptation of several of the systems. In particular, various antibody to polymer immobilisation strategies were investigated, with the optimum used to perform a full BSA/antiBSA antibody assay. A minimum detectable signal considerably lower than that of the planar immunosensor was achieved, thus validating the optimisations. The ability of this enhanced immunosensor to detect significantly lower levels of fluorescence has important implications for sensing applications where analytes are toxic in low concentrations or are only available in small quantities, with these situations occurring in a wide range of areas including health care, food safety and early-warning biological warfare agent detection.

# Chapter 1

# Introduction

## 1.1 Introduction: From Immunology to Immunosensors

Immunisation, as a preventative measure against disease, was first practised over 2500 years ago, with the Chinese inoculating healthy people with extracts from the pustules of those suffering from smallpox [1]. However, it wasn't until 1718 that this practice was first carried out in Europe and it was several years later before it was introduced in America [1]. Even at this stage, the practice remained purely empirical as the scientific community lacked fundamental knowledge of biological systems.

It was almost a century later, in the 1870's, before immunology, the field of science concerned with the immune system, was founded. This was led by the work of Louis Pasteur and Elia Metchnikoff. Pasteur demonstrated the existence of microorganisms and applied systematic immunisation to chickens and cows [2]. Metchnikoff, Pasteur's successor at the Pasteur Institute, Paris, is often referred to as the father of immunology due to his discovery that particular cells, which he termed phagocytes, destroy foreign bodies, such as bacteria [3].

The body of immunological knowledge did not increase significantly until the twentieth century, when immunology began to contribute in a very real manner to modern medicine. A prime example of this was the discovery of blood groups by Karl Lansteiner, which directly led to the reduction of the major risks associated with blood transfusion incompatibility. Lansteiner was also part of the scientific

community that, in the 1930s, began to isolate, purify and identify antibodies as an integral part of a body's immune system. Furthermore, he demonstrated that these antibodies were capable of discriminating between small differences in molecular structure. His work showed that antibody recognition of molecules involved the shape, composition and spatial arrangement of the molecules' functional groups [4]. Through the 1940's, 50's and 60's, a detailed picture of antibody recognition and antigen binding (an antigen being the molecule recognised by the antibody) was built by Pauling, Pressman, Kabat and others [5–7]. It was clear that the antibody/antigen binding mechanism was extremely selective, marking them as highly attractive sensing agents. Therefore, in the 1970's, research into the use of antibodies to detect and quantify antigens (an area referred to as immunoassays) expanded rapidly [8]. This ultimately resulted in the widespread employment of immunoassays in current-day clinical laboratories [9].

Immunosensors refer to devices in which antibodies or antigens are coupled to a signal transducer that detects the binding of the two molecules. Combined with the volume of immunoassay research being carried out, the publication of a paper by Nylander et al. in 1982 led the way for the first major commercial immunosensor: the Pharmacia BIACore SPR-based biosensor system [10]. This system was launched in 1990 and remains one of just a small number of commercially successful immunosensors. The potential benefits of immunosensors, for example in rapid point-of-care diagnosis, certainly make them worthy of development. However, immunosensor research is still quite a new area, as is apparent from the low, and only recent increase in, number of publications from the area (see Figure 1.1) [11, 12].

Consequently, the small number of commercialised immunosensors is not due to insufficient investment but partially due to the fact that immunosensor research is still quite a new area, with several challenges to overcome [13]. With the exception of home pregnancy tests (which are "yes/no" type sensors and so do not supply quantitative data on antigen concentrations), low cost, generic, effective immunosensors are not yet routinely available.

The primary aim of the work presented in this thesis was to develop an immunosensor fulfilling these requirements. In order to achieve this aim it was necessary to initially establish the techniques and systems required to develop an imunosensor. These included antibody immobilisation strategies, patterning

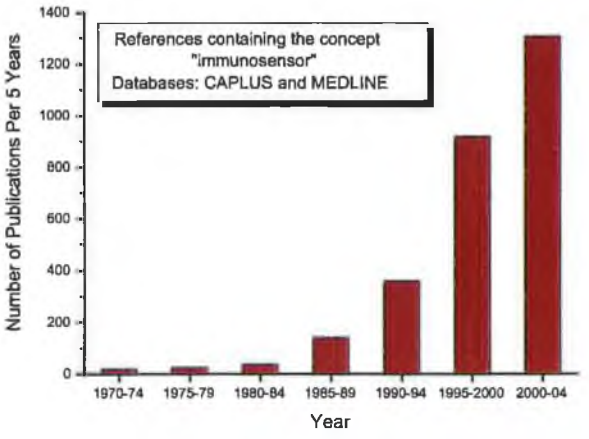


**Figure 1.1:** Histogram illustrating the number of publications containing the concept "immunosensor". Results obtained using CAPLUS and MEDLINE databases.

methods and excitation and detection systems. Parallel work, involving the analysis of fluorescence emission, led to the design and fabrication of an optimised sensor platform. The subsequent incorporation of this platform into the immunosensor system resulted in the realisation of a low-cost, generic immunosensor with improved sensitivity.

## 1.2 Current State of The Art

As the quantity of research focused on immunosensors is rapidly increasing, it is not possible to include references to all techniques currently being developed. Therefore, this section serves, not as a comprehensive review of the area, but to illustrate the variety of immunosensors currently being developed, giving examples of some of the major strategies being investigated and the advantages and limitations associated with each. As stated previously, though significant research is being currently carried out, generic, low-cost, effective immunosensors are not yet routinely available.

The immunosensor technologies being developed at present include electrochemical, mass-detection and heat-detection-based systems [13]. However, due to the numerous advantages that they offer over other techniques, optical immunosensors are currently the largest group of transducers [14]. Benefits include

the non-invasive, non-destructive nature of these methods, their ability to measure hazardous materials and the rapid signal generation and read-out.

The majority of research in optical immunosensors is focused on either refractive index-based or fluorescence-based detection methods. Therefore, explanations and examples of the main optical immunosensor types are detailed below under these two category headings.

### 1.2.1 Refractive Index-based Immunosensors

Surface plasmon resonance (SPR) is one of the most widely employed refractive index-based detection methods, with one of the leading commercial immunosensors, the BIAcore$^{TM}$ system from Biacore (Upsala, Sweden) employing SPR-based detection and numerous research groups developing SPR-based systems [15–17]. A detailed explanation of SPR-based sensing is provided in Section 2.5.1. In summary, a beam of light is used to excite surface electrons ("plasmons") in a metal film that is coated onto a high refractive index material. This generates an evanescent field, which propagates into a sample layer above the metal film. The field is highly sensitive to changes in refractive index, which occur when binding occurs in the sample layer. The attractiveness of this technology stems from the fact that labels are not required and the technology is extremely sensitive, as demonstrated by Homola et al., who achieved a refractive index resolution of $4x10^{-6}$ RIU and applied this SPR-based immunosensor to the detection of staphylococcal enterotoxin B, achieving nanogram per milliliter limits of detection [18]. SPR is also attractive for its suitability for real-time and kinetic measurements, as shown by Campagnola et al. who employed an SPR-based immunosensor to analyse the binding activity of tumour antigens and cancer patient sera containing serum antibodies [17]. Limitations of SPR-based sensors, as with the majority of refractive index-based sensors, include the fact that these sensors are sensitive to temperature and bulk refractive index changes. Also, they require high specificity of the binding layer to capture the target analyte and prevent non-specific binding to the surface, which could be recorded as a positive binding event.

Another immunosensor system being developed, which is similar in design to the SPR-based systems, is that of the resonant mirror optical immunosensor. It is this technology that is employed in the IAsys$^{TM}$ biosensor from Fisons Applied

Sensor Technology (Cambridge, UK). As with the SPR-based systems, an evanescent field is used to detect small refractive index changes that occur when a target analyte binds to a capture antibody. The sensor is comprised of a prism block with a low refractive index layer above, followed by a high refractive index layer, which acts both as a waveguide and the sensor surface. Light is coupled into the prism block and at the resonant angle, passes through the low index layer and propagates within the high index layer. This results in an evanescent field in the sample above. The light emerging from the system is passed through a polariser, which ensures that only light propagated within the waveguiding layer reaches the detector. Refractive index changes in the sample affect the evanescent field, which in turn causes movement of the resonant angle. This systems lends itself well to rapid, real-time analysis, as demonstrated by Dimitriev et al., who employed a resonant mirror optical immunosensor to carry out analysis of antibody-antigen interactions, specifically the binding of bispecific antibodies with human IgG and horseradish peroxidase [19]. Hoare et al., monitoring the production of antibody fragments, have been able to provide concentration data within 10 s of sample addition [20]. However, as with the majority of refractive index-based immunosensors, the resonant mirror immunosensors are limited by the fact that the binding of small molecules results in only small signal changes. One method employed to overcome this problem is the use of the smaller molecule as the capture agent and the larger one as the target analyte.

Székács et al. employed this strategy with the use of a diffraction grating-based immunosensor to successfully detect the herbicide trifluralin in the concentration range of $2x10^{-7}$ to $3x10^{-5}$ng/ml [21]. Diffraction grating-based immunosensors rely on the principle that if light is incident on the periodically structured surface of a diffraction grating, a series of waves directed away from the surface at different angles is produced. Typically, this type of immunosensor has been more complex to fabricate and optimise than other sensor types. However, developments in polymer processing by Whitesides et al. and others has resulted in the fabrication of polymer diffraction gratings, which renders these issues less important [22,23].

Interferometric immunosensors are another class of sensors that have developed rapidly due to advances made in other technologies. These sensors compare differences between two light beams; a sensing beam and a reference beam. When combined, they produce an interference pattern of light and dark fringes. A chem-

ical or physical reaction occurring along one of the beams causes a change in the refractive index, which is detected by the evanescent field and results in a shift of the interference pattern. Planar waveguides are a common format for these sensors, due to their long interaction length. Fabrication and optimisation of these waveguides has been assisted by advances in the telecommunications and semiconductor industries, while fluidic design has been significantly improved due to MEMS research [24]. Brynda et al. demonstrated the real-time analysis capabilites of these sensors in their measurement of analytes in blood plasmas [25]. A major limitation of interferometric immunosensors is that they require exacting design in order to control the beam paths and limit errant signals.

### 1.2.2 Fluorescence-based Immunosensors

Extensive research is currently being carried out in the area of electrochemiluminescence (ECL)-based immunosensors. These immunosensors rely on the principle that particular species/molecules/chemicals at an electrode undergo electron transfer to form excited states that emit light. In the majority of ECL-based immunosensors, the target analyte is not itself ECL-active but ECL-active species are employed as labels. For example, Paek et al. detected Legionella with a limit of detection of 2 ng/ml using ruthenium as an ECL-active label [26]. One of the reasons for the popularity of ECL-based immunosensors is the attractiveness of the labels, which are sensitive, inexpensive, nonhazardous and linear over a wide range (six orders of magnitude) [24]. They do, however, also have drawbacks, such as the necessity of carrying out stringent cleaning of the electrode both prior to and after operation.

The largest and most promising class of fluorescence-based immunosensors is that employing fluorescent labels, known as fluorophores. This is due to the significant advantages that fluorophores display over other labels. These include ease of handling, high stability, spatial resolution, multianalyte detection, reusability (due to the long shelf-life of fluorophores), sensitivity, rapid detection, simple excitation and detection instrumentation and low total system cost [27].

Fluorescence-based immunosensors typically measure changes in fluorescence lifetime, polarisation or intensity. The lifetime is a property of the fluorophore, which corresponds to the average time a fluorophore spends in an excited state,

between the absorption of a photon and its emission as fluorescence. Yuan et al. have combined the emerging technology of nanoparticles with fluorescence lifetime measurements to detect the presence of $\alpha$-fetoprotein in human serum samples, achieving limits of detection of less than 1ng/ml. Lifetime measurements are attractive due to their insensitivity to bleaching and excitation variations and also their facile calibration [24]. However, is it often seen as a technique requiring relatively expensive and complex instrumentation. Current developments in excitation and detection systems, such as the use of low-cost LED as described by Wilson et al., show that these issues are declining in importance [28].

In contrast to most lifetime-based immunosensors, flow immunosensors based on fluorescence intensity measurements have been successfully developed at low cost and demonstrated as effective portable sensors [29]. These sensors are based on displacement assays, whereby labelled antigens are displaced from immobilised antibodies by target antigens. Intensity measurements of the fluorescently-labelled displaced antigens are correlated to the concentration of target antigen present in the sample. The assay takes place under a constant flow, which allows subsequent samples to be analysed without resetting the system.

The portability, simplicity and direct and rapid detection provided by flow immunosensors has led to their use in on-site, real-time analysis, as described by Wilkins et al. in their detection of Hantavirus in human and mice blood [30]. Unfortunately, an intrinsic limitation exists in this technology, namely, the degradation of signal due to the fact that the number of labelled antigens present in the immunosensor are reduced with each measurement, resulting in a reduction of assay response over time [31]. For this reason, it is imperative that calibration steps be included for each immunoassay.

Displacement assays have also been carried out using waveguide-based immunosensors. These immunosensors, however, are not restricted to this assay format and can also be used with other formats such as sandwich and competitive assays (see Section 2.5.3 for explanations of these assay types). Waveguide immunosensors are based on the principle that light propagating within a waveguide generates an evanescent field, which is used to excite fluorescently-labelled antigens or antibodies immobilised on the surface of the waveguide. Using the evanescent field introduces surface specificity to the immunosensor and thus, ensures that the system is less affected by turbidity, particulates or fluorophores

within the bulk solution. These immunosensors often display rapid detection times, with Rowe-Taitt et al., for example, monitoring six biohazardous analytes in 20 mins [32]. The most common example of waveguide-based sensors are optical fibre-based sensors. Many examples exist in the literature of optical fibres employed as platforms for immunosensing, employing either evanescent field excitation or developed as probe-types systems [33–35]. However, optical fibres suffer from several disadvantages, such as lack of robustness and stringent coupling requirements, which make them problematic to employ outside of the lab as portable sensors. For these reasons, planar-based platforms formed the focus of this work. The geometry of the planar waveguide-based immunosensor is inherently more robust than that of an optical fibre. Ligler et al. have also demonstrated the multianalyte capabilities of these planar immunosensors by patterning multiple capture antibodies along the length of the waveguides and simultaneously detecting multiple target antigens [36].

Due to the advantages displayed by planar waveguide immunosensors, the initial immunosensor presented in this thesis was based on this planar waveguide technique. Subsequently, an immunosensor based on a novel polymer sensor platform was designed, which demonstrated increased performance over the planar version.

## 1.3 Thesis Structure

Chapter 1 provides the introduction to this work, explaining the concept of immunosensors and providing an overview of the the current state of the art in this area. An outline of the thesis is presented and the objectives of the work are stated.

Chapters 2 and 3 provide background knowledge required to understand the working of the immunosensor presented here. The two fundamental elements of the sensor, namely the sensing mechanism and transduction are detailed in Chapter 2 and Chapter 3 respectively. In Chapter 2, antibodies are introduced and antigen detection explained in detail. Their role in immunoassays is presented and the various immunoassay formats employable are described. In Chapter 3 the concept of fluorescence is explained and the different fluorescence excitation techniques are presented. In particular, waveguiding and evanescent wave excitation

are described in detail.

Chapter 4 details the development of a planar immunosensor, employing the theory described in Chapters 2 and 3. Each of the elements required for the formation of the immunosensor are described, including antibody immobilisation, patterning techniques and excitation and detection systems. Integrating each of these techniques and systems culminates in the attainment of a full dose response curve for BSA/antiBSA.

Chapter 5 details the experimental verification of two separate predictions of a new theory, developed by a colleague, describing the angular emission of fluorescent dipoles at a surface. The first prediction states that, due to the emission of the fluorescence in distinct angular ranges, redirection of the fluorescence should result in increased signal detection. The design and fabrication of a structured platform to test this prediction is presented and experimental verification of the prediction is provided. Experimental verification is also provided for the second prediction, which states that it is possible to discriminate between fluorescence originating from the surface and fluorescence originating from the bulk solution. In the final section of the chapter, the structured platform is investigated to determine if the ability to discriminate between surface and bulk fluorescence is inherent in the design.

Chapter 6 details the optimisation of the planar immunosensor presented in Chapter 4. The main feature of the enhanced immunosensor is the substitution of the planar glass substrate with the structured polymer platform developed as a result of the work presented in Chapter 5. Replacement of the glass substrate with a polymer platform necessitated the use of a new antibody immobilisation strategy. The investigation of several antibody to polymer immobilisation strategies is presented and a suitable strategy selected. The incorporation of the structured polymer substrate required the adaptation of each of the other techniques and systems developed in Chapter 4. These modifications to the patterning, excitation, detection and analysis systems are described and finally, results are presented from an immunoassay successfully carried out using the enhanced immunosensor.

Chapter 7 draws the conclusions of the work, namely that techniques for developing an effective immunosensor have been established and enhancement strategies were thoroughly investigated and implemented. The end result of the work is the successful design, fabrication and implementation of a generic, opti-

mised immunosensor.

## 1.4 Thesis Objectives

- To establish the techniques required to develop an effective optical immunosensor, in particular, antibody immobilisation strategies, patterning methods and excitation, detection and analysis systems.
- To verify theoretical predictions relating to fluorescence emission and use the results obtained in the design and fabrication of an enhanced platform for fluorescence detection.
- To develop a generic, optical immunosensor, with enhanced fluorescence detection capabilities.

# Bibliography

[1] Microsoft, *Encyclopedia Encarta*. 2002.

[2] L. Pasteur, "Germ theory and its applications to medicine and surgery," *Comptes rendus de l'Academie des Sciences*, vol. lxxxvi., pp. 1037–43, 1878.

[3] E. Britannica Inc., "Encyclopedia Britannica," 2005.

[4] "Antibodies," *The Antibody Resource Page*, http://www.antibodyresource.com/antibody.html, 2005.

[5] "The Linus Pauling Papers," *Profiles in Science*, National Library of Medicine, 2004.

[6] I. McKay, "Antibodies," *Microbiology and Pathology Course, Univeristy of Glasgow*, 2002.

[7] C. Fiola, "Monoclonal antibodies as anticancer agents," *US Pharmacist*, vol. 28, no. 10, Oncology Supplement, 2003.

[8] C. Price, "The evolution of immunoassay as seen through the journal Clinical Chemistry," *Clin Chem*, vol. 44, no. 10, pp. 2071–2074, 1998.

[9] J. Gosling, "A decade of development in immunoassay methodology," *Clin Chem*, vol. 36, no. 8, pp. 1408–1427, 1990.

[10] C. Nylander, B. Liedberg, and T. Lind, "Gas detection by means of surface plasmon resonance," *Sensors and Actuators*, vol. 3, pp. 79–88, 1982.

[11] A. Chemical Society, "CAplus - chemical abstracts plus database," 2005.

[12] "NLM databases and electronic resources," *National Library of Medicine*, http://www.nlm.nih.gov/databases/, 2005.

[13] C. Morgan, D. Newman, and C. Price, "Immunosensors: technology and opportunities in laboratory medicine," *Clin Chem*, vol. 42, no. 2, pp. 193–209, 1996.

[14] P. Luppa, L. Sokoll, and D. Chan, "Immunosensors-principles and applications to clinical chemistry," *Clinica Chimica Acta*, vol. 314, pp. 1–26, 2001.

[15] L. M. May and D. Russell, "Novel determination of cadmium ions using an enzyme self-assembled monolayer with surface plasmon resonance," *Analytica Chimica Acta*, vol. 500, no. 1-2, pp. 119–125, 2003.

[16] T. Ozawa, M. Kakuta, M. Sugawara, Y. Umezawa, and M. Ikura, "An optical method for evaluating ion selectivity for calcium signaling pathways in the cell," *Analytical Chemistry*, vol. 69, no. 15, pp. 3081–3085, 1997.

[17] C. Campagnolo, K. Meyers, T. Ryan, R. Atkinson, Y.-T. Chen, M. Scanlan, G. Ritter, L. Old, and C. Batt, "Real-time, label-free monitoring of tumor antigen and serum antibody interactions," *Journal of Biochemical and Biophysical Methods*, vol. 61, no. 3, pp. 283–298, 2004.

[18] M. Piliarik, J. Homola, Z. Manikova, and J. Ctyroky, "Surface plasmon resonance sensor based on a single-mode polarization-maintaining optical fiber," *Sensors and Actuators B: Chemical*, vol. 90, no. 1-3, pp. 236–242, 2003.

[19] D. Dmitriev, Y. Massino, O. Segal, M. Smirnova, E. Pavlova, K. Gurevich, O. Gnedenko, Y. Ivanov, G. Kolyaskina, and A. Archakov, "Analysis of the binding of bispecific monoclonal antibodies with immobilized antigens (human IgG and horseradish peroxidase) using a resonant mirror biosensor," *Journal of Immunological Methods*, vol. 261, no. 1-2, pp. 103–118, 2002.

[20] A. Gill, D. Bracewell, C. Maule, P. Lowe, and M. Hoare, "Bioprocess monitoring: An optical biosensor for rapid bioproduct analysis," *Journal of Biotechnology*, vol. 65, no. 1, pp. 69–80, 1998.

[21] A. Szekacs, N. Trummer, N. Adanyi, M. Varadi, and I. Szendro, "Development of a non-labeled immunosensor for the herbicide trifluralin via optical waveguide lightmode spectroscopic detection," *Analytica Chimica Acta*, vol. 487, no. 1, pp. 31–42, 2003.

[22] O. Schueller, D. Duffy, J. Rogers, S. Brittain, and G. Whitesides, "Reconfigurable diffraction gratings based on elastomeric microfluidic devices," *Sensors and Actuators A: Physical*, vol. 78, no. 2-3, pp. 149–159, 1999.

[23] A. Massari, K. Stevenson, and J. Hupp, "Development and application of patterned conducting polymer thin films as chemoresponsive and electrochemically responsive optical diffraction gratings," *Journal of Electroanalytical Chemistry*, vol. 500, no. 1-2, pp. 185–191, 2001.

[24] F. Ligler and C. R. Taitt, *Optical Biosensors: Present and Future.* Amsterdam: Elsevier, 2002.

[25] E. Brynda, M. Houska, A. Brandenburg, and A. Wikerstal, "Optical biosensors for real-time measurement of analytes in blood plasma," *Biosensors and Bioelectronics*, vol. 17, no. 8, pp. 665–675, 2002.

[26] C.-H. Yoon, J.-H. Cho, H.-I. Oh, M.-J. Kim, C.-W. Lee, J.-W. Choi, and S.-H. Paek, "Development of a membrane strip immunosensor utilizing ruthenium as an electro-chemiluminescent signal generator," *Biosensors and Bioelectronics*, vol. 19, no. 4, pp. 289–296, 2003.

[27] B. Read, "Why fluorescence detection is getting glowing reviews," *Internation Biotechnology Laboratory*, February, 2001.

[28] A. Moe, S. Marx, N. Banani, M. Liu, B. Marquardt, and D. Wilson, "Improvements in LED-based fluorescence analysis systems," *Sensors and Actuators B: Chemical*, In Press, 2005.

[29] C. Barzen, A. Brecht, and G. Gauglitz, "Optical multiple-analyte immunosensor for water pollution control," *Biosensors and Bioelectronics*, vol. 17, no. 4, pp. 289–295, 2002.

[30] S. Yelleti and E. Wilkins, "Design of an automated immunosensor device for fast detection of hantavirus in mice blood," *Sensors and Actuators B: Chemical*, vol. 97, no. 2-3, pp. 298–306, 2004.

[31] S. Rabbany, A. Kusterbeck, R. Bredehorst, and F. Ligler, "Binding-kinetics of immobilized antibodies in a flow immunosensor," *Sensors and Actuators B-Chemical*, vol. 29, no. 1-3, pp. 72–78, 1995.

[32] C. Rowe-Taitt, J. Cras, C. Patterson, J. Golden, and F. Ligler, "A ganglioside-based assay for cholera toxin using an array biosensor," *Analytical Biochemistry*, vol. 281, no. 1, pp. 123–133, 2000.

[33] C. Zhou, P. Pivarnik, S. Auger, A. Rand, and S. Letcher, "A compact fiber-optic immunosensor for salmonella based on evanescent wave excitation," *Sensors and Actuators B: Chemical*, vol. 42, no. 3, pp. 169–175, 1997.

[34] C. Preininger, A. Mencaglia, and F. Baldini, "Polymer-coated optical fibres for application in a direct evanescent wave immunoassay," *Analytica Chimica Acta*, vol. 403, no. 1-2, pp. 67–76, 2000.

[35] M. Daneshvar, J. Peralta, G. Casay, N. Narayanan, L. E. Iii, G. Patonay, and L. Strekowski, "Detection of biomolecules in the near-infrared spectral region via a fiber-optic immunosensor," *Journal of Immunological Methods*, vol. 226, no. 1-2, pp. 119–128, 1999.

[36] J. Golden, C. Taitt, L. Shriver-Lake, Y. Shubin, and F. Ligler, "A portable automated multianalyte biosensor," *Talanta*, vol. 65, no. 5, pp. 1078–1085, 2005.

# Chapter 2

# Biorecognition

## 2.1 Introduction

As explained in Section 1.1, immunosensors employ antibodies as their sensing agents. This chapter will provide a thorough description of antibodies in terms of their function and structure and give reasons for their choice. The antibody binding mechanism will be detailed, with reference to binding site composition and the forces involved. Finally, the various immunoassay categories and formats commonly employed in immunosensing will be explained.

## 2.2 Proteins

Antibodies are a subgroup of proteins, which, due to their high availability and specificity, are one of the major types of biomolecules employed in biosensors. Other commonly used biomolecules include nucleic acids such as deoxyribonucleic acid (DNA) or ribonucleic acid (RNA) [1–4]. The basic building blocks of proteins are amino acids, which are molecules containing amine ($NH_2$) and carboxyl (COOH) functional groups [5]. Their chemical structure is shown in Figure 2.1, where R represents a side chain. These side chains distinguish one amino acid from another and determine properties such as size, charge and hydrophobicity.

Amino acids link together to form long chains known as polypeptides. The name arises from the fact that each of the amino acids is joined via peptide bonds, which are the bonds formed between amine and carboxyl groups, as shown in

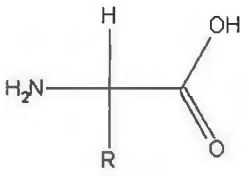


**Figure 2.1:** Chemical structure of an amino acid. R represents a side chain, which defines the amino acid.

Figure 2.2. Every polypeptide begins with a free amine group and is called the N-terminus. The opposite end of the polypeptide has a free carboxyl group and is referred to as the C-terminus.

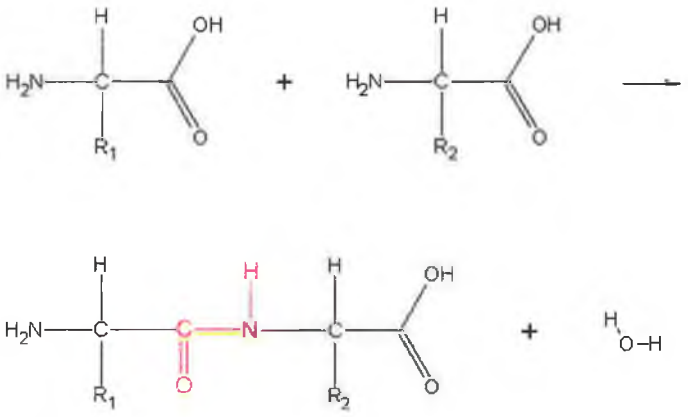


**Figure 2.2:** Formation of an amino acid chain. Binding occurs via peptide bonds, which are highlighted in red.

Proteins are complex organic compounds, which are composed of one or more polypeptide chains [6]. The position and arrangement of the amino acids determines both the function and the three-dimensional folded structure of the protein.

Enzymes, cell receptors and antibodies are three of the most widely used protein-based molecules in biosensors [7–15]. Enzymes are large molecules produced by living cells in order to catalyse biochemical reactions. The enzymes themselves are not changed by the reactions that they catalyse. Enzymes are often chosen as sensing agents due to their high specificity with regards to the type of chemical reaction they catalyse and the substance upon which they act [16]. An example of a widely used enzyme is that of glucose oxidase, which is commonly employed in glucose sensing [17–19].

Cell receptors are protein-based structures found in the plasma membrane of cells, which bind specifically with a range of organic molecules, including proteins and viruses [6]. There are several modes of operation for cell receptors. One of the most common occurs when the receptor spans the cell membrane. The binding to the receptor induces a conformational change that activates the internal portion of the cell receptor to initiate a chain reaction of chemical changes within the cell [6].

The third main type of protein used as biosensor sensing agents are antibodies, which were the sensing agents chosen for use in the biosensor presented here. There were two main reasons for this. Firstly, there is considerable experience in the area of antibody engineering here at the National Centre for Sensor Research, at Dublin City University [20–24] and secondly, the fact that antibodies can be generated against a large variety of antigens. This is important as the biosensor presented here is intended to be a generic sensor, capable of detecting a wide variety of analytes.

## 2.3 Antibodies

### 2.3.1 Antibody Function

Antibodies are an integral part of a body's immune system. When a foreign molecule, such as a pathogen or toxin, enters the body it stimulates a class of white cells known as B-lymphocyte cells (B cells) to mature into antibody producing plasma cells. The plasma cells are triggered by the foreign molecule, known as an antigen, into producing antibodies that possess antigen binding sites [25].

Once generated, the antibody binds to its specific antigen to form a single complex. In this way, the antibody marks the antigen for destruction by phagocytes, which are cells that ingest and destroy marked foreign molecules [25]. Though more commonly used to mark molecules for destruction, in some cases the antibodies themselves can destroy pathogens by inducing the formation of hydrogen peroxide from oxygen free radicals and water [26].

All of the antibodies that a given B cell secretes have the same specificity for the antigen and are called monoclonal antibodies. However, when the immune

system is challenged with an antigen, many different B cells respond and secrete antibodies. Each of these antibodies recognises the antigen but in slightly different ways. These antibodies are known as polyclonal antibodies and comprise different specificities and cross-reactivities [26]. Polyclonal antibodies are suitable for certain assays such as when a family of toxins is being detected, but increasingly, monoclonal antibodies are desirable. This has resulted in extensive research of new methods of producing monoclonal antibodies [27]. One well documented method is that of cell fusion, whereby a tumor cell derived from a lymphocyte cell is fused with a B cell to form hybridomas [28]. These hybrid cells are immortal and proceed to produce monoclonal antibodies indefinitely.

### 2.3.2 Antibody Structure

Regardless of whether the antibodies are monoclonal or polyclonal, they possess the same basic immunoglobulin structure. The structure is comprised of two identical heavy polypeptide chains and two identical light polypeptide chains. Both the heavy and light chains contain the amino acid cysteine, which is an amino acid whose side chain terminates in a sulfhydryl (SH) group. Sulfhydryl groups link to each other to form disulphide bonds. In this way, a cysteine in the heavy chain links with a cysteine in the light chain to join both chains via a disulphide bridge [26]. The resultant antibody structure is illustrated in Figure 2.3, with the amine and carboxyl functional groups present at the N-terminus and C-terminus respectively indicated (see Section 2.2 for more information).

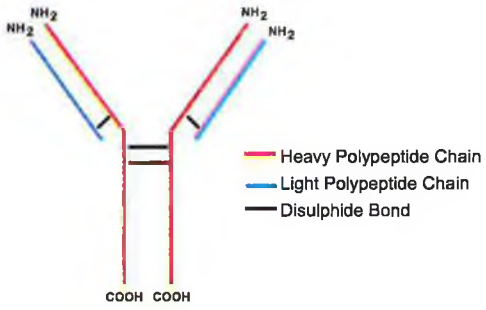


**Figure 2.3:** Illustration of antibody structure, indicating the terminal functional groups.

The polypeptide chains fold to form structures called protein domains. Each

light chain is composed of two domains, while each heavy chain is composed of four. These domains associate to form three distinct globular portions, resulting in a Y-shaped structure (see Figure 2.4).


**Figure 2.4:** Illustration of antibody Y-shaped structure formed by protein domains (Image copyrighted by Mike Clarke, Cambridge University [29]).

The stem of the Y shape is composed of two heavy chains and is called the Fc region. The two domains (labelled $C_H2$ and $C_H3$ in Figure 2.5) in this portion of the antibody, along with the lower domains of the two arms ($C_H1$ and $C_L$), form the constant region of the antibody common to all antibodies [30]. Each of the arms of the Y-shaped structure is comprised of a heavy and a light chain. This portion of the antibody is referred to as the Fab portion [31]. As mentioned above, the lower domains of the arms are constant regions ($C_H1$ and $C_L$), while the upper domains are variable regions ($V_H$ and $V_L$). It is a particular section of the variable regions that forms the antigen binding site [30]. Figure 2.5 shows a schematic of antibody chains and regions.

### 2.3.3 Antibody Classes

Immunoglobulins are classified by the structure of their heavy chains. There are five distinct antibody classes found in large mammals; immunoglobulin G (IgG), immunoglobulin A (IgA), immunoglobulin M (IgM), immunoglobulin D (IgD) and immunoglobulin E (IgE) [28]. The heavy chain of each immunoglobulin is referred to by its corresponding lower-case Greek letter, i.e. $\gamma$, $\alpha$, $\mu$, $\delta$ and $\epsilon$. The following descriptions of each of the antibody classes, characteristics and

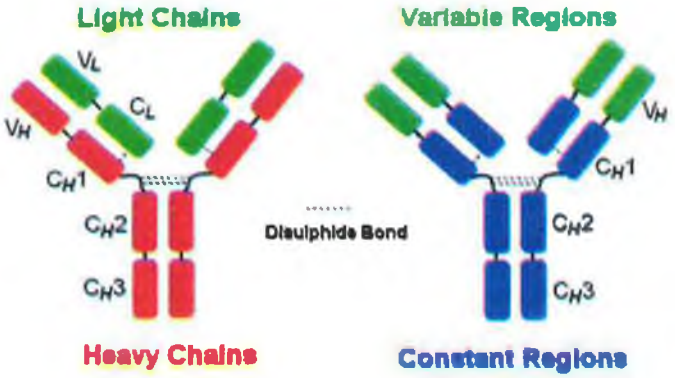


**Figure 2.5:** Schematic of antibody structure, indicating the locations of chains and regions.

physical properties are taken from *Immunology, 6th Edition* by Roitt, Brostoff and Male [25].

IgG antibodies are the largest class of antibody found in human serum, accounting for over 70 % of the total immunoglobulin pool. They are based on the basic four chain molecule structure and are composed of approximately 2–3 % carbohydrate. A schematic of the IgG antibody structure is shown in Figure 2.6 (Figures 2.6 to 2.11 reproduced with kind permission from Duane W. Sears [32]). It is this particular class of antibodies that was used in the work presented here. Details of the specific antibodies employed are given in Section 4.2.2.

**Figure 2.6:** Schematic of immunoglobulin IgG structure

There are four known subclasses of IgG; namely, IgG1, IgG2, IgG3 and

IgG4 [28]. Though still recognisable as $\gamma$ chains, the heavy chain structure of each of these subclasses varies slightly from each other. These variations develop in order for the antibody subclass to carry out slightly different functions. For example, the IgG subclasses found in humans and mice have developed in order to carry out functions specific to their hosts' needs and so are different from each other [30]. The main difference between the IgG subclasses occurs in the pattern of disulphide bonds linking the two heavy chains. Figure 2.7 shows a schematic of the IgG immunoglobulin subclasses.

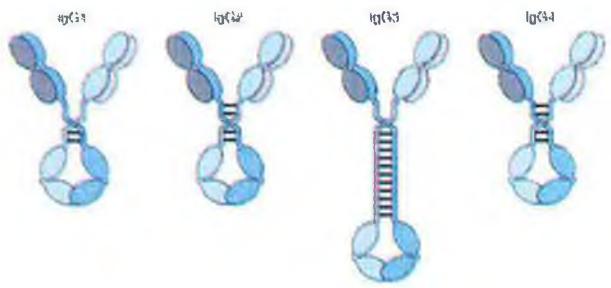

**Figure 2.7:** Schematic of immunoglobulin IgG subclasses.

After IgG immunoglobulin, IgA is the next largest class of antibody found in human serum, accounting for approximately 15–20 % of the total immunoglobulin pool. The majority of human IgA antibodies are comprised of the basic four chain molecule shown in Figure 2.6. However, in most mammals IgA is usually found as a dimer, i.e. formed from two of the basic four chain molecules (see Figure 2.8). The two molecules are bound via a peptide chain called a J chain. IgA antibodies are the predominant antibody class found in secretions such as saliva and milk, with secreted IgA being of the subclass IgA1 or IgA2.

IgM is the next largest class of immunoglobulin, accounting for approximately 10 % of all antibodies found in human serum. It comes in the form of a pentamer of the basic four chain molecule, with 12–14 % of its content comprised of carbohydrate. Like IgA antibodies, it also features a J chain. A schematic of the pentamer structure is shown in Figure 2.9.

IgD immunoglobulins are a major component of the surface membranes of many B cells but comprise less than 1 % of the total immunoglobulins found in human serum. Like IgM immunoglobulins, carbohydrate forms 12–14 % of their

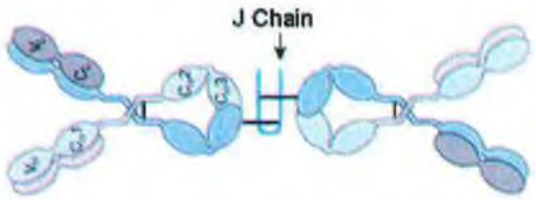


**Figure 2.8:** Schematic of immunoglobulin IgA structure

**Figure 2.9:** Schematic of immunoglobulin IgM structure

content, though the carbohydrates are found in locations different to those on the IgM antibodies (see Figure 2.10).

**Figure 2.10:** Schematic of immunoglobulin IgD structure

IgE immunoglobulins are the least common antibody type, with only trace amounts present in human serum. They are found on the surface membrane of mast cells, which are cells involved in the production and release of chemical mediators that result in asthma and other conditions [25]. IgE immunoglobulins are probably most well known for the part they play in food allergies. It is this class of immunoglobulin that initiates the immune response to antigens present on protein molecules found in particular foods that cause allergic reactions in certain individuals [26]. IgE antibodies have an additional constant region, $C_H4$, as illustrated in the schematic shown in Figure 2.11.

**Figure 2.11:** Schematic of immunoglobulin IgE structure

## 2.4 Antigen-Antibody Interaction

### 2.4.1 Antigen Binding

Each antibody domain is comprised of strands of polpeptide chains. An illustration of this is shown in Figure 2.12.


**Figure 2.12:** Illustration of antibody structure formed by strands of polypetide chains (Image copyrighted by Mike Clarke, Cambridge University [29]).

Antigen binding sites occur at the end of the variable domains, with the variable domain of each antibody differing from that of all other antibodies. The difference arises as a result of variations in the amino acid sequence of the polypeptide chains (predominantly in the binding regions). These variations occur along the length of the chains but three specific areas show particularly high degrees of variability. These areas are called the hypervariable regions [31].

The three hypervariable regions occur at the loops of the polypeptide chains, where the strands change direction. The three regions together are called the complementarity-determining regions (CDRs) (see Figure 2.13). Both the variable heavy and light chains contain CDRs, which when combined, form the antigen binding site [30].

Since the CDRs of each antibody vary from one other, the shape of each antigen binding site also varies. Antigens can only bind to specific antibodies when their surfaces are complementary to the the shape of the antigen binding site. This is known as steric compatibility [31]. The portion of the antigen that binds to the antibody is called the epitope. There are three distinct ways in which it can bind; in pockets, in grooves or along the surface of the antigen binding site [31]. In the first case, the entire epitope fits into the binding site. In the second case, the epitope slots into the groove between the heavy and light chains

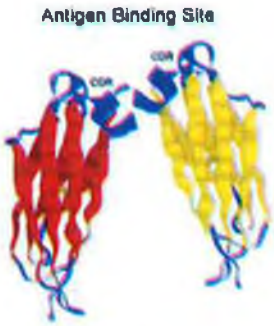


**Figure 2.13:** Representation of antibody variable region, indicating the location of the complementarity-determining regions (CDRs). The CDRs (shown as blue loops) of both the heavy and light chains combine to form the antigen binding site.

and in the third case the epitope is larger than the binding site but a section of its surface conforms to the antigen binding site. The three cases are illustrated in Figure 2.14.


(a) (b) (c)

**Figure 2.14:** Types of conformational binding sites available on antibodies. Antigens are shown in orange, with their epitopes highlighted in red. Image (a) illustrates a pocket binding site. Image (b) illustrates a groove binding site. Image (c) illustrates a surface binding site (Images copyrighted by Garland Publishing/Elsevier Science 2000 [31]).

An element of steric compatibility involves the electron clouds of the antigen and antibody. Though the antigen may be structured to fit into the binding site, if the antigen's electron cloud overlaps with areas of the antibody's electron cloud then repulsive forces will come into effect [25]. Antigen association involves overcoming these repulsive forces and establishing attractive interactions between the antibody and the antigen. The attractive forces involved in the antigen

binding need to be greater than the repulsive forces in order for binding to occur.

The four non-covalent attractive forces involved in antigen binding are electrostatic forces, hydrogen bonding, van der Waal forces and hydrophobic forces [30]. Individually, each of the forces is weak in comparison to covalent bonds. However, the large number of interactions involved in the antigen binding results in a large total binding energy.

For each of the forces involved, the strength of the bond created is different, but in all cases it is inversely proportional to the distance between the antigen and antibody. The strength of each of the electrostatic forces, for example, is proportional to $1/d^2$ [25]. These are the forces that occur between opposite charges. Both antigens and antibodies usually contain many charged amino acid side chains, which are affected by these forces [31].

Hydrogen bonding occurs when a hydrogen atom is shared between two electronegative atoms [31]. The first atom is the proton donor, consisting of a hydrogen atom bound to an electronegative atom. A proton acceptor, consisting of an electronegative atom with a lone pair of electrons, attracts the hydrogen atom to form a hydrogen bond. These bonds stabilise the antibody.

Van der Waal forces are generated by the electron clouds of adjacent molecules. Fluctuations in these clouds cause polarisation of nearby atoms. The strength of these reactions is proportional to $1/d^6$ [25].

Hydrophobic forces are the final non-covalent forces involved in antigen binding. These forces occur between non-polar molecules and water, with the non-polar molecules being brought together to exclude water. One of the reasons for this occurrence is that in the absence of water, the non-polar molecules can assume lower, more favourable energy configurations [33].

### 2.4.2 Affinity

The sum of all the attractive and repulsive forces acting at an antibody binding site is known as the affinity [25]. It is a measure of the strength of the reaction between a single antibody binding site and a single antigen. Figure 2.15 illustrates the basic concept.

The term avidity is given to the total strength of the antigen binding [25]. Antibodies are multivalent, having more than one binding site. For this reason,

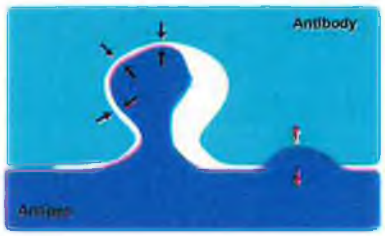


**Figure 2.15:** Illustration of attractive (black arrows) and repulsive (red arrows) forces operating at an antigen binding site.

the avidity of an antibody is often more useful than the affinity. It should be noted that the avidity of an antibody for an antigen is greater than merely the sum of the individual affinities of each of the binding sites [25]. This is because all of the bonds must be broken simultaneously in order for dissociation to occur.

There are several factors that affect affinity and hence the possibility of dissociation occurring. Changes in pH, temperature and ionic strength all affect affinity and so need to be controlled in order to optimise the binding conditions [31].

## 2.5 Immunoassays

### 2.5.1 Label-Free Immunoassays

The basis of an immunoassay is the detection of antigens through the use of antibodies. Antigens can also be used to detect the presence and concentration of antibodies. For simplicity of description, each of the following assays shall be described in term of antigen detection.

The majority of immunoassays can be categorised as either labelled or label-free immunoassays. Two of the main label-free assays are agglutination assays and precipitation assays. In agglutination assays a suspension of antibody-coated latex beads forms an opaque solution. The addition of antigen results in the binding together of several antibody-coated beads to form minute clumps. Consequently, as the beads are no longer dispersed throughout, the solution changes from opaque to clear [28]. The process is illustrated in Figure 2.16.

Precipitation assays are based on a very similar process to agglutination assays. When antibodies are mixed with their specific antigen, precipitation occurs

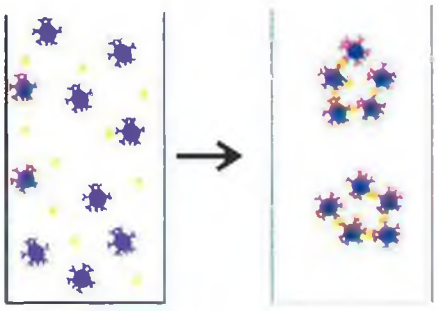

(a) (b)

**Figure 2.16:** Illustration of the basic concept of agglutination assays. In image (a) latex beads coated with antibodies are suspended in solution. In image (b) the beads are clumped together due to the addition of antigens into the solution, which form links between the antibody coated beads.

and is either visible for detection or measured by its ability to scatter light [30].

Both agglutination and precipitation immunoassays tend to be less sensitive than labelled immunoassays i.e. their lower limits of detection are higher than those of the labelled assays [30]. One type of label-free immunoassay that is capable of low limits of detection is the surface plasmon resonance (SPR)-based immunoassay [34]. SPR can be explained as the collective excitation of electrons at the interface of a metallic surface and a dielectric [35]. SPR is highly sensitive to changes in the refractive index at the boundary. It is this fact that is exploited in the majority of SPR-based immunoassays [36–38]. A typical configuration is comprised of a glass chip coated with a metallic film, upon which antibodies are immobilised. A prism is positioned on the opposite side of the glass chip, with a light source located normal to it to ensure that the emitted photons are not refracted when they enter the prism. Photons emitted from the light source pass through the prism and generate SPR in the metallic layer. When resonance occurs, the reflected light intensity from the metallic layer goes through a minimum at a defined angle of incidence. The angle of minimum reflected light intensity is recorded using an optical detector such as a photodiode array or CCD camera (see Section 3.5 for information on detectors). Antigens specific to the antibodies are passed over the surface and bind to the antibodies. In doing so, they increase the concentration, and hence the refractive index, at the surface. This results in

a measurable angular shift in minimum reflected light intensity, which can be used to determine the concentration of antigens bound to the immobilised antibodies. A schematic of the setup is shown in Figure 2.17.

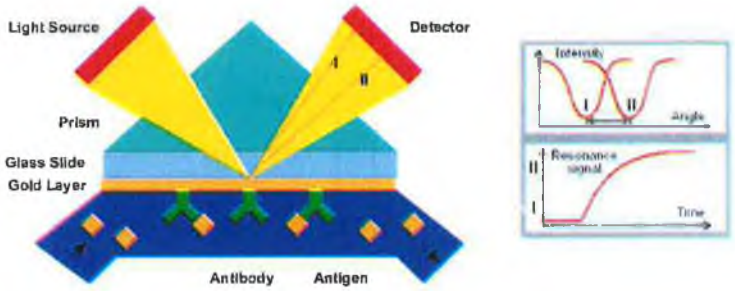


**Figure 2.17:** Surface plasmon resonance set-up.

A major advantage of SPR-based immunoassays is that they carry out real-time measurements, which is not possible with some of the other types of immunoassays. There are many commercially available SPR-based immunosensors but the most widely used are those developed by BiaCore$^{TM}$ [34] (Upsala, Sweden). These are examples of heterogeneous assays, which are assays that can discriminate between bound and unbound antigens and therefore do not require the unbound antigens to be removed before detection of the bound antigens takes place. Homogeneous assays, in contrast, require unbound antigens to be removed before detection of bound antigens can take place.

### 2.5.2 Label-Based Immunoassays

There are four main types of label-based immunoassays; radiolabelled, enzyme-labelled, chemiluminescent-labelled and fluorescently-labelled immunoassays.

#### Radiolabelled Immunoassays

In radiolabelled immunoassays, antibodies are labelled with radioisotopes. These were one of the first types of labels to be used in immunoassays [28]. The radioisotope decays at a known rate and the emission of the subatomic particles is detected using a counter coupled to a photomultiplier tube. The emitted particles, and hence the counter required, vary depending on the isotope used, though

most emit $\beta$ particles or gamma radiation. The radioisotope Iodine-125 is commonly employed. This isotope emits gamma radiation and has a half-life (time taken for half the number of radioactive nuclei to decay) of 60 days [28]. Due to radiation dose concerns, the stringent controls required and the increase in alternative labels, radioisotopes have decreased in popularity over the past few decades.

### Enzyme-Labelled Immunoassays

One of the most widely used immunoassay types is the enzyme-labelled immunoassay [13–15, 39–41]. Enzyme characteristics, such as high specificity and strong catalytic power, make them very attractive labels. Generally, enzyme-labelled immunoassays employ two levels of antibodies; a primary antibody, which recognises the antigen and an enzyme-labelled secondary antibody, which recognises the primary antibody. A substrate, which is a chemical entity whose conversion to a product is catalyzed by an enzyme, is then introduced. The assay procedure is shown in Figure 2.18. Depending on the reaction that occurs, detection can be colorimetric, fluorometric or chemiluminescent [42].

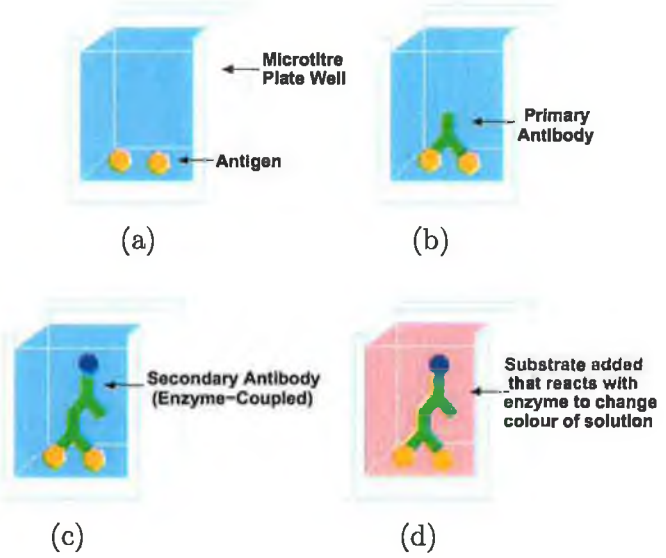


**Figure 2.18:** Illustration of enzyme-labelled immunoassay.

Two of the most commonly employed enzyme-labelled immunoassays are Western Blots and Enzyme-Linked Immunosorbent Assays (ELISAs). In West-

ern Blots, gel electrophoresis is used to separate proteins of different sizes. This is accomplished by passing the sample through a negatively-charged gel. The smaller and lighter the proteins, the faster they travel. It must be noted however that the charge of the particle can also influence its position in the column. Once the proteins have been separated, they are transblotted onto a membrane. This is then incubated with specific antibodies, which bind to the protein of interest. This is subsequently detected using an enzyme-labelled secondary antibody that reacts with the primary antibody. A substrate that gives a coloured product on reaction with the enzyme label is then added. An example of the results obtained is shown in Figure 2.19.

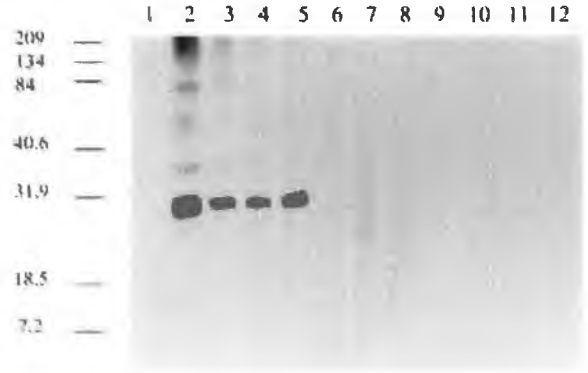


**Figure 2.19:** Results from a Western Blot assay. Charged gel is used to separate proteins by weight. Their presence is then indicated using enzyme-labelled antibodies. Column 1 is a negative control, column 2 is a set of molecular weight markers, columns 3-5 are chicken sera containing the antibody of interest and columns 6-12 are chicken sera not containing the antibody of interest. Protein weights (in kilodaltons) are indicated on the left.

ELISAs are typically carried out using microtitre plates, which are polymer plates containing 96 or 384 wells. The antigens of interest are immobilised in the wells and secondary, enzyme-labelled, antibodies are added. A substrate is then added to each well, where it reacts with the enzyme, resulting in a colour change of the solution. Each well can be coated with varying concentrations of antigen, with the same concentrations of primary and secondary antibody added to each. ELISAs are used extensively for a wide variety of tests, including HIV

screening [43]. A disadvantage of using enzyme-labelled immunoassays is that they can be inhibited by certain factors. For example, horse radish peroxidase (HRP), which is one of the most commonly employed enzymes, is inhibited by sodium azide ($NaN_3$), which is regularly used in antibody solutions to prevent bacterial growth [28]. It is also inhibited by $O_2$ and $Cl_2$ and is found in serum and other important analytical matrices [28].

### Chemiluminescent and Bioluminescent Immunoassays

Chemiluminescence is the emission of light caused by a chemical reaction [28]. Two or more compounds react to create an excited state, which on decaying to the ground state, emit photons. Bioluminescence is a form of chemiluminescence, where the compounds involved in the reaction are found in living organisms [5].

The light emitted often only lasts for a few seconds. For example, reacting acridium ester with $OH^-$ and $H_2O_2$, results in a burst of light that lasts for approximately 5 seconds [28]. Reagent addition must be fast and extremely precise because the reaction occurs so quickly. In some cases, this can be overcome by using an enhancer to extend the light emission time. For example, using the chemical enhancer p-iodophenol with the reagents peroxidase, luminol and $H_2O_2$, results in a light emission that lasts longer than 30 minutes [28].

Chemiluminescent assays are extremely sensitive to factors that influence the recorded signal, such as background, inhibitors and enhancers. The purity of the reagents used and the cleanliness of equipment must be strictly controlled.

### Fluorescently-Labelled Immunoassays

In fluorescently-labelled immunoassays, the labels used are fluorescent molecules, known as fluorophores. These molecules absorb light of a particular wavelength, which raises them to an excited state. They then revert to their ground state, emitting light of a second and higher wavelength. This process will be explained in detail in Chapter 3.2.

It was this form of assay that was employed in the immunosensor presented here. Some of the reasons for this choice include the fact that, unlike surface plasmon resonance-based immunoassays, fluorescently-labelled immunoassays do not require the use of a metallic substrate, which gives the fluorescent immunoas-

says an extra degree of versatility with regards to substrate choice. There are no safety concerns with the use of fluorophores, as opposed to concerns over radiation doses when using radioisotopes as labels. Unlike enzyme and chemiluminescent labelled immunoassays, fluorescently-labelled immunoassays do not require a second reagent for the reaction to occur. Fluorophores are also easily attached to proteins, are very stable and are readily available in a wide range of wavelengths, which increases the multianalyte capabilities of the immunosensor. Finally, fluorescence is intrinsically a highly sensitive process, which implies that fluorescently-labelled immunoassays are capable of achieving very low detection limits.

### 2.5.3 Assay Formats

There are four main immunoassays formats: direct binding, competitive, displacement and sandwich assay. Direct binding assays are the simplest to perform. Antibodies specific to the antigen of interest are immobilised on the sensor surface. Antigens are introduced and bind to the antibodies. The antigens are either labelled or induce a measurable change in the sensor (e.g. refractive index change). This assay can also be performed by immobilising antigens on the sensor surface and allowing antibodies to bind to them. The format is shown in Figure 2.20.

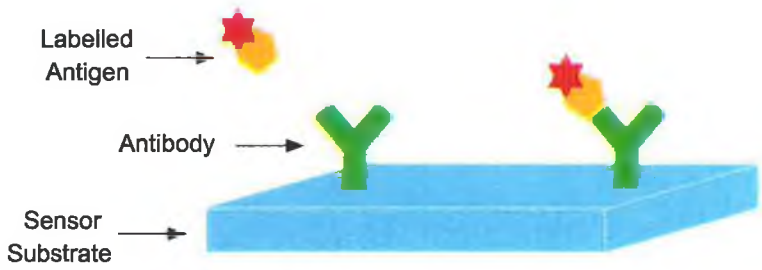


**Figure 2.20:** Schematic of direct binding assay format.

Sandwich assays also involve the immobilisation of antibodies, followed by the attachment of antigens but in this case the presence of the antigen is detected by a second, labelled antibody. Figure 2.21 illustrates the binding format.

For sandwich assays to be effective, the antigen of interest must be large

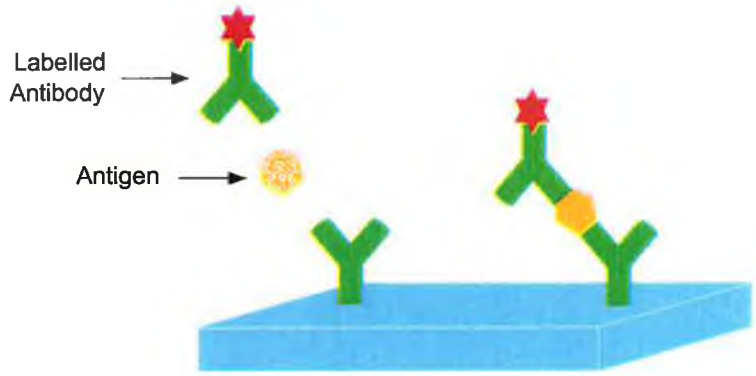


**Figure 2.21:** Illustration of sandwich assay, showing antigen sandwiched between labelled antibody and binding antibody.

enough, with sufficient available epitopes, to bind two antibodies simultaneously. A major advantage of this double binding is a reduction in the number of false readings. This is due to the fact that in order for an antigen to be detected it must bind to not just one, but two separate antibodies.

Antigens too small to stimulate antibody production are called haptens. They are typically less than 10,000 Daltons in weight. Daltons (Da) are atomic mass units used in biochemistry and molecular biology, with $1\,\mathrm{Da} = 1\,\mathrm{g\ mol^{-1}}$ [33]. In order for the haptens to be detected, it is necessary to conjugate (bind) them to larger carrier proteins [31]. Antibodies specific to the hapten conjugates can then be generated and sandwich assays carried out as described above.

A major advantage of sandwich assays is that, provided the antigen is large enough, they can provide signal amplification. A number of labelled antibodies can attach to each bound antigen. This means that the presence of each antigen is indicated by not one but several labelled antibodies. The principle is illustrated in Figure 2.22.

Unlike sandwich assays, competitive assays are capable of detecting antigens of less than $10,000$ Daltons. In competitive assays labelled and unlabelled antigens compete for antibody binding sites. Antibodies are immobilised on the sensor surface and a known quantity of labelled antigen is introduced, along with a test sample containing an unknown amount of antigen. The concentration of antigen in the test sample is determined by comparison with an inhibition curve that is generated by measuring the response from different fixed amounts of la-

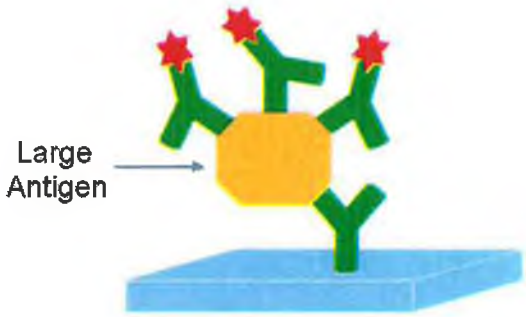


**Figure 2.22:** Illustration of amplification capability of sandwich assay. The presence of each antigen is indicated by not one but several labelled antibodies.

belled antigen and unlabelled antigen. A schematic of the assay format is shown in Figure 2.23.

**Figure 2.23:** Illustration of competitive assay.

One possible drawback of competitive assays is that there are several sample preparation steps, including labelling and mixing. This may not be a problem for some assays or immunosensors but it must be considered when deciding on the most suitable assay format.

The final immunoassay format is that of the displacement assay. These assays require immobilised antibodies to be saturated by labelled antigens. When a test sample containing the antigen of interest is introduced, the unlabelled antigens displace the bound labelled antigens. The quantity of antigens in the test sample can be determined by measuring the quantity of displaced labelled antigens. Figure 2.24 illustrates the process.

**Figure 2.24:** Illustration of displacement assay.

## 2.6 Conclusions

This chapter has detailed the sensing mechanism of the immunosensor developed in this work. Antibodies were introduced and described in terms of both their function and structure. The mechanisms involved in antigen binding were explained, with reference to the composition of antigen binding sites and the forces employed. In the final sections of the chapter, descriptions of the main immunoassay categories and formats were provided and reasons were given for the choice of fluorescently-labelled immunoassays.

# Bibliography

[1] J. Wang, "Electrochemical nucleic acid biosensors," *Analytica Chimica Acta*, vol. 469, no. 1, pp. 63–71, 2002.

[2] N. Bsat, M. Wiedmann, J. Czajka, F. Barany, M. Piani, and C. Batt, "Food safety applications of nucleic acid-based assays," *Food Technology*, vol. 48, no. 6, pp. 142–145, 1994.

[3] D. Chernoff, R. Miner, B. Hoo, L. Shen, R. Kelso, D. Jekic-Mcmullen, J. Lalezari, S. Chou, W. Drew, and J. Kolberg, "Quantification of cytomegalovirus DNA in peripheral blood leukocytes by a branched-DNA signal amplification assay," *Journal of Clinical Microbiology*, vol. 35, no. 11, pp. 2740–2744, 1997.

[4] S. Iqbal, J. Chambers, R. Brubaker, M. Goode, and J. Valdes, "Detection of Yersinia pestis using branched DNA," *Molecular and Cellular Probes*, vol. 13, no. 4, pp. 315–320, 1999.

[5] C. Villee, *Biology.* Philadephia: W.B. Saunders Company, 7th ed., 1977.

[6] N. Campbell, *Biology.* Redwood City: The Benjamin/Cummings Publishing Company Inc., 3rd ed., 1993.

[7] Z. Dai, F. Yan, H. Yu, X. Hu, and H. Ju, "Novel amperometric immunosensor for rapid separation-free immunoassay of carcinoembryonic antigen," *Journal of Immunological Methods*, vol. 287, no. 1-2, pp. 13–20, 2004.

[8] M. Minunni, S. Tombelli, A. Gullotto, E. Luzi, and M. Mascini, "Development of biosensors with aptamers as bio-recognition element: the case of HIV-1 Tat protein," *Biosensors and Bioelectronics*, vol. 20, no. 6, pp. 1149–1156, 2004.

[9] Z. Muhammad-Tahir and E. Alocilja, "A disposable biosensor for pathogen detection in fresh produce samples," *Biosystems Engineering*, vol. 88, no. 2, pp. 145–151, 2004.

[10] L. Bousse, R. McReynolds, G. Kirk, T. Dawes, P. Lam, W. Bemiss, and J. Parce, "Micromachined multichannel systems for the measurement of cellular metabolism," *Sensors and Actuators B: Chemical*, vol. 20, no. 2-3, pp. 145–150, 1994.

[11] J. Lin, F. Yan, X. Hu, and H. Ju, "Chemiluminescent immunosensor for CA19-9 based on antigen immobilization on a cross-linked chitosan membrane," *Journal of Immunological Methods*, vol. 291, no. 1-2, pp. 165–174, 2004.

[12] S. Sharma, N. Sehgal, and A. Kumar, "Biomolecules for development of biosensors and their applications," *Current Applied Physics*, vol. 3, no. 2-3, pp. 307–316, 2003.

[13] J. Langer, M. Filipiak, J. Kecinska, J. Jasnowska, J. Wlodarczak, and B. Buladowski, "Polyaniline biosensor for choline determination," *Surface Science*, vol. 573, no. 1, pp. 140–145, 2004.

[14] C. Mousty, "Sensors and biosensors based on clay-modified electrodes–new trends," *Applied Clay Science*, vol. 27, no. 3-4, pp. 159–177, 2004.

[15] H. Osada, S. Chiba, H. Oka, H. Hatafuku, N. Tayama, and K. Seki, "Noncontact magnetic temperature sensor for biochemical applications," *Journal of Magnetism and Magnetic Materials*, vol. 272-276, no. Supplement 1, pp. E1761–E1762, 2004.

[16] L. Mello and L. Kubota, "Review of the use of biosensors as analytical tools in the food and drink industries," *Food Chemistry*, vol. 77, no. 2, pp. 237–256, 2002.

[17] J. R. Retama, E. L. Cabarcos, D. Mecerreyes, and B. Lopez-Ruiz, "Design of an amperometric biosensor using polypyrrole-microgel composites containing glucose oxidase," *Biosensors and Bioelectronics*, vol. 20, no. 6, pp. 1111–1117, 2004.

[18] L. Zajoncova, M. Jilek, V. Beranova, and P. Pec, "A biosensor for the determination of amylase activity," *Biosensors and Bioelectronics*, vol. 20, no. 2, pp. 240–245, 2004.

[19] J. Yu, S. Liu, and H. Ju, "Glucose sensor for flow injection analysis of serum glucose based on immobilization of glucose oxidase in titania sol-gel membrane," *Biosensors and Bioelectronics*, vol. 19, no. 4, pp. 401–409, 2003.

[20] P. Leonard, S. Hearty, J. Brennan, L. Dunne, J. Quinn, T. Chakraborty, and R. O'Kennedy, "Advances in biosensors for detection of pathogens in food and water," *Enzyme and Microbial Technology*, vol. 32, no. 1, pp. 3–13, 2003.

[21] P. Dillon, B. Manning, S. Daly, A. Killard, and R. O'Kennedy, "Production of a recombinant anti-morphine-3-glucuronide single-chain variable fragment (scFv) antibody for the development of a "real-time" biosensor-based immunoassay," *Journal of Immunological Methods*, vol. 276, no. 1-2, pp. 151–161, 2003.

[22] M. McMahon and R. O'Kennedy, "The use of *in vitro* immunisation, as an adjunct to monoclonal antibody production, may result in the production of hybridomas secreting polyreactive antibodies," *Journal of Immunological Methods*, vol. 258, no. 1-2, pp. 27–36, 2001.

[23] J. Quinn, P. Patel, B. Fitzpatrick, B. Manning, P. Dillon, S. Daly, R. O'Kennedy, M. Alcocer, H. Lee, M. Morgan, and K. Lang, "The use of regenerable, affinity ligand-based surfaces for immunosensor applications," *Biosensors and Bioelectronics*, vol. 14, no. 6, pp. 587–595, 1999.

[24] B. Lu, M. Smyth, and R. O'Kennedy, "Immunological activities of IgG antibody on pre-coated Fc receptor surfaces," *Analytica Chimica Acta*, vol. 331, no. 1-2, pp. 97–102, 1996.

[25] I. Roitt, J. Brostoff, and D. Male, *Immunology.* Harcourt, 6th ed., 2001.

[26] N. Kimball, *Glossary of Biotechnology Terms.* Culinary and Hospitality Industry Publications, 3rd ed., 2002.

[27] D. Andersen and D. Reilly, "Production technologies for monoclonal antibodies and their fragments," *Current Opinion in Biotechnology*, vol. 15, no. 5, pp. 456–462, 2004.

[28] R. Edwards, *Immunoassays Essential Data.* Chichester: Wiley, 1996.

[29] M. Clarke, "Mike's immunoglobulin structure/function home page," *http://www.path.cam.ac.uk/ mrc7/mikeimages.html*, 2003.

[30] J. Gosling, *Immunoassays A Practical Approach.* New York: Oxford University Press, 2000.

[31] C. Janeway, P. Travers, M. Walport, and M. Shlomchik, *Immunobiology.* New York: Garland, 5th ed., 2001.

[32] D. Sears, "Immunology," *W. H. Freeman and Co. and Sumanas, Inc.*, 1997.

[33] P. Atkins, *Physical Chemistry.* New York: Oxford University Press, 6th ed., 1998.

[34] R. Rich and D. Myszka, "Why you should be using more SPR biosensor technology," *Drug Discovery Today: Technologies*, vol. In Press Corrected Proof, 2004.

[35] W. Robertson, *Surface Plasmon Resonance.* Middle Tennessee State University: http://physics.mtsu.edu/wmr/research.htm, 2004.

[36] L. M. May and D. Russell, "Novel determination of cadmium ions using an enzyme self-assembled monolayer with surface plasmon resonance," *Analytica Chimica Acta*, vol. 500, no. 1-2, pp. 119–125, 2003.

[37] T. Ozawa, M. Kakuta, M. Sugawara, Y. Umezawa, and M. Ikura, "An optical method for evaluating ion selectivity for calcium signaling pathways in the cell," *Analytical Chemistry*, vol. 69, no. 15, pp. 3081–3085, 1997.

[38] R. Rella, J. Spadavecchia, M. Manera, P. Siciliano, A. Santino, and G. Mita, "Liquid phase SPR imaging experiments for biosensors applications," *Biosensors and Bioelectronics*, vol. 20, no. 6, pp. 1140–1148, 2004.

[39] X.-L. Luo, J.-J. Xu, Y. Du, and H.-Y. Chen, "A glucose biosensor based on chitosan-glucose oxidase-gold nanoparticles biocomposite formed by one-step electrodeposition," *Analytical Biochemistry*, vol. 334, no. 2, pp. 284–289, 2004.

[40] I. Pastor, R. Esquembre, V. Micol, R. Mallavia, and C. Mateo, "A ready-to-use fluorimetric biosensor for superoxide radical using superoxide dismutase and peroxidase immobilized in sol-gel glasses," *Analytical Biochemistry*, vol. 334, no. 2, pp. 335–343, 2004.

[41] M. Voinova and M. Jonson, "Electronic transduction in model enzyme sensors assisted by a photoisomerizable azo-polymer," *Biosensors and Bioelectronics*, vol. 20, no. 6, pp. 1106–1110, 2004.

[42] P. Patel, "(Bio)sensors for measurement of analytes implicated in food safety: a review," *Trends in Analytical Chemistry*, vol. 21, no. 2, pp. 96–115, 2002.

[43] J. Evans, *HIV-1 Antibody Test*. McKesson Health Solutions LLC, 2004.

# Chapter 3

# Fluorescence Sensing: Principles and Techniques

## 3.1 Introduction

The immunosensor presented in this work is based on the detection of fluorescence from labelled antibodies or antigens. This chapter will detail the principles and techniques involved in fluorescence sensing. Fluorescence emission will be explained, along with references to fluorophores. Typical excitation sources and methods will be described. A detailed theoretical analysis of the two main excitation principles employed in the immunosensor presented here namely, waveguiding and evanescent field excitation, will be presented. Finally, a description will be provided of the fluorescence detection systems most commonly employed in fluorescence-based biosensors.

## 3.2 Photoluminescence

Photoluminescence occurs when photons are absorbed by an atom and subsequently re-radiated. It is caused by the photons interacting with the electrons of the atom and raising them to higher energy levels. In the process of returning to their ground level the electrons emit energy as photons. The principle is illustrated in Figure 3.1.

Photoluminescence is usually categorised as either phosphorescence or fluores-

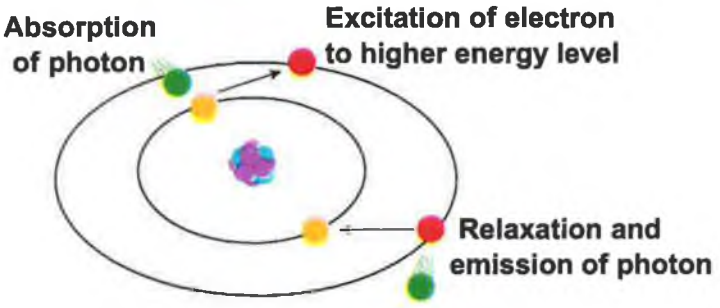


**Figure 3.1:** Illustration of principle of photoluminescence

cence. In the case of phosphorescence, the emission of light continues for a significant time (seconds) after the excitation has ceased, whereas for fluorescence, the emission of light occurs only over a short time scale (a typical emission lifetime is 10 ns) [1]. The reason for this difference is due to the behaviour of the excited electrons and the relative transition probabilities of the optical transitions.

In the case of fluorescence, when electrons in the ground state ($S_o$) are excited by photons, they are raised to higher energy levels such as the first or second states ($S_1$ or $S_2$). This is illustrated in the Jablonski diagram shown in Figure 3.2.

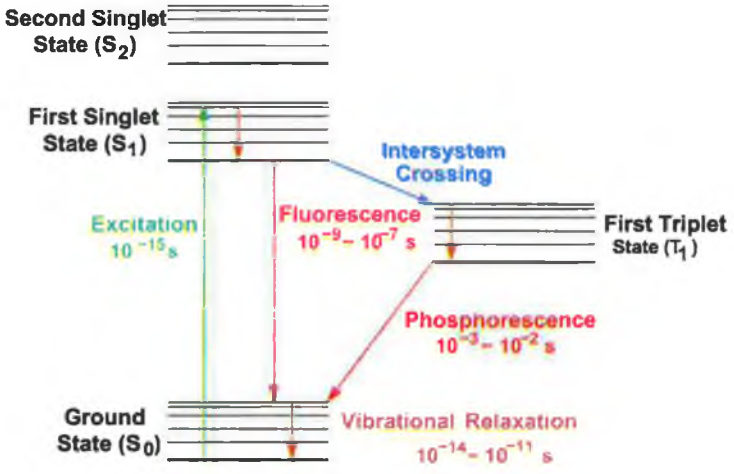


**Figure 3.2:** Jablonski diagram illustrating the emission of fluorescence and phosphorescence due to electron transitions from excited states to ground states.

After the initial excitation, internal conversion to the lowest first state occurs, followed by the electrons returning to the ground state, emitting photons in the process. In the case of fluorescence, the internal conversion to the lowest first

state occurs in approximately $10^{-12}$s. This is several orders of magnitude faster than the emission of fluorescence, which takes approximately $10^{-8}$s [1].

In the case of phosphorescence, after excitation to a higher state, the electrons de-excite to the first triplet state [1]. Transition from this state to the ground state is forbidden. As a consequence, the atom emits over a longer period as the electrons return to the ground state via low-probability processes. Such processes can include interaction with other molecules in the same triplet state or thermal energy raising the electron to a state from which it can de-excite [2].

For both fluorescence and phosphorescence, the amount of energy released during the relaxation to the ground state is less than that absorbed, meaning that the emitted light occurs at a higher wavelength (lower energy) than the excitation light. The difference in wavelength between absorbed and emitted light maxima is called the Stokes' Shift [1]. The absorption and emission spectra of the dye Pt(II)Porphyrin is shown in Figure 3.3, with Stokes' Shift indicated by the blue arrow.

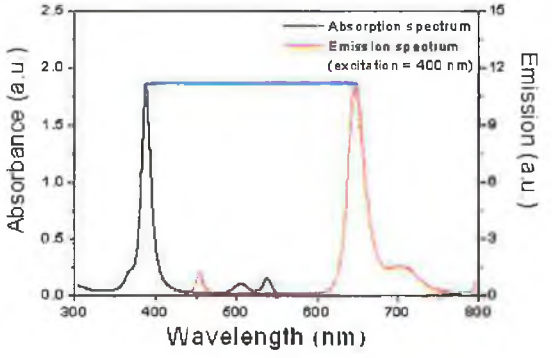


**Figure 3.3:** The absorption and emission spectra of the dye Pt(II)Porphyrin. Stokes' Shift is indicated by the blue line.

## 3.3 Fluorophores

Fluorophores are fluorescent molecules used as tags or labels in optical detection systems. There are two main features common to all fluorophores. The first is the obvious requirement that they produce fluorescence when excited at a particular wavelength. The second is that fluorophore molecules contain functional groups

that allow them to easily bind to the molecule to be detected. Other desirable attributes include high absorptivity, high fluorescence quantum yield, water solubility, pH insensitivity, low photobleaching (irreversible reduction of fluorophore intensity after sustained excitation) and low quenching upon conjugation (binding) to the host molecule.

The most commonly employed fluorophores in fluorescence biosensing include fluorescein, rhodamine and cyanine. The reason these are most widely used is due to the fact that they exhibit several of the above characteristics. Fluorescein, along with its most widely used derivative, fluorescein isothiocyanate (FITC), has relatively high absorption coefficient, excellent fluorescence quantum yield and good water solubility. Its excitation maximum of 495 nm closely matches the 488 nm spectral line of argon-ion lasers, which are often used in confocal laser-scanning microscopy and flow cytometry applications. Some of its drawbacks include its relatively high rate of photobleaching and the fact that its fluorescence is significantly reduced below pH7.

For the work presented here, cyanine dye was employed as the fluorescent label. The particular derivative used was Cy5, which is a fluorescent bifunctional NHS-ester, meaning that it has two amine binding sites. This facilitates binding of the Cy5 dye to antibodies, which have several available amine groups. The dye is also highly water soluble, which is an important requirement of the label, as antibodies are stored in aqueous solutions. Other advantages of Cy5 dye include its improved photostability compared to other dyes and the fact that it is insensitive to pH over a broad range.

As shown in the absorption and fluorescence emission spectra in Figure 3.4, Cy5 dye can be excited between 600 nm and 660 nm and emits an intense fluorescence in the far-red region of the visible spectrum (with a maximum signal at 670 nm). This means that low-cost, commercial, red laser diodes (see Section 3.4.1 for a detailed description of laser diodes) can be used as the excitation source.

A ruthenium dye complex, $Ru(dpp)_3$, was also employed for the work presented in Chapter 5, and will be described in detail in that Chapter.

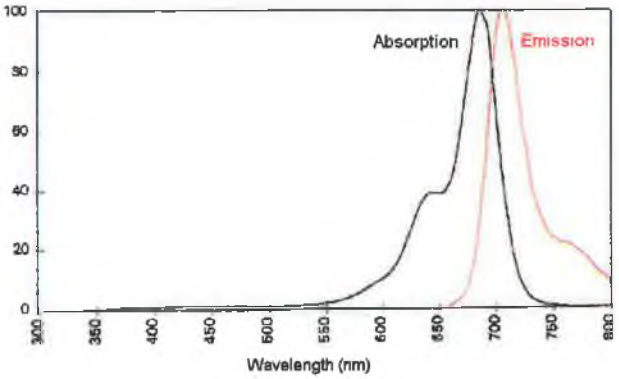


**Figure 3.4:** Absorption and emission spectra of Cy5 dye.

## 3.4 Excitation

### 3.4.1 Excitation Sources

Two main excitation sources were used in the work presented here. The first was a light emitting diode (LED), which is one of the most commonly employed excitation sources for sensing applications. LEDs are based on semiconductor p-n junctions or diodes. When the LED is forward biased, the electron-hole recombination gives rise to intense emissions across the bandgap of the material. Some of the reasons for the popularity of LEDs include the fact that they are small in size, inexpensive and have low power consumption. A few of the drawbacks associated with LEDs are that the emitted light is incoherent, uncollimated and is of a relatively broad bandwidth.

The second excitation source used in the work presented here was a laser diode. Laser diodes are simply LEDs that have been designed to produce coherent laser light. Like LEDs, they are small in size and, due to their low power consumption, can be powered by batteries. This makes them suitable for inclusion in portable sensor systems.

The excitation sources used in the work presented here were matched to the excitation maxima of the dyes employed. A 635 nm laser diode was used as the excitation source for the sensors employing Cy5 dye and a blue LED (460 nm) was used as the excitation source when the ruthenium dye complex, $Ru(dpp)_3$, was employed.

### 3.4.2 Waveguiding

One of the immunosensors developed in this work employed a waveguide as the sensor substrate, facilitating the use of evanescent wave excitation.

An optical waveguide is a dielectric medium that confines and guides optical electromagnetic waves [3]. Of particular interest to this work is the planar configuration, with an asymmetric slab waveguide being a commonly employed format e.g. a glass microscope slide coated with sensing layer [4]. The term *asymmetric* refers to the fact that the refractive index of the medium above the waveguide differs from the refractive index of the medium below. For ease of explanation, in this treatment the media above and below the waveguide shall be referred to as the layer and substrate respectively.

A generalised asymmetric slab waveguide is depicted in Figure 3.5, with $n_l$, $n_w$ and $n_s$ denoting the refractive indices of the layer, waveguide and substrate respectively. The thickness of the waveguide is indicated by $d$ and the incident angle by $\theta$.

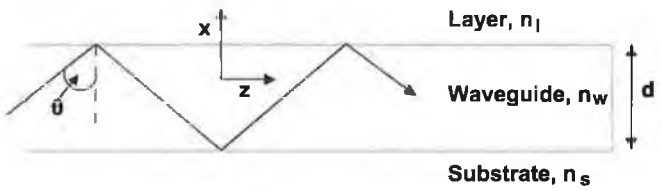


**Figure 3.5:** Schematic of an asymmetric slab waveguide.

A ray of light is guided down the length of the waveguide via total internal reflection. Total internal reflection occurs when the incident angle is greater than the critical angle [5]. From Snell's law, the critical angle is defined as:

$$\theta_c = \sin^{-1}(\frac{n_1}{n_2}) \tag{3.1}$$

where $n_2$ denotes the medium of higher refractive index and $n_1$ the medium of lower refractive index.

Therefore, the critical angles at the waveguide-layer interface and the waveguide-substrate interface can be defined as:

$$\theta_c^l = \sin^{-1}(\frac{n_l}{n_w}) \tag{3.2}$$

$$\theta_c^s = \sin^{-1}(\frac{n_s}{n_w}) \tag{3.3}$$

If $n_l > n_s$, which is the case in the work presented here, then $\theta_c^l > \theta_c^s$. This results in three possible angular ranges of $\theta$:

1. $90° > \theta > \theta_c^l$ : In this case, total internal reflection occurs at both the waveguide-layer interface and the waveguide-substrate interface, resulting in a guided mode. This is illustrated in Figure 3.6.

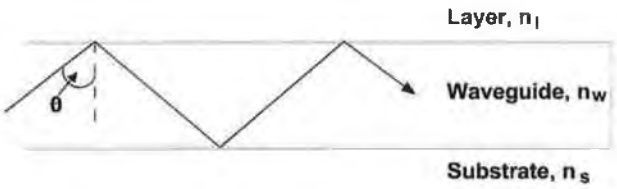


**Figure 3.6:** Guided mode.

2. $\theta_c^l > \theta > \theta_c^s$ : In this case, total internal reflection occurs at the waveguide-substrate interface but the light is free to leak into the layer as what is known as a "cover mode" (illustrated in Figure 3.7).

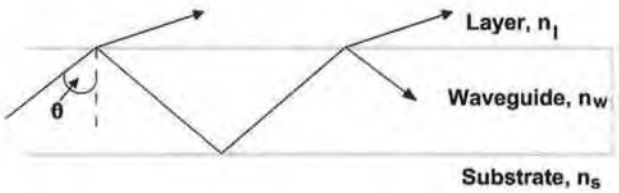


**Figure 3.7:** Cover mode radiation.

3. $\theta < \theta_c^s$ : If the incident angle is lower than the critical angle at both interfaces then the light is free to leak into both the layer and the substrate. An illustration of the resultant "substrate cover mode" radiation is shown in Figure 3.8.

Of the three angular ranges indicated, only the first allows waveguiding to occur over an extended distance.

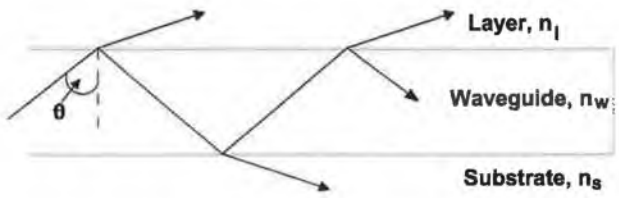


**Figure 3.8:** Substrate-cover mode radiation.

### 3.4.3 Evanescent Wave Excitation

When light propagates in a waveguide, an exponentially decaying tail of the field extends into the surrounding media. This is known as the evanescent field and is illustrated in Figure 3.9 [3].

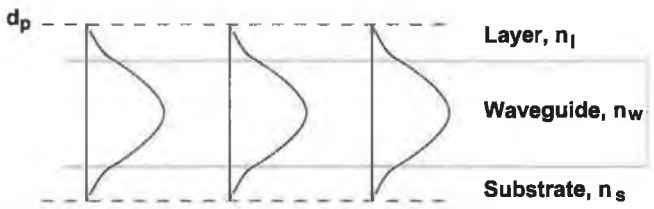


**Figure 3.9:** Illustration of exponential decay of evanescent field.

The field decays exponentially with distance from the waveguide according to the relation:

$$E = E_0 \exp\left(\frac{-z}{d_p}\right) \tag{3.4}$$

where $E$ and $z$ are the electric field amplitude and distance from interface respectively. The penetration depth, $d_p$, is the perpendicular distance from the interface at which the wave amplitude falls to 1/e of its initial value at the interface ($E_0$). The magnitude of $d_p$ is given by:

$$d_p = \frac{\lambda}{2\pi n_w(\sin^2\theta - (n_l/n_w)^2)^{1/2}} \tag{3.5}$$

where $\theta$ refers to the angle of incidence and all other symbols are as previously described.

As can be seen from Equation 3.5, $d_p$ is dependent on refractive index, wavelength and incident angle, which means that $d_p$ can be tuned by varying these

parameters. This has significant implications for sensing. The evanescent field can be used to selectively interact with entities at the waveguide surface. By tuning $d_p$, labelled molecules bound to the surface of the waveguide can be excited without exciting non-bound labelled molecules in the solution above, which lie out of the range of the evanescent wave.

In the initial immunosensor presented here (see Chapter 4), evanescent wave excitation is used to selectively excite surface-bound labelled antibodies.

### 3.4.4 Coupling

As the penetration depth of the evanescent field is dependent on the angle of incidence, it is necessary to have precise control over the coupling of light into the waveguide. Prism coupling, butt coupling and grating coupling are examples of some of the more commonly employed methods [6].

Initially, grating coupling was employed as the method of coupling for the first immunosensor presented in this work. This involved the fabrication of a sol-gel-based, periodic grating on the surface of a waveguide. The grating facilitated the phase matching of the incident beam with particular waveguide modes. Due to the low coupling efficiencies and high incident angle dependency of grating coupling this method was subsequently replaced with an alternative coupling method.

The method chosen was that of direct focusing, also referred to as *end-fire* coupling. End-fire coupling is a form of transverse coupling, where the incident beam of light is incident directly onto the exposed cross-section of the waveguide. Coupling occurs by matching the beam-field, e.g. Gaussian profile of laser beams, to the waveguide mode field [7]. Focusing of the incident beam is necessary to match its profile to that of the waveguide mode field. This aids in the reduction of energy loss into scattered fields. A schematic of the method is shown in Figure 3.10.

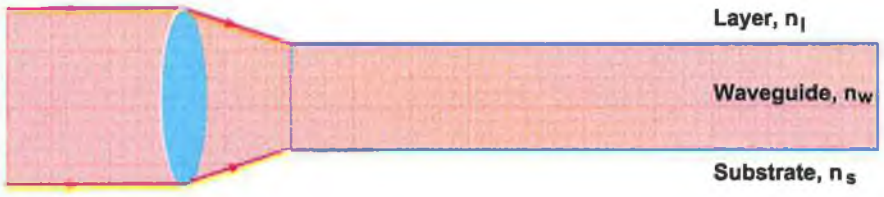


**Figure 3.10:** Schematic of coupling of a light beam into a waveguide using the end-fire coupling method.

## 3.5 Fluorescence Detection

### 3.5.1 CCD Camera

Charged coupled device (CCD) cameras are widely used for 2D detection. These are metal oxide semiconductor-based devices comprised of rows and columns of pixels, each of which converts photons into electrons. Photons striking the CCD surface excite the individual elements, elevating electrons to higher energy levels, eventually producing free charge. A positive voltage applied to an electrode at the pixel attracts the negatively charged electrons close to the area under the electrode and also repels any positively charged holes from the area. This forms a "potential well" beneath the electrode. The quantity of electrons collected (charge) is dependent on the number of photons striking the CCD, with a typical well capable of collecting 100,000 electrons before being saturated.

Though only a single electrode is required to form a potential well, each pixel consists of three electrodes. This facilitates the transfer of the charge out of the CCD, in order for it to be quantified. In order to collect the electrons, a positive voltage is applied to one of the electrodes. This is referred to as holding the electrode high (e.g. applying 12 V). The other two electrodes are kept low (e.g. 0 V). Once the charge is collected it can be moved by changing one of the low voltages to high. The charge is now shared between the two high electrodes. Reverting the initial electrode back to low ensures that the charge is transferred to the new electrode. Repeating the process will result in the charge progressing either down a column of pixels or across a row, depending on the orientation of the electrodes.

In the majority of CCD cameras, electrodes are arranged so that charge is

transferred downwards along the columns until it reaches the final row, where it is transferred off the CCD. It is then amplified and converted into a voltage. These voltages are then converted from analogue values into a digital form by the camera electronics, resulting in a 2D intensity image of the CCD array.

At room temperature, thermally generated noise, referred to as dark current, can result in the generation of thousands of electrons per pixel per second. Consequently, full well capacity of each pixel is reached within a few seconds. Cooling CCDs can significantly reduce the noise to only tens of electrons per pixel per second. Therefore, CCD cameras are often cooled in order to improve their performance.

### 3.5.2 CMOS Camera

Complementary metal oxide semiconductor (CMOS) cameras are similar in design and function to CCD cameras. The main difference lies in the electron to voltage conversion. In CCD cameras, this occurs after the collected charge has been removed from the pixel columns. However, in CMOS cameras, electron to voltage conversion takes place at each pixel and it is the voltage that is transferred along the columns.

In general, CMOS cameras offer superior power consumption compared to CCD cameras and due to the fact that less off-chip circuitry is required, they are typically smaller in size. These advantages are usually offset by the superior noise performance of CCD cameras, which occurs as a result of their employing less on-chip circuitry.

Both CCD and CMOS cameras were employed in this work.

## 3.6 Conclusions

In this chapter, the optical phenomena relevant to the development of the immunosensor reported in this work have been presented. Fluorescence was described in terms of electron activity and explained with the aid of energy level diagrams. A brief overview of fluorophores was provided. Excitation sources commonly employed in fluorescence-based biosensors were explained. The principle of waveguiding was introduced and the conditions under which it can occur

were stated. Evanescent wave excitation was explained and the importance of its tunable penetration depth was highlighted. The strategy by which light was coupled into the sensor platform was outlined and finally, each of the fluorescence detection sources employed in the work presented here were described and compared.

# Bibliography

[1] J. Lakowicz, *Principles of Fluorescence Spectroscopy.* New York: Kluwer Academic/Plenum Publishers, 2nd ed., 1999.

[2] B. Herman, V. C. Frohlich, J. Lakowicz, D. Murphy, K. Spring, and M. Davidson, "Basic concepts in fluorescence," *Olympus America Inc.*, http://olympusmicro.com/primer/techniques/fluorescence/fluorescenceintro.html, 2005.

[3] G. Smith and T. King, *Optics and Photonics: An Introduction.* Chichester: Wiley and Sons Ltd., 2000.

[4] F. Ligler and C. R. Taitt, *Optical Biosensors: Present and Future.* Amsterdam: Elsevier, 2002.

[5] E. Hecht, *Optics.* San Francisco: Addison Wesley, 4th ed., 2002.

[6] T. Tamir, *Integrated Optics.* New York: Springer-Verlag, 1979.

[7] R. Hunsperger, *Integrated Optics:Theory and Technology.* Newark: Springer-Verlag, 3rd ed., 1991.

# Chapter 4

# Development of Planar Immunosensor

## 4.1 Introduction

In order to successfully achieve the objective of developing a generic, low-cost, effective immunosensor, it was necessary to investigate and combine a range of experimental techniques, namely, immobilisation strategies, patterning methods, optical excitation and detection and image analysis. This chapter describes the development and integration of these techniques to yield a planar optical immunosensor.

## 4.2 Antibody Preparation

### 4.2.1 Assay Format

The assay format chosen for the immunosensor presented here was that of a sandwich assay. As described in Section 2.5.3, the first stage of a sandwich assay is the immobilisation of capture antibodies on the sensor substrate. The antigen of interest is then introduced and binds specifically to the immobilised antibodies. The presence of the antigen is indicated by introducing fluorescently-labelled antibodies, which attach to the bound antigens. Using an appropriate detector, the fluorescence signal is imaged and correlated to the antigen concentration. The overall assay configuration is illustrated in Figure 4.1.

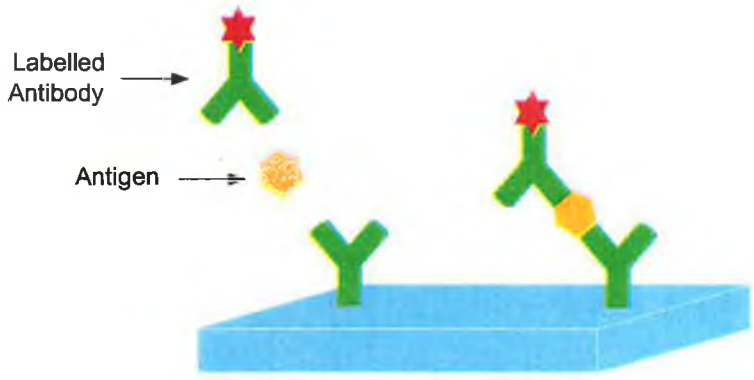


**Figure 4.1:** Sandwich assay format, illustrating an antigen sandwiched between labelled antibody and binding antibody.

There were several reasons for choosing this sandwich assay format. It is a relatively simple assay to perform, with each of the solutions (i.e., antibody, antigen and labelled antibody) being introduced separately. The main advantage of this assay is that the antigen does not need to be mixed or labelled. One possible drawback of using a sandwich assay format is that, unless the antigen is coupled to larger molecules, only relatively large antigens are capable of being detected. This is due to the fact that the antigen must attach to both the capture antibody and the labelled antibody (see Section 2.5.3 for more information). However, binding to two antibodies also provides an advantage over other assay formats as it helps to reduce the number of false readings, due to the fact that antigens are detected only when they bind to two separate antibodies.

### 4.2.2 Antibody/Antigen Selection

The initial antigen/antibody pair chosen to demonstrate the proof of principle immunosensor was that of bovine serum albumin (BSA) and its corresponding antibody; anti-BSA. Albumin is the most common protein in blood plasma, with BSA being the most common protein in bovine blood plasma. There were several reasons for choosing this antigen and corresponding antibody.

With a mass of approximately 60 kDa and a diameter of approximately 6 nm, BSA was large enough, with sufficient epitopes to bind to two antibodies simultaneously. This facilitated the use of the sandwich assay format. BSA is readily

available in its purified form and relatively large quantities (grams) can be purchased at a relatively low cost. This is unlike many other antigens that are quite expensive and available only in $\mu$g quantities. The reason BSA is so readily available is due not only to the fact that it is the most common protein in blood plasma but that it is also a good immunogen, meaning that it generates a large quantity of high affinity antibodies. As a result of its availability and good immunogenic properties, BSA is well characterised, making it a good choice for the development of the proof of principle immunosensor presented here.

### 4.2.3 Purification

In order to increase the antibody specificity, the anti-BSA antibodies were affinity-purified before being immobilised on the substrate surface. A polymer cylindrical column with an opening at one end and a narrow outlet at the other was filled with Sepherose gel linked with BSA. Sephersose gel (AGB, Dublin) is comprised of polymer beads of sufficient diameter to allow labelled-antiBSA antibodies to filter slowly between the beads once they are packed into the column. Tubing was attached to the outlet at the base of the column and connected to a flowcell positioned in a UV spectrometer. Anti-BSA antibodies were then injected into the column and, after 20mins, phosphate buffer saline (PBS) Tween was passed through the column to remove unbound antibodies. PBS was then passed through to remove any traces of PBS Tween. In order to break the bonds between the BSA molecules and anti-BSA antibodies, a solution of low pH (referred to as an elution buffer) was passed through the column. The antibody solution was collected in aliquots after it had passed through the flowcell and spectrometer (which was used to measure the absorbance of the eluted solution at 280 nm). Anti-BSA antibodies absorb at 280 nm and, as a consequence, a high absorbance corresponds to a solution containing a high concentration of antibodies specific to BSA.

### 4.2.4 Antibody Labelling

Purified antibodies were divided into two separate solutions. The first solution was used as the capture antibody stock and the second solution was used for the antibody labelling step. The label chosen for use in the immunosensor presented

here was the cyanine dye, Cy5, which was explained in detail in Section 3.3. The Cy5 dye was added to pH9.3 buffer solution containing the antibodies and incubated at room temperature. After 30 mins, with additional mixing of the solution every 10 mins, the antibodies were fully labelled.

### Separation of labelled antibody from free dye

Upon completion of labelling, it was necessary to remove any unconjugated dye in order to prevent it from interfering with antigen attachment or giving rise to false readings.

In order to separate the antibody from the free dye, two different methods were employed. The first method was dialysis. The labelled antibody solution was pipetted into dialysis tubing, which was then sealed at both ends. The dialysis tubing contained pores of a size that allowed passage of free dye but blocked the larger dye-labelled antibodies. The filled tubing was stirred in a pH7 PBS solution overnight. This stage was carried out in a cold room as prolonged storage of the antibody solution at room temperature results in a reduction in antibody activity. After stirring, unbound dye present in the antibody solution had filtered through the tubing into the PBS solution, leaving only labelled antibody remaining within.

The second free dye separation method employed was Gel Permeation Chromatography (GPC). In GPC, a glass cylinder (typically 10mm in diameter and 500 mm to 1000 mm in length) is packed with beads of a known pore size and solvent is passed through. The sample requiring separation is dissolved in the same solvent and added to the column. The rate of passage of the molecules present in the sample is affected by their size. Molecules larger than the pores continue following the solvent flow. However, diffusion causes molecules smaller than the pores to be drawn into the beads before continuing down the column. Consequently, molecules larger than the pore size reach the base of the column before molecules that are smaller than the pore size.

In order to remove the free dye from the labelled antibody solution, a GPC column was packed with polystyrene beads with pore sizes larger than Cy5 dye but smaller than the labelled antibodies. PBS was passed through the column and the antibody solution was then added. Two bands were formed, each travelling at a different rate through the column. The first contained the labelled antibodies,

with the second being comprised of the dye molecules. This formation of two bands permitted the labelled antibodies to be collected separately from the free dye. The process is illustrated in Figure 4.2

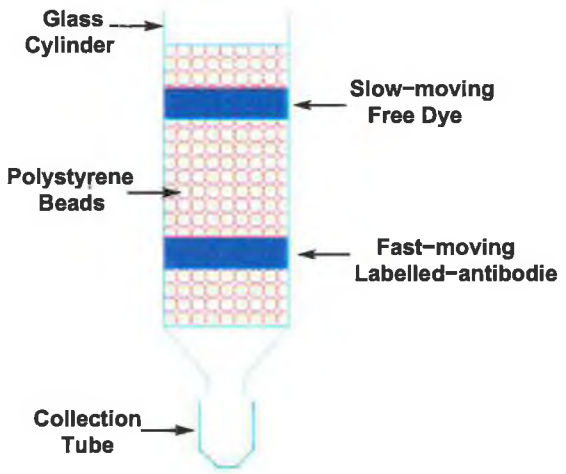


**Figure 4.2:** Separation of free dye from labelled antibody using a gel-filtration column.

### Calculation of Dye to Antibody Ratio

Gruber et al. demonstrated reduced fluorescence emission for IgG antibodies labelled with 6 dye molecules when compared to antibodies labelled with fewer dye molecules [1]. Therefore, for the antibodies employed in this work, it was decided to use a dye to antibody ratio of less than 6.

It was not possible to quantify the exact number of dye molecules attached to each anti-BSA antibody but the average number was calculated from the ratio of the dye and antibody molecular concentrations. The molecular concentrations were determined using the dye and antibody absorption values and their molar extinction coefficients.

The molar extinction coefficient of Cy5 dye is supplied by the manufacturer as $250,000\,\mathrm{M^{-1}cm^{-1}}$ at 650 nm. It is measured at 650 nm as this is the wavelength at which maximum absorbance occurs. As the molar extinction coefficient varies for each antibody, there is no standard value. However, from Equation 4.1 (Beer-Lambert Law), the slope of the straight line plot of antibody concentration versus

absorption is equal to the molar extinction coefficient (when l equals 1cm).

$$A = \epsilon c l \tag{4.1}$$

where $A$ represents absorbance, $\epsilon$ is the molar extinction coefficient, c is the antibody concentration and l is the optical path length. Therefore, plotting absorption at 280 nm for one of the batches of labelled anti-BSA antibodies used in this work (as the antibody absorption maximum occurs at this wavelength), the antibody molar extinction coefficient was determined to be 166,270.

Following the determination of the extinction coefficient, the molar concentrations of the dye and antibodies were calculated using Equations 4.2 and 4.3. These are manipulations of the Beer-Lambert Law, using an optical path length of 1 cm (as absorbance values were determined using a cuvette of 1 cm diameter).

$$[Cy5] = \frac{A_{650}}{\epsilon_{dye@650}} \tag{4.2}$$

$$[Antibody] = \frac{A_{280} - [0.05 \times A_{650}]}{\epsilon_{antibody@280}} \tag{4.3}$$

where $[Cy5]$ represents the molar concentration of Cy5 dye, $[Antibody]$ represents the molar concentration of the labelled antibody solution, and all other symbols are as previously described. As antibodies do not absorb at 650 nm, the absorption that occurs at 650 nm is entirely due to the Cy5 dye. However, the absorption that occurs at 280 nm, though mainly due to the antibodies, is also partially due to the dye. The dye manufacturer states that the dye absorption at 280 nm is approximately 5 % of the absorption at 650 nm (hence the modification factor in Equation 4.3).

Substituting the absorption values and extinction coefficient yields:

$$[Cy5] = \frac{0.8932}{250,000} = 3.5728 \times 10^{-6} M \tag{4.4}$$

Similarly,

$$[Antibody] = \frac{(0.1932) - (0.05 \times 0.8932)}{166,270} = 8.9336 \times 10^{-7} M \tag{4.5}$$

Consequently, the dye to antibody ratio becomes:

$$\frac{Dye}{Antibody} = \frac{3.573 \times 10^{-6}}{8.934 \times 10^{-7}} = 4 \tag{4.6}$$

Therefore, for this particular example, 4 dye molecules attached to each antibody.

### 4.2.5 Determination of Antibody Activity

For the immunosensor to work effectively, it was essential that the range over which the antibody was sensitive to the antigen of interest was determined. Too few antigens present in the sample could result in no change in sensor response, while too many antigens could result in saturation of the binding sites.

The activity (sensitivity to BSA) of the anti-BSA antibodies was determined using an Enzyme-Linked Immunosorbent Assay (ELISA) (see Section 2.5.2 for more information on ELISAs). Microtitre plates were coated with 10 $\mu$g/mL of BSA in PBS. Once immobilised and shaken to remove unbound molecules, the plates were then coated with Milk Marvel (Chivers, Ireland) solution. This contains proteins of various sizes, which occupy areas on the plate uncoated by the BSA. Washing steps of PBS Tween and PBS were used to remove any unbound molecules. Dilutions of anti-BSA antibodies in PBS (from 1/200 to 1/1000000) were added to different wells of the microtitre plates and incubated to facilitate binding. Following binding, the plates were washed and a secondary, enzyme-linked antibody was added to each well. In this work, goat anti-rabbit Horse Radish Peroxidase conjugated antibody was used. After further incubation and washing, Peroxidase Substrate was added, which reacted with the enzyme-linked antibody. Horse Radish Peroxidase Substrate absorbs at 450 nm. Therefore, measuring the absorbance of each well at this wavelength, permitted the quantity of substrate (and consequently the quantity of antibody) present to be determined. A typical antibody activity graph obtained is shown in Figure 4.3.

Each point on the graph shown in Figure 4.3 corresponds to a different dilution of anti-BSA antibodies. The graph shows the limit at which a change in antibody concentration is no longer detectable. This value is known as the antibody titre. In Figure 4.3 the titre occurs at approximately a 1/100000 antibody dilution. Below this value, though the concentration of antibody decreased, no detectable change in absorbance was recorded.

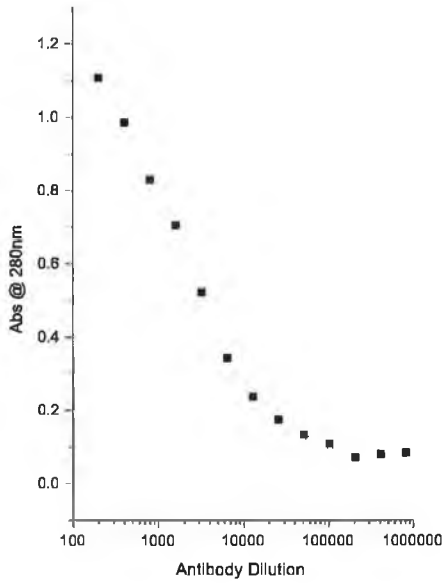


**Figure 4.3:** Activity graph of anti-BSA antibodies, measured using an Enzyme-Linked Immunosorbent Assay.

The graph was used to determine the optimum concentration of antibody to immobilise on the immunosensor substrate surface. The concentration that resulted in an absorbance equal to half the maximum absorbance value (referred to as the 1/2 max value) was chosen as the compromise between detectable signal and presence of excess antibodies. The 1/2 max value in Figure 4.3 lies at approximately 1/5000. Therefore the antibody stock solution was diluted by 5000 before being immobilised on the substrate.

## 4.3 Immobilisation

### 4.3.1 Antibody Functional Groups

The assay required the immobilisation of capture antibodies onto the substrate surface. It is possible to physisorb antibodies onto substrates (as occurs on the microtitre plates employed in ELISAs) but this is an unstable, uncontrolled attachment. In order to control surface coverage and antibody orientation it is necessary to covalently attach the antibodies to the sensor substrate.

The majority of IgG antibodies (the class used here) include side chains con-

taining amine groups or hydroxyl groups but due to the intrinsic variation between antibodies, these groups may exist in different locations on each. The same is true for carboxyl groups but there is a higher probability that they occur towards the base of the antibody Y-structure. Amine and carboxyl groups covalently bind to one another. Therefore, surfaces containing these groups allow antibody immobilisation. Due to their location on the antibody, the use of carboxyl groups increases the probability that antibodies will attach in an upright position, leaving the antigen binding sites free for attachment (see Section 2.4.1 for more information on antigen binding). In order for this to occur, amine groups must be available on the immunosensor surface.

It should be noted that it is also possible to cleave the arms of the antibody Y-structure in order to obtain access to the disulphide bonds present there. These could then be used to immobilise the antibody to the sensor surface. The primary advantage associated with this technique is an increased control over antibody orientation. However, it was decided that this level of optimisation was not required until the initial proof-of-principle sensor had been developed. Consequently, the immunosensor was designed to detect antigens using whole antibodies rather than fragments.

### 4.3.2 Silanisation of Glass Substrate

The immunosensor presented in this work employed a glass microscope slide as the sensor substrate. This is a standard substrate commonly employed in optical chemical and biosensors. The glass slide surface consists mainly of unreactive silica ($SiO_2$), which does not readily bind amine or carboxyl groups. Therefore, a chemical linker was required in order to attach antibodies to the glass surface.

Due to the fact that they are inexpensive and easy to use, with low energy reactions, the most commonly employed glass linkers are a family of chemicals called organosilanes [2]. These compounds, illustrated in Figure 4.4, are composed of hydrolysable groups (X), a spacing group (typically an alkyl chain) and an organofunctional group.

Following hydrolysis, the functional group X, typically an alkoxy or halogen, forms a reactive silanol group (Si-OH), which can condense with other silanol groups, for example those on the surface of glass slides, to form siloxane link-

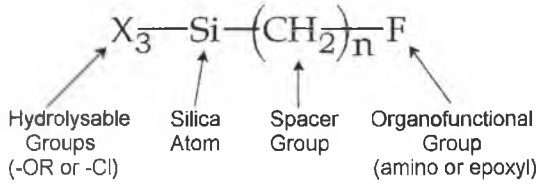


**Figure 4.4:** Illustration of organosilane structure.

ages. The functional group F is a nonhydrolysable organic group that possesses a functionality able to react with organic species (e.g. antibodies). Thus, use of the organosilane results in a covalent bond between organic species and inorganic substrates.

For the immunosensor presented here, several silane linkers were tested, each with different F functionalities such as amino (-NH2), mercapto (-SH) and glycidoxy functions. The final choice of organosilane; 3-glycidoxypropyltrimethoxysilane, was dictated by the optimum coverage and ease of implementation.

As the coverage of organosilanes on the substrate surface is mainly dependent on the density of reactive hydroxyl groups, a pre-treatment of the glass slides was carried out in order to increase the number of silanol groups present. This was achieved by treating the glass slides with $1\,\mathrm{mol/L}^{-1}$ sodium hydroxide (NaOH) solution. The substrates were then immersed in a solution containing the organosilane and the methoxy groups of the organosilane reacted with the Si-OH groups of the glass slides to covalently bind the organosilane to the surface. This resulted in epoxyl functional groups being made available for the binding of organic compounds required for antibody attachment. The process is shown in Figure 4.5.

### 4.3.3 Biolinkage

A biolinkage layer was employed to attach the antibodies to the functional group of the organosilane. Two separate biolinker layers were investigated for use with the immunosensor presented here. The first was the commonly-employed avidin-biotin system [3].

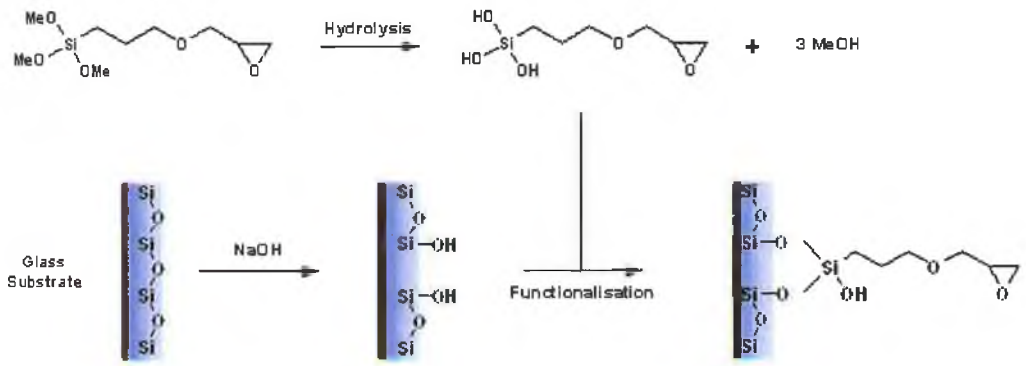


**Figure 4.5:** Schematic of covalent binding of organosilane to glass surface.

### Avidin-Biotin System

Avidin is a protein that is present in egg whites. Biotin is a vitamin of the B complex, which are a group of water-soluble vitamins that include riboflavin, folic acid and vitamin $B_{12}$. The major distinguishing feature of these two molecules is the extremely high affinity they have for each other ($K_a = 10^{15}M^{-1}$). To put this in perspective, it should be noted that a $K_a$ value of $> 10^7M^{-1}$ typically denotes antibodies with high affinity. The affinity of biotin for avidin is several orders of magnitude higher than this. Avidin also has four binding sites for biotin, which increases the number of possible reactions, configurations and applications of the avidin-biotin system.

The high affinity was exploited in the immunosensor presented here by attaching biotin to the capture antibodies (what is known as biotinylation) and attaching avidin to the silanised surface of the glass slide. When the biotinylated antibodies were passed over the surface they attached to the avidin molecules and became bound to the substrate.

### Protein A

Though the avidin-biotin system successfully bound the capture antibodies, the procedure was quite lengthy and complicated. Therefore, an alternative method was investigated. A single biolinker molecule, Protein A, was used to bind the capture antibodies to the functional group of the silane. Protein A is a protein

produced by staph bacteria, which live harmlessly on the skin surface. It displays a strong affinity for the Fc portion of the IgG antibody.

The covalent attachment of Protein A to the epoxy terminus of the silane, 3-glycidoxypropyltrimethoxysilane, occurs via its amine and carboxyl functional groups. The mechanisms of these two reactions are shown in Figure 4.6.

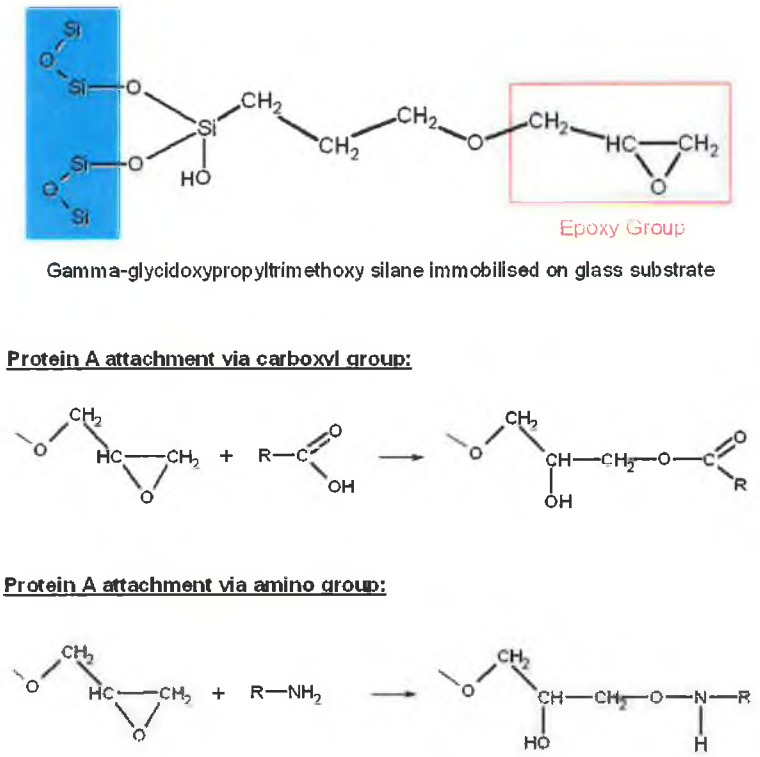


**Figure 4.6:** Mechanisms of covalent attachment of Protein A to organosilane.

The use of Protein A in place of the avidin-biotin system provided several advantages. The Protein A procedure required shorter preparation time, used less hazardous chemicals and required no pretreatment of the antibody. An added advantage of employing Protein A was that its binding reaction is reversible, which allows the same immunosensor platform to be used repeatedly if required.

### 4.3.4 Non-Specific Binding

Immunosensors are based on the specific recognition of an antibody for its antigen. A problem inherent in immunosensors is non-specific binding, which can occur

in several different forms. Sources of non-specific binding include the binding of antigens to the substrate rather than to their antibodies, labelled antibodies binding to the substrate rather than to the antigens and capture antibodies binding molecules other than the antigen of interest. Strategies to prevent non-specific binding must be implemented.

Four non-specific binding preventative measures were employed in the work presented here. Two were implemented during the antibody preparation stages (measures 1 and 4 listed below) and two were implemented during the assay stages (measures 2 and 3):

1. Antibodies were affinity-purified, which increased their sensitivity and reduced the chance of them binding to molecules other than the antigen of interest.

2. Capture antibodies, labelled antibodies and antigens were all spatially separated on the substrate surface. Their channels crossed paths at a single location. This meant that only sensor responses from this position could be attributed to antigen binding.

3. A blocking step was introduced after the capture antibodies had been immobilised, meaning that the antigens could bind only to the capture antibodies and the labelled antibodies could bind only to the antigens.

4. Before being passed over the substrate, the labelled antibodies were mixed with a small quantity of the protein used to block the sensor surface (see previous point). This was to ensure that any antibodies specific to the protein rather than the antigen bound to the free proteins instead of those on the substrate surface.

## 4.4 Patterning

### 4.4.1 Arraying

An Affymetrix 417 Arraying system was employed to pattern the capture antibodies onto the sensor substrate. The Arrayer is based on pin-and-ring technology, in which a metal ring is immersed into the solution to be spotted. When the ring is

drawn out, it contains a meniscus of the solution. A pin is moved down through the meniscus, piercing it and retaining a droplet of the solution on its tip. When the pin is brought into contact with a surface, it deposits the solution.

The Arrayer is capable of printing spots sizes of 150 $\mu$m diameter with a standard deviation of 10 %. Each ring pickup consumes approximately 1.5 $\mu$L of solution and it was possible to pattern 400 spots from each pickup. The Arrayer is also capable of printing approximately 4 spots per second, which facilitates rapid sensor production.

In the work presented here, the Arrayer was used to print an array of antibodies at specific locations on a glass slide that had been treated as described in Section 4.3. Figure 4.7 shows an example of fluorescence recorded from an array of Cy5-labelled anti-BSA antibodies printed using the Arrayer.

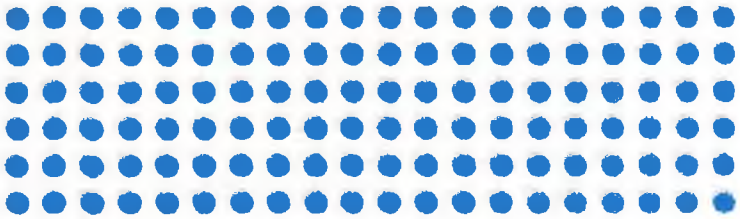

**Figure 4.7:** Array of Cy5-labelled anti-BSA antibodies printed using the Affymetrix 417 Arrayer. Antibodies spots sizes are approximately 150 $\mu$m in diameter. The antibodies were imaged using a Gentic Microsystems fluorescence scanner.

### 4.4.2 Microfluidics

Upon patterning of the capture antibodies onto the sensor substrate, the next step required was the introduction of the antigens and labelled antibodies. This was accomplished using a flowcell fabricated from poly(dimethylsiloxane) (PDMS) (Dow Corning). PDMS is a silicone rubber formed from liquid prepolymer and curing agent. The two are mixed together and cast against an appropriate master. The PDMS is then cured at an elevated temperature in order to facilitate cross-linking. Following curing, the resultant PDMS mould is peeled from the master. The concept is illustrated in Figure 4.8.

In the work presented here, the liquid prepolymer was cast against an aluminium master containing two ridges (1 mm x 2 mm x 8 mm), with upright cap-

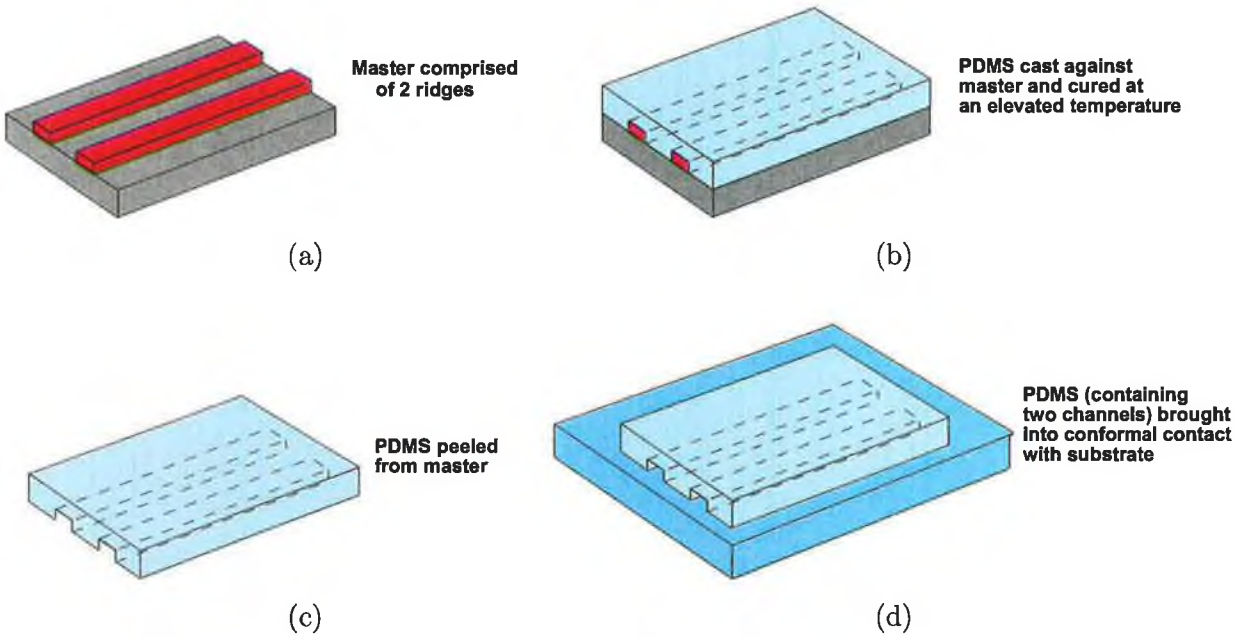


**Figure 4.8:** Illustration of the fabrication of a PDMS flowcell. PDMS is cast against a channel master and cured at an elevated temperature. The resultant mould is peeled from the master and brought into conformal contact with the substrate, where it seals and acts as a flowcell.

illary tubes positioned at each end. It was then cured at 70°C for 1 hour. Upon solidification, the PDMS mould was peeled from the master, with the resultant mould containing recessed channels of identical dimensions to the ridges of the master. The mould was brought into contact with the sensor surface to form a seal and act as a flowcell.

In order to provide tubing support, capillary tubes were inserted into the inlets and outlets of the flowcell, which were formed from the capillary tubes of the master. Tubing was connected to these tubes and a peristaltic pump was used to flow solutions through the channels.

Having established the viability of the initial flow system, the dimensions of the channels were decreased in order to reduce the volume of solution required to fill them. The aluminium master was replaced by one formed from SU-8 photoresist (Microchem, U.S.A.). SU-8 is a negative tone photoresist. When exposed to light of an apropriate wavelength, these exposed areas become resistant to chemical etching. Consequently, it is often employed in the production of templates as its unexposed areas can be removed, resulting in the formation of patterned coatings on the substrate.

The pattern formed on the surface is determined by the photomask employed. By blocking light from reaching certain areas of the photoresist and allowing others to be exposed, the pattern formed on the surface takes the form of the photomask.

In the work presented here, high resolution printing was employed to fabricate the photomask. The required design was produced using CAD software and printed onto acetate using high-resolution printing.

A portion of a silicon wafer was coated with SU-8 photoresist via the technique of spin-coating [4]. UV radiation, passed through the photomask, initialised cross-linking of the exposed areas of the SU-8 film. A thermal curing step, referred to as the post-bake exposure, completed the cross-linking. The uncross-linked (i.e. unexposed) areas were then removed through the use of the relevant solvent, leaving a positive relief pattern, which took the form of the design of the photomask. Here, the positive relief took the form of two ridges, with their height determined by the thickness of the SU-8 film. The ridge dimensions were 3 mm x 200 $\mu$m x 440 $\mu$m.

PDMS was moulded against the SU-8 master and cured. Once cured, the

flowcell was peeled from the master and the end of each channel was pierced with a needle to form the inlets and outlets. The flowcell was then brought into conformal contact with the surface of the sensor substrate. Tubing was attached to the end of each needle and a peristaltic pump was used to pass the antigen and labelled antibody solutions over the sensor surface.

### 4.4.3 Methodology

The flowcell was employed to introduce the antibody and antigen solutions to the surface of the sensor substrate and to provide spatial resolution. This meant that the signal due to antigen binding could be discriminated from certain non-specific binding events.

The flowcell was positioned on the surface of the substrate so as to include the immobilised capture antibodies within its channels (see Figure 4.9 (b)). Antigens were introduced into one of the flowcell channels and a PBS buffer solution was introduced into the second channel. Upon completion of binding, PBS Tween was passed through the channels to remove unbound antigens. PBS was then passed through the channels to remove all traces of PBS Tween.

The flowcell was then removed and a second was positioned on the slide at right angles to the previous flowcell (as shown in Figure 4.9 (c)). Labelled antibodies were introduced into both channels and bound to the immobilised antigens. After binding had occurred, the two washing steps of PBS Tween and PBS were carried out.

The nature of the patterning resulted in the formation of the three layers necessary for the sandwich assay at only one location on the chip. This point is indicated as B in Figure 4.9. Consequently, it is the fluorescence recorded solely at this point that is related to sensor response. Point A indicates an area on the chip where only capture and labelled antibodies are present. Therefore, the fluorescence recorded due to non-specific binding at this point serves as a background signal. This signal level is subtracted from the sensor signal level recorded at point B, yielding the final antigen dependent reading.

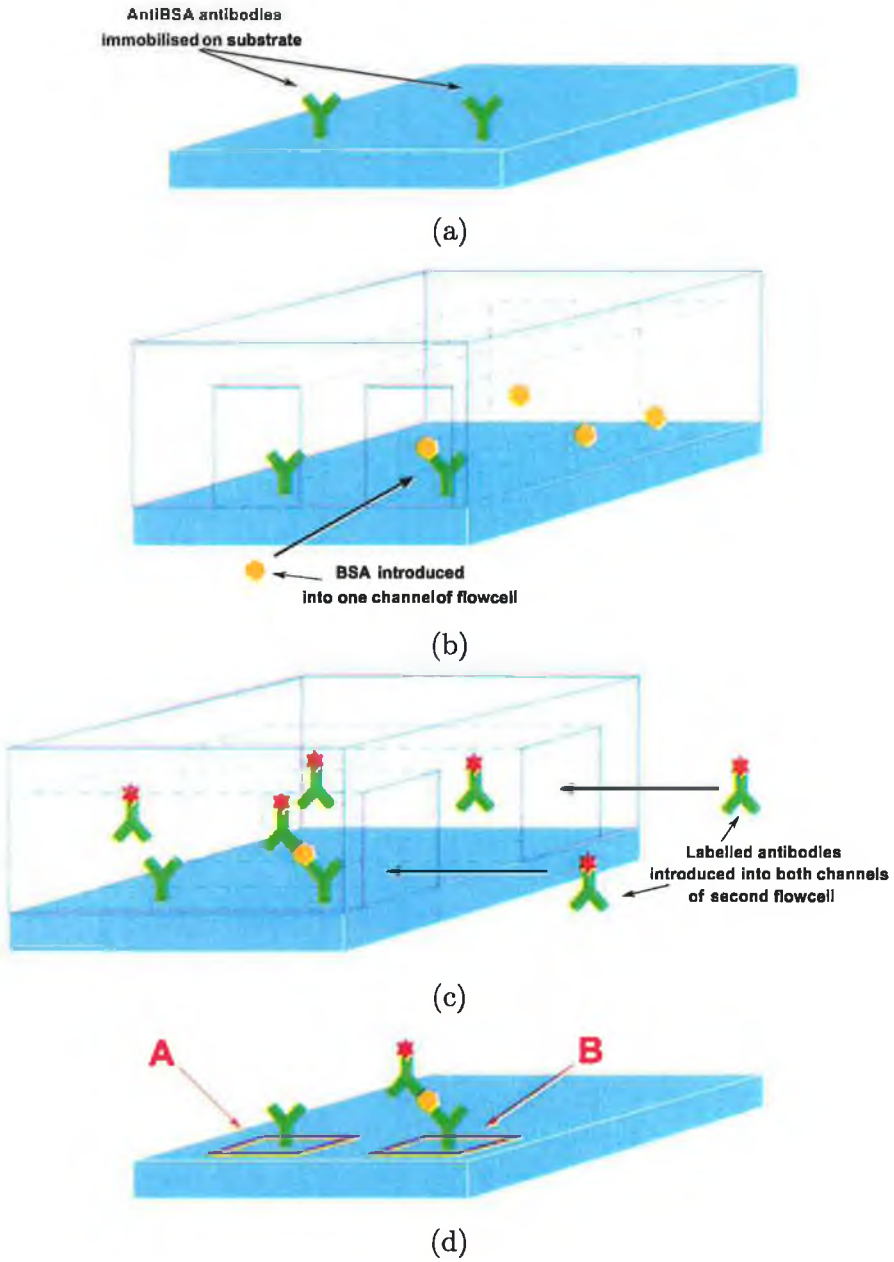


**Figure 4.9:** Illustration of the patterning of each layer of the antibody sandwich assay. Antibodies immobilised on substrate (image (a)). Image (b) shows the position of first flowcell, with buffer passed through the first channel and antigen through the second. Image (c) shows the position of the second flowcell, with labelled antibodies passed through both channels. Image (d) illustrates the combined result of all three layers, with no fluorescence detected at position A but fluorescence detected at position B, indicating the presence of antigens in the sample solution.

## 4.5 Experimental and Analysis Systems

### 4.5.1 Excitation

It is clear from the previous section that the presence of the antigen is indicated by fluorescence at a particular point on the chip. It is, however, necessary to ensure efficient excitation of the fluorophore in order to obtain a fluorescence signal. In the immunosensor presented here, evanescent wave excitation was employed, making the sensing process surface-specific in nature (see Section 3.4.3 for a detailed explanation of evanescent wave excitation). This means that only those fluorophores bound to the sensor substrate (via antibody-antigen interactions) are optically excited, thereby eliminating the possibility of fluorescence excitation in the bulk solution.

Optical excitation was provided by a 635 nm laser diode. A laser diode was chosen due to its reduced size and power consumption compared to a conventional Helium-Neon laser. This was important in the context of ultimately producing a portable sensor. The wavelength of the laser diode was chosen to overlap with the absorption maximum of the Cy5 dye in order to achieve efficient excitation (see Section 3.3 for more information on Cy5 dye).

A line generator was attached to the output of the laser diode. This converted the circular profile of emitted light into a rectangular profile, which facilitated uniform illumination (and therefore excitation) of the sensor substrate. A patterned glass slide acted as the waveguide and a cylindrical lens was employed in order to focus the excitation beam sufficiently for coupling into the waveguide via its endface, as was discussed in Section 3.4.4. A schematic of the excitation setup is shown in Figure 4.10.

### 4.5.2 Detection

The fluorescence emitted by the labelled-antibodies was recorded using a Charge Coupled Device (CCD) Camera-based detection system. A schematic of the detection system is shown in Figure 4.11.

Cy5 dye has a fluorescence maximum at 670 nm. Therefore, in order to remove any excitation light, the emitted light was passed through a 670 nm bandpass filter before being collected by the CCD camera.

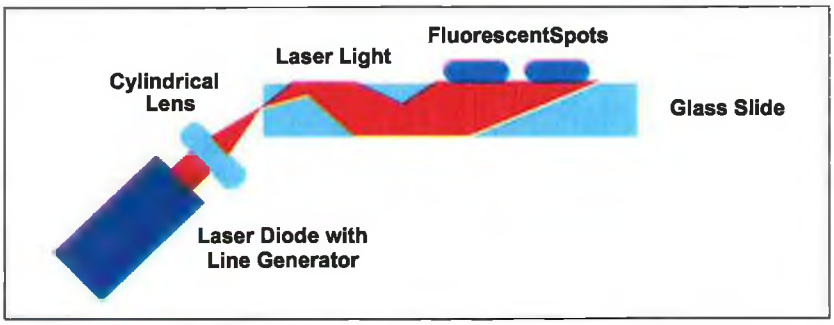


**Figure 4.10:** Schematic of fluorescence excitation setup

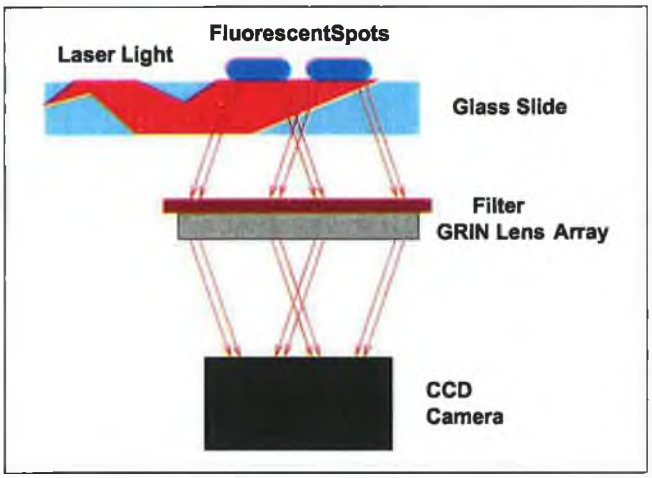


**Figure 4.11:** Schematic of immunosensor fluorescence detection system.

A graded index (GRIN) lens array was then employed to focus the light onto the CCD array. GRIN lens arrays are composed of an array of rod lenses, with the refractive index of each rod lens varying in a parabolic fashion along its length. This results in the redirection of light passing through the lens. The propagation paths in such lenses are illustrated in Fig. 4.12.

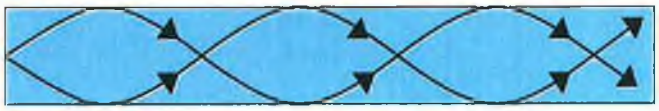

**Figure 4.12:** Illustration of light path through graded index (GRIN) lens.

By manufacturing these lenses to the correct length, light can be smoothly redirected to a specific point of focus. The GRIN lens employed here was manufactured to have an effective focal length of 8.89 mm. The GRIN lens created a 1:1, non-inverted image of the 2D surface of the substrate and as it was small, with a short effective focal length, it facilitated the miniaturisation of the setup.

The GRIN lens focused the emitted fluorescence onto the CCD array of a cooled CCD camera (Sensicam PCO) positioned at the effective focal length of the GRIN lens array. As the camera was cooled, its internal noise was kept to a minimum, thus increasing its detection capability. This was an important consideration due to the low light levels emitted by small concentrations of fluorescently-labelled antibodies (see Section 3.5 for a detailed explanation of CCD cameras). Another reason for employing a cooled CCD camera is the fact that it is capable of recording 2D images. This makes it possible to analyse several areas of the substrate surface simultaneously, thus facilitating multianalyte sensing.

### 4.5.3 Image Analysis

In order to determine the presence and concentration of antigens bound to the sensor substrate, the fluorescence intensity at two specific locations was required. The first occurred where the capture antibodies and labelled antibodies were present. The fluorescence intensity recorded at this location was subtracted from the fluorescence intensity recorded at the location where the capture antibodies, antigens and labelled antibodies were present. The difference in fluorescence

intensity between the two recorded images was attributed to the presence of the antigen.

In order to extract fluorescence intensity values from the recorded images and correlate them with antigen concentration, the image analysis software had to fulfill several requirements:

1. Determination of pixel intensity values.
2. Integration across defined areas in order to determine mean intensity values.
3. Background subtraction.
4. Normalisation against maximum value.
5. Comparison of mean intensity values.

Several commercial image analysis and modification software packages were investigated for suitability. These included Paint Shop Pro, Image Magic and IP Lab. The process that was finally selected involved using a custom-written C program, the majority of which was written by a colleague. The program converted the images to data files, which were then plotted and analysed using a second custom-written program, kindly supplied by another colleague. The Visual Basic front panel of this program is shown in Figure 4.13.

## 4.6 Sensor Performance

### 4.6.1 Validation Assay

Bovine serum albumin (BSA) and its associated antibody were chosen as the model system to validate the operation of the immunosensor. Polyclonal anti-BSA antibodies were purified and divided into two aliquots, one of which was labelled with Cy5 dye. A glass microscope slide was cleaned (using an acid wash), silanised and coated with Protein A. Using the Affymetrix Arrayer (see Section 4.4.1), an array of anti-BSA antibodies was then printed on the glass slide and the surface was blocked with Milk Marvel. Applying the methodology described in Section 4.4.3, a PDMS flowcell was used to pattern BSA, followed by labelled anti-BSA antibodies onto the glass substrate. The bound antibodies were

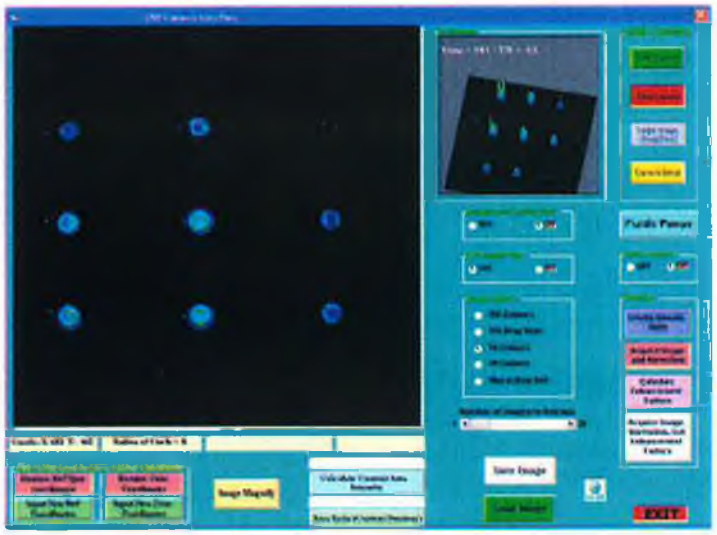


**Figure 4.13:** Visual Basic front panel of image analysis program.

excited and detected using the systems described in Sections 4.5.1 and 4.5.2. The resultant image, with the position of the control solution, BSA and labelled-antiBSA antibodies indicated, is shown in Figure 4.14.

### 4.6.2 Dose Response Curve

A full dose response curve was carried out in order to investigate sensor performance. A range of BSA concentrations was prepared and assays were carried out, as described in Section 4.6.1, with a different concentration of BSA being immobilised in each case. A single intensity value was determined by calculating the intensity within a fixed area (the section of the channel that intersected with the capture antibodies, Area B in Figure 4.14). Three replicates were carried out for each concentration of BSA (i.e. the assay was repeated three times for each concentration of BSA). Mean intensities values were calculated and used to determine standard deviations for each concentration. The resultant dose response curve is shown in Figure 4.15.

As expected, as the concentration of antigen decreased, the level of fluorescence decreased. A working range of greater than 100,000 ng/ml of antigen to 100 ng/ml was attained. Though antibodies vary in their sensitivity to different concentrations of antigens, the range obtained here is comparable to those

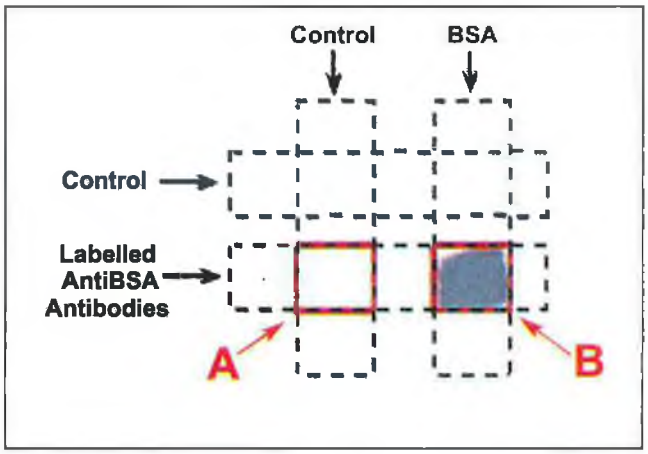


**Figure 4.14:** Image of fluorescence emitted from labelled anti-BSA antibodies, indicating presence of antigen (BSA) at point B. No fluorescence was detected at point A, as no BSA was present.

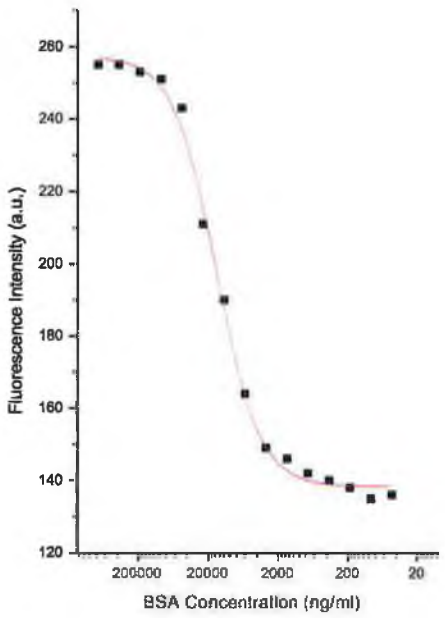


**Figure 4.15:** Dose response curve for BSA/anti-BSA assay, obtained using planar immunosensor.

achieved by similar immunosensors [5, 6].

The data was fitted into a sigmoidal four-parameter logistic equation, with $R^2 = 0.99719$ [5]. The minimal detectable signal (MDS) was calculated from the mean zero response plus $3\sigma$ (where $\sigma$ represents the standard deviation) of the response at this level. The mean zero response is the intensity value recorded when no antigen is present. With this system, an MDS of 137 was calculated, which corresponded to a limit of detection for BSA of approximately 150 ng/ml.

As the three lowest BSA concentrations all lie within the MDS it was not possible to determine if the limit of detection was due to the sensitivity of the antibodies employed or due to the MDS of the system. In order to determine this, an enhanced system, with a lower MDS would be required.

## 4.7 Conclusions

This chapter described each of the techniques and systems that were successfully developed and combined in order to produce an effective immunosensor. Development of five main areas was required for the fabrication of the immunosensor, namely antibody preparation; immobilisation; patterning; experimental and analysis systems; and validation.

Each of the steps involved in the antibody preparation, including purification and labelling, were described in detail in this chapter. Immobilisation strategies and methods were discussed, with reference to the functional groups available on the antibodies and the chemical linkers employed to immobilise them on the substrate. The patterning techniques investigated were then discussed and the methodology explained.

A description was given of the excitation, detection and analysis systems developed and optimised in order for the immunosensor to function effectively. The separate components employed were detailed, along with explanations of their functions.

Finally, the results from the validation assay and dose response curve obtained were presented. These results were comparable to similar immunosensors detailed elsewhere.

The planar immunosensor developed here served to validate the experimental techniques involved in the production of an optical immunosensor. The next stage

of this work was the progression to an enhanced optical biochip, the development of which is described in the following chapters.

# Bibliography

[1] H. Gruber, C. Hahn, G. Kada, C. Riener, G. Harms, W. Ahrer, T. Dax, and H. Knaus, "Anomalous fluorescence enhancement of cy3 and cy3.5 versus anomalous fluorescence loss of cy5 and cy7 upon covalent linking to igg and noncovalent binding to avidin," *Bioconjugate Chemistry*, vol. 11, no. 5, pp. 696–704, 2000.

[2] Gelest, "Silane coupling agents: Connecting across boundaries," *Gelest, Inc.*, 2004.

[3] D. Savage, *Avidin-Biotin Chemistry: A Handbook*. Pierce, 2005.

[4] B. Leyer, H. Knozinger, H. Schmelz, H. Gobel, H. Meixner, and T. Scherg, "Preparation of alvo4-films for sensor application via a sol-gel/spin-coating technique," *Thin Solid Films*, vol. 310, no. 1-2, pp. 228–233, 1997.

[5] M. Ngundi, L. Shriver-Lake, M. Moore, M. Lassman, F. Ligler, and C. Taitt, "Array biosensor for detection of ochratoxin a in cereals and beverages," *Analytical Chemistry*, vol. 77, no. 1, pp. 148–154, 2005.

[6] M. Diaz-Gonzalez, D. Hernandez-Santos, M. Gonzalez-Garcia, and A. Costa-Garcia, "Development of an immunosensor for the determination of rabbit IgG using streptavidin modified screen-printed carbon electrodes," *Talanta*, vol. 65, no. 2, pp. 565–573, 2005.

# Chapter 5

# Enhancement Strategies for Fluorescence-Based Sensors

## 5.1 Introduction

Efficient capture of fluorescence emission is an important factor in the performance of fluorescence-based biosensors. Higher levels of fluorescence increase the signal-to-noise ratio, which improves the sensor resolution. Methods of dramatically increasing the efficiency of fluorescence capture were predicted by the results of a theoretical analysis published previously [1]. The analysis examined the angular distribution of fluorescence emission from a fluorescent molecule on or near a surface. It was shown that, in such configurations, the fluorescence emission is anisotropic and that a considerable portion of the emission is emitted at angles that result in the light being confined within the substrate, with only a small fraction being transmitted through the substrate or into the environment above for detection.

Detailed analysis of these findings suggested two important research directions that impacted strongly on this work. The first was that redirection of the substrate-confined emission out of the substrate and towards the detector should result in a significant increase in the quantity of fluorescence captured. The second finding was that fluorescence from different positions is observed within different angular ranges. Therefore, via analysis of the fluorescence angular profile, it should be possible to distinguish between fluorescence from the surface and

that from the bulk solution.

Both of these predictions have important implications for fluorescence-based chemical sensors and biosensors. The significant increase in fluorescence capture efficiency would result in substantially lower limits of detection. The capability to distinguish between surface and bulk fluorescence would eliminate the necessity of removing a fluorescing bulk solution prior to detection. This would result in less complicated microfluidics and fewer steps in the assay, resulting in shorter measurement time and a simpler operational protocol. Another significant advantage of the ability to discriminate between surface and bulk fluorescence is the possibility of employing direct excitation (through the bulk solution). This would eliminate the need for the complicated optics associated with surface specific excitation, facilitating the production of simpler, more robust, portable sensors.

This chapter details the experimental verification of these two predictions, specifically

1. That the redirection of substrate-confined emission results in enhanced fluorescence capture efficiency, and

2. That it is possible to discriminate between fluorescence originating from the surface and fluorescence originating from the bulk solution comprising the environment.

## 5.2 Verification of Enhanced Fluorescence Capture

### 5.2.1 Angular Distribution of Fluorescence Emission

Work published previously in this laboratory showed that the angular distribution of fluorescence of a radiating dipole at a surface is highly anisotropic [1]. The resultant angular distributions are shown in Figures 5.1, 5.2 and 5.3, with the superscripts "l", "s", "a" and "w" corresponding to layer, substrate, air and water respectively. Figures 5.1 and 5.2 correspond to polar representations of the angular distribution and Figure 5.3 corresponds to a cartesian representation. In each case, the substrate employed in the model is glass, with Figure 5.1 corresponding to an air environment and Figure 5.2 corresponding to a water environment.

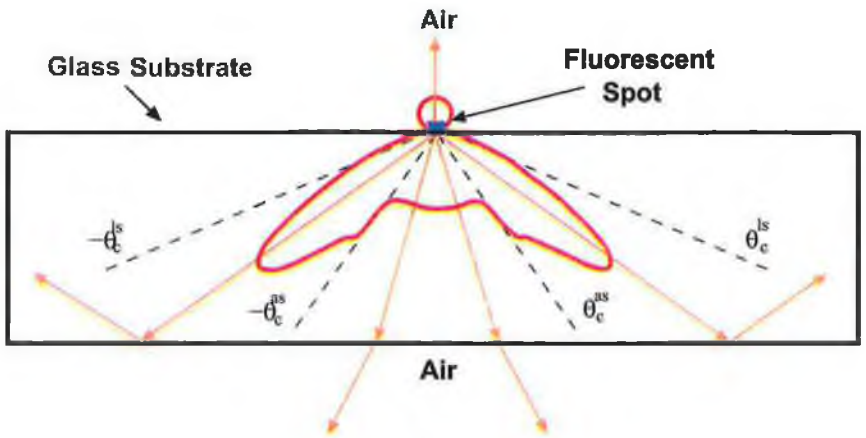


**Figure 5.1:** Angular distribution of fluorescence intensity radiated by a fluorescent spot situated on a glass substrate, which is surrounded by air.

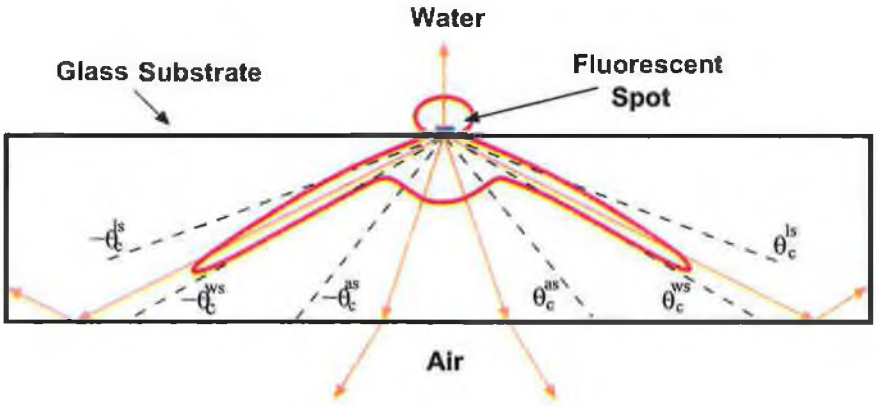


**Figure 5.2:** Angular distribution of fluorescence intensity radiated by a fluorescent spot situated on a glass substrate. The superstrate corresponds to a water environment.

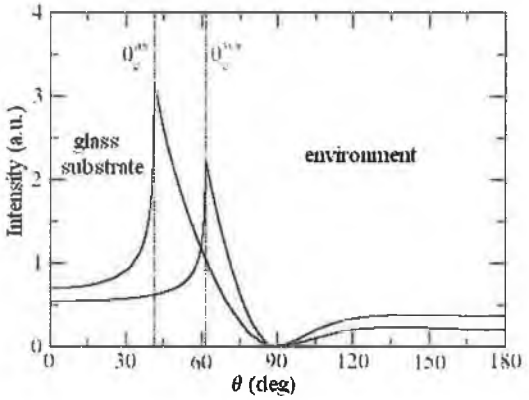


**Figure 5.3:** Cartesian representation of the fluorescence angular distributions. The solid and dashed lines correspond to the distributions in air and water environments, respectively, with $\theta_c^{as}$ corresponding to the critical angle of the air/glass interface and $\theta_c^{wis}$ corresponding to the critical angle of the water/glass interface. The intensities radiated into intervals $\theta \in \langle 0°, 90° \rangle$ and $\theta \in \langle 90°, 180° \rangle$ correspond to radiation into the substrate and environment, respectively.

Using these angular profiles, the fluorescence emission can be divided into four categories. The first category refers to the fluorescence emitted into the environment above the substrate (air in Figure 5.1 and water in Figure 5.2) and, for the purposes of this discussion, will be referred to as AT/WT (air-transmitted or water-transmitted). The second category refers to the fluorescence transmitted through the substrate into the environment below. This fluorescence occurs at angles $\theta \in \langle -\theta_c^{as}, \theta_c^{as} \rangle$, where, as stated previously, the superscripts "a" and "s" represent the air and substrate respectively. The angle of fluorescence emission is represented by $\theta$ and the relevant critical angle by $\theta_c$ (i.e. $\theta_c^{as}$ is the critical angle of the air/substrate interface). This fluorescence will be referred to as substrate transmitted (ST) fluorescence. The third category is that of the substrate-confined (SC) fluorescence. This fluorescence occurs at angles of $\theta \in \langle \theta_c^{es}, \theta_c^{ls} \rangle$ and $\theta \in \langle -\theta_c^{es}, -\theta_c^{ls} \rangle$, where "e" and "l" represent the environment and fluorescent layer, respectively and all other symbols are as previously described. As predicted by the name, this fluorescence is trapped within the substrate. The fourth and final category is that of evanescent wave (EW) fluorescence and occurs at angles of $\theta \in \langle \theta_c^{ls}, 90^0 \rangle$ and $\theta \in \langle -\theta_c^{ls}, 90^0 \rangle$, where "l" represents the fluorescent layer or spot and all other symbols are as previously described. EW fluorescence

is also confined within the substrate but unlike SC fluorescence, it results in an evanescent field in the fluorescent layer/spot deposited on the surface.

In the majority of fluorescence-based sensors, detection occurs either directly above or directly below the fluorescent spot, which corresponds to detection of the AT/WT or ST fluorescence. From Figures 5.1, 5.2 and 5.3, it can be seen that this fluorescence corresponds to only a small fraction of the total emitted fluorescence. This implies that these configurations do not provide efficient fluorescence capture.

The SC fluorescence comprises as much as 66 % of the total emitted fluorescence. This SC fluorescence is also confined to relatively narrow angular ranges, with $\Delta\theta = \theta_c^{ls} - \theta_c^{as} \approx 30^0$ and $\Delta\theta = \theta_c^{ls} - \theta_c^{ws} \approx 10^0$. Therefore, enhancement of the overall fluorescence capture efficiency was focused on the manipulation of this SC fluorescence. Redirection of the SC fluorescence, out of the substrate and onto a detector positioned beneath, should result in a significant enhancement in the quantity of fluorescence recorded.

The following sections detail the design, fabrication and performance of a custom-designed structure employed to redirect the SC fluorescence out of the substrate and onto a detector, thereby increasing the fluorescence capture efficiency.

### 5.2.2 Design of Enhancement Structure

In order to redirect the SC fluorescence, the top surface of a planar substrate was modified to incorporate a frustrated cone [2]. A cross section of the structure is shown in Figure 5.4.

The enhanced structure is based on the principle that SC fluorescence emitted from a fluorescent spot deposited on the top of the frustrated cone is totally internally reflected by the tilted interface (A in Figure 5.4). Careful choice of the angle $\alpha$ ensures this occurs. Using basic geometry, it can be shown that

$$\tan\alpha = \tan\theta - \frac{w}{h} \tag{5.1}$$

where w represents the width of the top of the frustrated cone and h is the height of the frustrated cone.

An added advantage of the total internal reflection of the SC fluorescence by the tilted interface, A, is that the reflected fluorescence impinges on the bottom

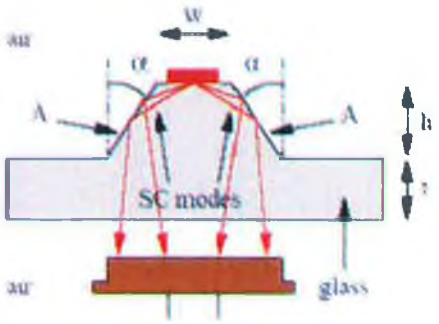


**Figure 5.4:** Cross section of structure employed to improve fluorescence capture efficiency. The frustrated cone facilitates the redirection of the SC fluorescence out of the substrate onto the detector positioned below.

surface at angles close to $0^0$, resulting in the majority of the fluorescence being transmitted out of the substrate onto the detector.

### 5.2.3 Fabrication of Enhancement Structure

Polymers were chosen as the materials for the new enhanced substrate due to the fact that they are a versatile range of materials that can be moulded and machined with relative ease. Surface properties can be modified to suit various applications (e.g. to increase hydrophobicity or to facilitate binding of molecules). Optically transparent polymers are readily available, which was an important factor in the application presented here.

Using a commercially available CAD/CAM software package (XCAD, X-NC, U.K.), a chip design, incorporating six frustrated cones on its surface was produced. Using this design in conjunction with high-precision Computer Numerically Controlled (CNC) micromilling and spark-erosion, a brass mould of the desired chip was fabricated by Parsec (Dublin). Polymethyl methacrylate (PMMA) structured chips were then produced using a Babyplast micro-injection moulder (JET Industrial Services, U.K.). The brass mould employed and the resultant structured polymer chips are shown in Figure 5.5.

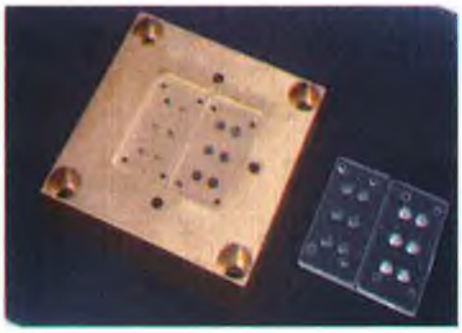

**Figure 5.5:** Brass mould and resulting custom-designed chip containing six frustrated cones.

### 5.2.4 Experimental Method

In order to verify the improved fluorescence capture provided by the structured chips, fluorescent material was deposited onto the frustrated cones and onto a planar substrate and the quantity of fluorescence collected from the two locations was compared.

The ruthenium complex ruthenium(II) tris(4,7-diphenyl-1,10-phenanthroline), $(Ru(dpp)_3{}^{2+})$, was employed as the fluorescence source for all experimental work described in this chapter. This is a commonly employed dye with a large quantum efficiency ($\approx 0.35$) and Stokes' Shift. Its excitation and emission maximum occur at 460 nm and 605 nm respectively, as shown in Figure 5.6.

The large Stokes' Shift associated with this dye complex ensures that interference from excitation light is kept to a minimum. In the work presented here, the ruthenium dye complex was either dissolved in solution or entrapped in a porous sol-gel layer.

The sol-gel process involves the use of metal organic precursors to form glass at low-temperature. The precursors in liquid "sol" phase polymerise to form a gel. Further polymerisation, hydrolysis and heat treatments result in the formation of glass (due to the elimination of water from the system). Addition of the dye complex during the sol phase results in inclusion of the dye molecules within the glass structure. Thus, the sol-gel acts as a matrix for the dye. For the following sections, the term "doped sol-gel" shall be used to refer to sol-gel doped with $Ru(dpp)_3{}^{2+}$.

Using a Genomics Pin-Printer, a spot (approximately 5 $\mu$m thick) of doped

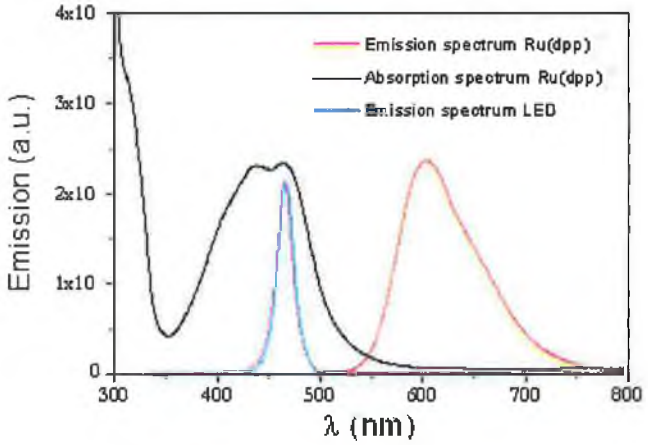


**Figure 5.6:** Graph of absorption and emission spectrum of the ruthenium dye complex ruthenium(II) tris(4,7-diphenyl-1,10-phenanthroline), $(Ru(dpp)_3{}^{2+})$. Also shown is the emission spectrum of the blue LED used to excite the ruthenium dye complex.

sol-gel was printed on the upper surface of each of the frustrated cones of the structured chip and also as discrete spots on the planar portion of the chip (see Section 6.3 for an explanation of the printing process). A blue LED ($\lambda$=460 nm) was used to excite the dye (emission spectra shown in Figure 5.6) and the resultant fluorescence was emitted into the environment and substrate as illustrated in Figure 5.1. Fluorescence transmitted through the chip was collected by a cooled CCD camera, positioned behind the chip.

### 5.2.5 Image Analysis

The 2D images recorded by the CCD camera were analysed using a Mathematica program (based on C) that was written in-house. This program correlated pixel values with fluorescence intensity. The intensity of fluorescence recorded from a defined area was calculated by integrating the pixel values over this area.

In order to determine the level of enhancement provided by the frustrated cones, the quantity of fluorescence emitted from a spot of doped sol-gel printed on the top of such a cone was compared with the quantity of the fluorescence emitted from a spot of doped sol-gel deposited on the planar portion of the chip.

It should be noted that, using a structured chip coated with undoped sol-gel, a background intensity reading of zero was recorded and was used as a background signal to subtract from all other measured values. Therefore, the numerical results presented in the following section were unaffected by background intensity.

### 5.2.6 Results

A typical example of an image of the fluorescence recorded from a printed structured chip is shown in Figure 5.7.

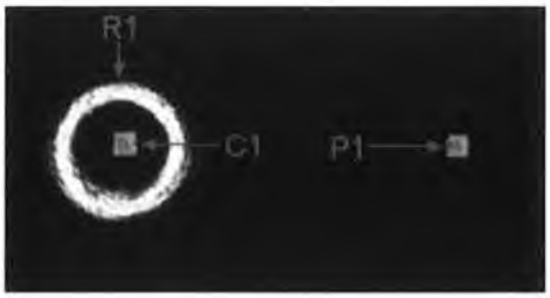


**Figure 5.7:** A representative image of the fluorescence intensity recorded from an enhancement chip. The ring and spot on the left-hand-side of the image corresponds to the fluorescence recorded from doped sol-gel printed on the top of a frustrated cone. The spot on the right-hand-side of the image corresponds to the fluorescence recorded from doped sol-gel printed on the planar portion of the chip.

Two distinct fluorescence profiles are evident. The ring-like profile (together with the central spot) on the left-hand-side of the image corresponds to the fluorescence emitted from the doped sol-gel spot printed on the upper surface of a frustrated cone. The ring (R1) corresponds to the SC fluorescence and the spot in the centre of the ring (C1) corresponds to the ST fluorescence (see Section 5.2.1 for explanation of SC and ST fluorescence). The spot on the right-hand-side of the image (P1) corresponds to the ST fluorescence emitted from the doped sol-gel printed on the planar portion of the chip, i.e., corresponding to the detection configuration employed by a wide range of fluorescence-based scanners.

A circular area, centred on C1 and including R1, was selected and the total intensity in this area was calculated. An identical circular area, centred on P1, was then selected and the total intensity within this area was obtained. The ratio

of these two intensities was then calculated. In the case of Figure 5.7, a ratio, or enhancement factor, of 39 was achieved. Employing the same excitation and detection in each case, 15 printed enhancement chips were excited and analysed. A mean enhancement factor of 35 $\pm$ 5 was achieved, resulting in, on average, 35 times more fluorescence detected from the frustrated cones compared to the planar portion of the chip.

### 5.2.7 Summary

The theoretical analysis discussed in Section 5.1 postulated that the redirection of the SC fluorescence emitted by fluorescent material on a surface should result in enhancement of the fluorescence capture efficiency. In order to verify this, a custom-designed structured chip, employing redirection elements was fabricated and printed with fluorescent material. The printed chip was excited and the resultant fluorescence images analysed. The use of the enhanced configuration resulted in a significant increase in fluorescence capture efficiency when compared with a conventional planar platform, thereby verifying the first prediction of the theoretical analysis.

## 5.3 Discrimination of Surface Versus Bulk Fluorescence

The second prediction of the theoretical analysis discussed in Section 5.1 was that it should be possible to distinguish between fluorescence originating from the surface and the fluorescence originating from the bulk solution comprising the environment. The following sections describe the design and experimental verification of this prediction.

### 5.3.1 Angular Distribution of Fluorescence Contribution from Bulk and Surface

To determine the angular distribution of fluorescence originating at a surface compared to that from a bulk solution, a multilayer system comprised of a sol-gel-coated glass substrate covered by a bulk solution was modelled (schematic

shown in Figure 5.8) [2].


**Figure 5.8:** Schematic of multilayer system, consisting of a glass substrate, sol-gel layer and bulk layer.

The resultant theoretical angular distributions of the fluorescence intensity are shown in Figures 5.9 and 5.10. Figure 5.9 (a) corresponds to the situation where the bulk layer contains fluorescent molecules but the sol-gel layer does not, while Figure 5.9 (b) corresponds to the situation where the sol-gel layer contains fluorescent molecules but the bulk layer does not. Figure 5.10 corresponds to the situation where both the sol-gel and the bulk layers contain fluorescent molecules. In all cases, the refractive index of the bulk layer is $n_b = 1.33$ and its thickness is denoted by $t_b$, while the refractive index and thickness of the sol-gel layer are $n_l = 1.43$ and $t_l = 1.5\,\lambda$, respectively (where $\lambda$ represents the excitation wavelength).

From Figures 5.9 and 5.10, it can be seen that the theoretical analysis predicts that the contribution originating from the sol-gel layer and the bulk layer are observed within different angular regions. In particular, the main contribution originating from the bulk layer is radiated at angles *below* the critical angle $\theta_c^{ws}$ (where $\theta_c^{ws}$ corresponds to the critical angle of the water/glass interface), while the main contribution originating from the thin sol-gel layer is observed at angles *above* the critical angle $\theta_c^{ws}$.

### 5.3.2 Experimental Setup

In order to verify the theoretical predictions summarised in Section 5.1, an experimental analysis of customised samples was carried out. Sol-gel layers were formed on glass slides by dip-coating, a process which involves the immersion and withdrawal of the slides from a sol. The thickness of the layer increases with the rate of removal. As was the case in Section 5.2, the ruthenium dye complex

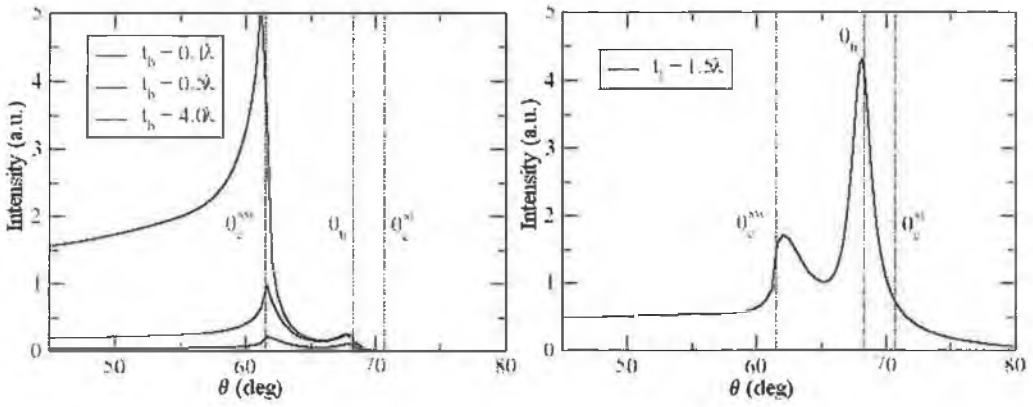


(a) (b)

**Figure 5.9:** Angular distributions of fluorescence intensity emitted from a multilayer system in which a glass substrate is coated with a sol-gel layer and covered by a bulk layer. Graph (a) corresponds to the situation where the bulk layer contains fluorescent molecules but the sol-gel layer does not and graph (b) corresponds to the situation where the sol-gel layer contains fluorescent molecules but the bulk does not.

$Ru(dpp)_3{}^{2+}$ was employed as the fluorescent compound. Fluorescence from the doped sol-gel layer fulfilled the role of surface-originating fluorescence while that originating from the doped solution above the sol-gel layer was considered to be bulk fluorescence.

Using a refractive index matching fluid, a sol-gel-coated slide was attached to a semi-cylindrical prism. Use of the semi-cylindrical prism ensured that the angular distribution of the radiated fluorescence was maintained. A poly(dimethylsiloxane) (PDMS) flowcell (see Section 4.4.2 for more information on PDMS) was sealed against the glass slide and a peristaltic pump was used to flow bulk solutions across the slide. The setup is shown in Figure 5.11.

The bulk solutions employed were ethanol and $Ru(dpp)_3{}^{2+}$-doped ethanol, corresponding to non-fluorescing bulk and fluorescing bulk solutions, respectively. The flowcell, slide and prism were attached to a rotary stage, which facilitated the precise alignment and measurement of the fluorescence emission angles. Fluorescence excitation was achieved via a blue, fibre-coupled LED (emission spectrum shown in Figure 5.6). The position of the fibre tip was adjusted so as to provide a small spot of light (diameter of $\approx 1\,\text{mm}$) in the centre of the sample, which

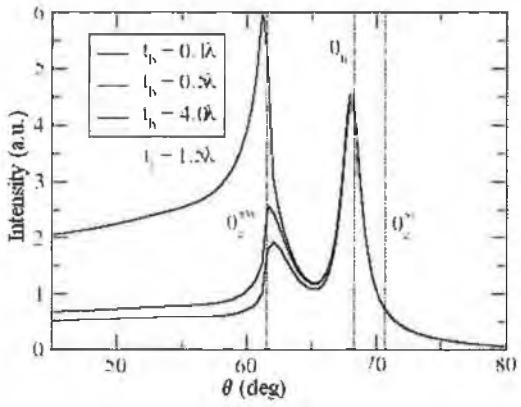


**Figure 5.10:** Angular distribution of fluorescence intensity emitted from a multilayer system in which a glass substrate is coated with a doped sol-gel layer and covered by a fluorescent bulk layer.

coincided with the centre of the semi-cylindrical prism. Fluorescence emitted by the excited ruthenium complex was transmitted through the prism to a detector positioned at the face of the prism.

A linear detector array (LDA) was employed to measure the intensity and angle of the fluorescence emission. The LDA comprised 1024 photodiodes, positioned in a linear format. An in-house, custom-written LabVIEW program controlled the rotary stage, data acquisition and visualisation. By plotting the intensity from each photodiode against its location on the LDA, a 2D map of the fluorescence emission profile was obtained, detailing the intensity emitted at each angle.

### 5.3.3 Experimental Method

Two samples were investigated. The first consisted of a glass slide coated with a doped sol-gel layer and the second consisted of a glass slide coated with an undoped sol-gel layer. Sequences of fluorescing and non-fluorescing bulk solutions were passed over each of these samples and the emitted fluorescence recorded. The sequences are summarised in Table 5.1.

Following acquisition of the fluorescence profiles corresponding to each of the steps described in Table 5.1 (a), the glass slide coated with doped sol-gel was replaced by a glass slide coated with an undoped sol-gel layer. The sequence of

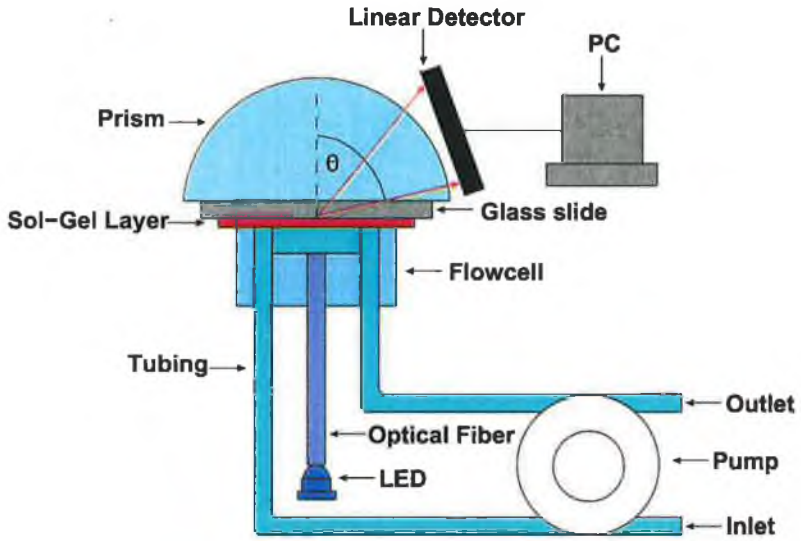


**Figure 5.11:** Experimental setup for distinguishing between surface and bulk fluorescence. Radiated fluorescence originating from the bulk solution and/or the surface of a coated glass slide was transmitted through a prism to a linear detector array, which measured the intensity and angle of emission.

steps described in Table 5.1 (b) was passed over the sample and the corresponding fluorescence emissions recorded. The reason for the exclusion of water from the sequence described in Table 5.1 (b) will be explained in Section 5.3.4.

### 5.3.4 Results

#### Calculation of Critical Angles

The refractive indices of each of the solutions and materials employed are listed in Table 5.2. These values were used to calculate the critical angles of each of the interfaces. The calculated critical angles, which were employed in the analysis of the experimental results, are listed in Table 5.3.

#### Determination of Calibration Functions

The linear detector array (LDA) employed to record the angular profile of the fluorescence emission from each sample consisted of 1024 photodiodes, with the signal from each photodiode representing a pixel on the acquired image. Due to

| Step | Medium Above Doped Sol-Gel Layer |
|---|---|
| 1 | air |
| 2 | water |
| 3 | doped ethanol |
| 4 | water |
| 5 | doped ethanol |
| 6 | undoped ethanol |

(a)

| Step | Medium Above UnDoped Sol-Gel Layer |
|---|---|
| 1 | air |
| 2 | ethanol |
| 3–6 | doped ethanol |
| 7 | undoped ethanol |

(b)

**Table 5.1:** Sequence of steps specifying medium above sol-gel layer. The tables (a) and (b) correspond to the sequence of bulk solutions above the sol-gel layer for the doped and undoped samples respectively.

| Solution/Material | Refractive Index |
|---|---|
| air | $n_a = 1.000$ |
| water | $n_w = 1.332$ |
| ethanol | $n_e = 1.362$ |
| sol-gel | $n_l = 1.425$ |
| glass substrate | $n_s = 1.515$ |

**Table 5.2:** Refractive index values of each of the solutions and materials employed during the experiment.

the fact that the detector was linear and the face of the semi-cylindrical prism was curved, the distance between each photodiode and the prism varied in relation to its position in the LDA. Therefore, it was necessary to determine a relationship between the measured intensity of a particular photodiode and the true intensity at the corresponding angular position. It was also necessary to determine a relationship between the pixel number and the corresponding angular position.

The determination of these relationships was achieved via the use of a sample comprised of a glass slide coated with a relatively thick luminescent layer ($\approx 0.8\,\mu$m) and surrounded by air. This sample was chosen due to the fact that the angular profile of the radiated luminescence contained a distinct peak, which allowed its angular position to be determined precisely. An explanation of the angular profile obtained is provided by the theory referred to in Section 5.1.

| Interface | Critical Angle |
|---|---|
| air/glass substrate | $\theta_c^{as} = 41.30°$ |
| water/glass substrate | $\theta_c^{ws} = 61.55°$ |
| ethanol/glass substrate | $\theta_c^{es} = 64.03°$ |
| sol-gel layer/glass substrate | $\theta_c^{ls} = 70.15°$ |

**Table 5.3:** Critical angles corresponding to various interfaces.

The coated sample was attached to the semi-cylindrical prism and mounted on a rotary stage, as before. An LED coupled to an optical fibre was used to excite the central point of the sample and the resultant angular profile of the fluorescence emission was recorded using the LDA. After the image had been acquired, the sample, prism and light source were rotated by $\Delta\theta = 2°$ and a second image was acquired. This process was repeated 9 times and the corresponding experimental data is shown in Figure 5.12.

In the graph, the $x$ axis corresponds to the pixel number, i.e., the position of each photodiode, and the $y$ axis represents the corresponding intensity detected by that particular photodiode.

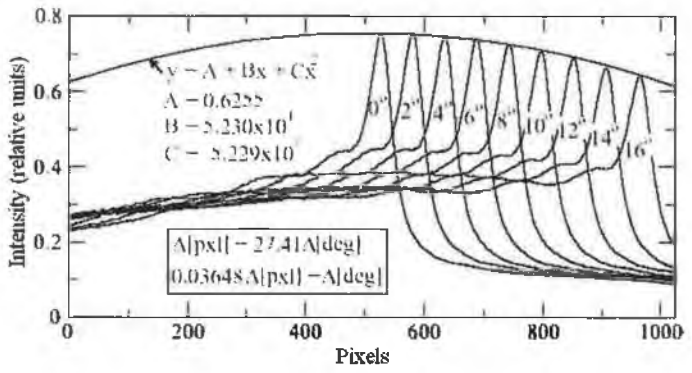


**Figure 5.12:** Angular profile of the fluorescence intensities obtained for 9 different orientations of the semi-cylindrical prism containing the sample. The angles of rotation are shown in the graph. Also shown are the calibration functions of the detection system.

The overall angular profile of the fluorescence emitted remained unchanged as the stage was rotated. However, slight distortion occurred at the edges of the image due to the fact that the photodiodes at the edges of the LDA were

further from the face of the semi-cylindrical prism than those in the centre. This is clearly demonstrated by the decrease in intensity of the peak as its position approached the edge of the image.

The variation of the peak intensity across the image could be described by the following quadratic function:

$$y = A + Bx + Cx^2 \tag{5.2}$$

where $A = 0.6255$, $B = 5.230 \times 10^{-4}$ and $C = -5.229 \times 10^{-7}$, with $y$ representing the detected luminescence intensity and $x$ representing the pixel position.

It was observed that every rotation of the sample by $\Delta\theta = 2°$ corresponded to the same change of the peak position on the image i.e. a linear relationship existed between the variation of the angular position of the peak and the sample rotation. Subsequently, the relationship between the difference in the angular position, represented by $\Delta$ [deg], and the difference in the pixel position, represented by $\Delta$ [pxl], was calculated to be:

$$\Delta\,[\text{pxl}] = 27.41\,\Delta\,[\text{deg}] \tag{5.3}$$

$$\Delta\,[\text{deg}] = 0.03648\,\Delta\,[\text{pxl}] \tag{5.4}$$

Equations 5.3 and 5.2 represent the calibration functions of the LDA-based detection system. Angular fluorescence intensity profiles obtained by the LDA need to be divided by the intensity calibration function 5.2 in order to obtain the true intensity values. Subsequently, the profile is transformed to the angular profile using Equation 5.3.

It should be noted that this procedure does not provide *absolute* values of angles but only the *relative* angular differences. This is due to the experimental apparatus, as the positions of the samples and semi-cylindrical prism are not identical for each experiment. However, once a sample is in place and the absolute value of a particular pixel is determined, this value does not change over the course of the experiment. Therefore, in order to interpret the data obtained, the angular profile of the emitted fluorescence must contain at least one feature with a known angular position.

After the calibration procedure had been completed, testing of different samples could proceed.

### Doped Sol-Gel-Coated Slide

The first sample investigated was a glass slide coated with a doped sol-gel layer. Using the setup described in Section 5.3.2, the sequence of solutions listed in Table 5.1 (a) was passed over the coated slide. The resultant angular profiles of the fluorescence intensity when the layer was surrounded by the first and second solutions, i.e., air and water, are shown in Figure 5.13

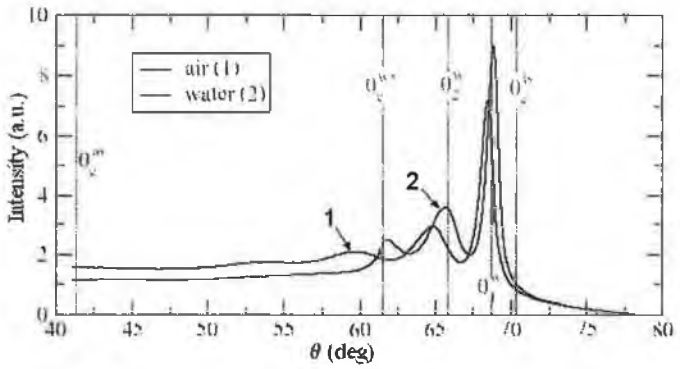


**Figure 5.13:** Angular distributions of the fluorescence intensity radiated by a doped sample surrounded by air (curve 1) and water (curve 2) The curves represent the stabilised profiles and they correspond to the data which was calibrated using Equations 5.3 and 5.2.

Curve 1 in Figure 5.13 corresponds to the angular profile of the fluorescence intensity when the sample was covered by air. After the bulk changed from air to water, the angular profile changed to that shown by curve 2. The profile matches well with the theoretical plots shown in Section 5.3.1. In particular, there is an obvious transition between the almost constant intensity profile below the critical angle $\theta_c^{ws}$ and the profile within the angular range $\theta \in \langle \theta_c^{ws}, \theta_c^{ls} \rangle$, in which distinct peaks are present.

This feature was used to determine the absolute position of the sample. From Table 5.3, it was deduced that this feature was located at $\theta_c^{ws} = 61.55°$ and all other features and their corresponding angular positions were determined relative to this value.

The water bulk solution was then replaced by ethanol doped with $Ru(dpp)_3{}^{2+}$. After a stabilisation time, during which the angular profile of the fluorescence intensity was unpredictable due to the mixing of the two solutions, the profile

shown as curve 3 in Figure 5.14 was obtained.

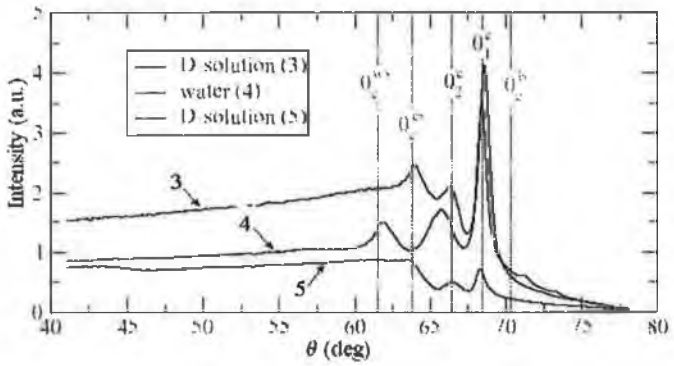


**Figure 5.14:** Angular distributions of the fluorescence intensity radiated by a doped sol-gel-coated glass slide. The curves correspond to the cycle during which the doped layer was surrounded by a doped ethanol solution (curve 3), water (curve 4) and the doped ethanol solution (curve 5), respectively. The curves represent the stabilised profiles and are calibrated using Equations 5.3 and 5.2.

A notable difference between the angular profiles in Figure 5.13 and in Figure 5.14 is the shift in position of the feature characterising the location of the critical angle of the substrate/environment interface. Due to the change of the environment from water to ethanol, this feature moved from the angular position corresponding to $\theta_c^{ws}$ to that corresponding to $\theta_c^{es}$. Applying the calibration function 5.3 to the measured values showed that they were in agreement with the theoretical values listed in Table 5.3. Therefore, it was concluded that changes in refractive index can be observed using this experimental method.

Upon changing the bulk solution from non-fluorescing water to fluorescing ethanol, the intensity of the angular profile below $\theta_c^{es}$ increased substantially relative to the intensity of the profile above this angle. This is in excellent agreement with the theoretical predictions, i.e. that the majority of the fluorescence originating from the bulk solution is observed at angles below the critical angle $\theta_c^{es}$.

During the course of the experiment, an overall decrease in the intensity of the angular profile was observed, as can be seen upon comparison of the plots in Figure 5.13 and 5.14. One possible explanation for this decrease may be that the fluorescent molecules in the bulk solution absorbed a portion of the excitation light (as is required in order to generate the fluorescence). Due to this absorption,

the intensity of the excitation light reaching the sol-gel layer would be reduced. Consequently, the contribution of the sol-gel layer to the fluorescence intensity would be reduced, resulting in a reduction of the intensity of the profile above the critical angle $\theta_c^{es}$, as seen in Figure 5.14.

In the next step of the experiment, the doped-ethanol solution was replaced by water (non-fluorescing). A period of stabilisation, corresponding to the transition to a purely aqueous environment, was again observed. The stabilised angular profile is represented by curve 4 in Fig. 5.14. Comparing this profile to that obtained when the layer was last in such an environment (curve 2 in Fig. 5.13), it can be seen that the angular profile of the fluorescence intensity is essentially unchanged. The most significant discrepancy is an overall decrease in intensity by a factor of approximately 2 across the entire angular range. Variations in the intensity of LED emission were not thought to be sufficient to account for such a change. A possible explanation for the observed decrease in the fluorescence intensity was removal of ruthenium complex molecules from the layer or their quantum yield was somehow reduced during the experiment (possibly via photobleaching).

The following stage of the experiment consisted of again replacing the water with a dye-doped ethanol solution. The corresponding angular profile of the fluorescence intensity (shown by curve 5 in Fig. 5.14) exhibited the same features as the profile corresponding to the previous identical transition discussed above. However, a further decrease in the overall intensity of the angular profile was also observed. This continued decrease supported the proposed process of leaching of the fluorescent molecules from the sol-gel layer

In order to eliminate the unpredictable behaviour of the angular profile during the transition period between water and the doped-ethanol solution, it was decided to instead employ undoped ethanol as the non-fluorescing solution. This eliminated possible issues associated with the refractive index difference between water and ethanol, along with the unpredictable mixing behaviour of the two. This step resulted in a smooth transition between fluorescing and non-fluorescing solutions.

Three additional cycles of fluorescing bulk followed by non-fluorescing bulk were carried out. The resultant angular profiles of the fluorescence intensity corresponding to these three cycles are shown by curves 1–6 in Fig. 5.15.

Comparing the curves in Figure 5.15 (a) and 5.15 (b), a clear difference in

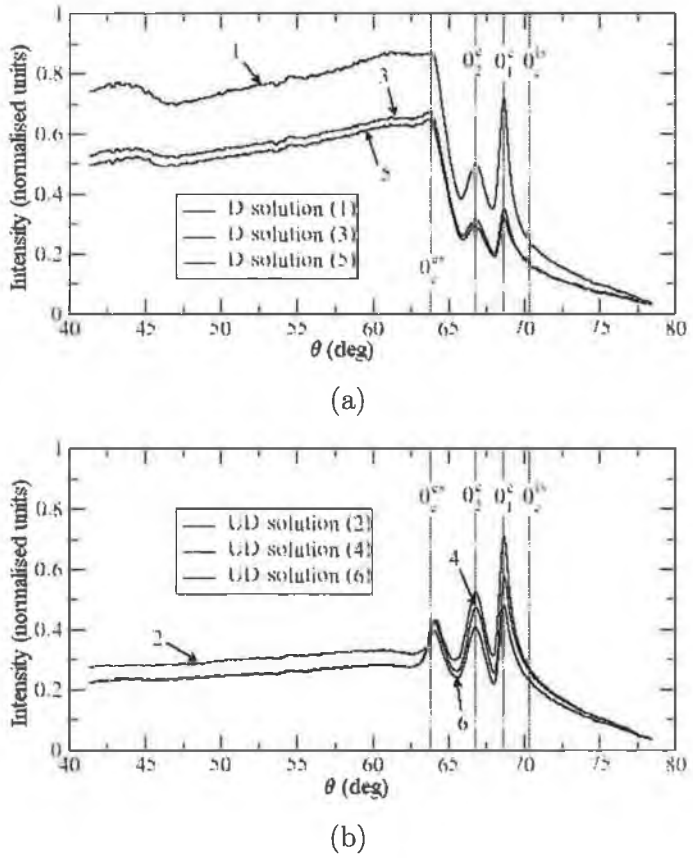


(a)

(b)

**Figure 5.15:** Angular profiles of the fluorescence intensity radiated by the doped sol-gel sample. The curves correspond to the cycle during which the doped layer was surrounded by a doped ethanol solution—curves 1, 3 and 5 in the graph (a)—and by an undoped ethanol solution—curves 2, 4 and 6 in the graph (b). The curves represent the stabilised profiles and are calibrated using Equations 5.3 and 5.2.

the angular profiles is observed below the critical angle $\theta_c^{es}$. When the doped solution is present above the sol-gel layer, a significant increase in intensity is observed below this angle compared to the angular range above it. This is, again, in agreement with theoretical predictions. Therefore, this section of work shows that, in the case of the fluorescing surface (represented by the doped sol-gel layer), it is indeed possible to distinguish between fluorescence contributions from the bulk and the surface. The next stage of this work was to determine if this discrimination is possible in the case of a non-fluorescing surface (represented by an undoped sol-gel layer).

### Undoped Sol-Gel-Coated Slide

Upon completion of the cycles employing a doped sol-gel layer, the sample was replaced by a glass slide coated with a layer of undoped sol-gel. Figure 5.16 shows the angular fluorescence intensity profiles recorded for the sequence of solutions listed in Table 5.1 (b).

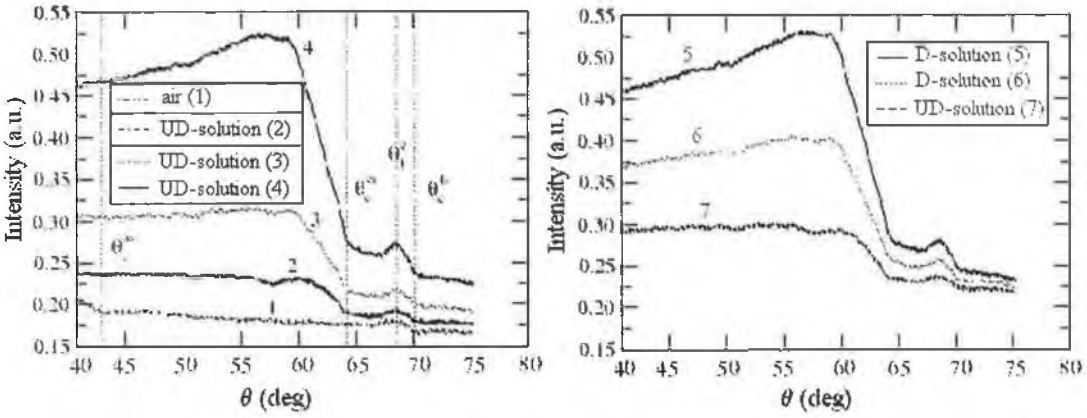


**Figure 5.16:** Angular profiles of fluorescence intensity from a glass slide coated with an undoped sol-gel layer. The numbers associated with the curves correspond to the steps summarised in Table 5.1 (b). The curves were calibrated using Equations 5.3 and 5.2.

Curve 1 in Figure 5.16 corresponds to the angular profile obtained in an air environment. According to the theoretical analysis, as the distance between the radiating dipole and the surface increases, the intensity above the critical angle decreases [1]. In particular, for large distances, there is an abrupt decrease in intensity above the critical angle. This is due to the nature of the coupling of the light into the substrate. As explained in Chapter 3, the electromagnetic field propagating in the glass at angles $\theta \in \langle \theta_c^{es}, 90° \rangle$, extends an exponentially decaying tail (known as the evanescent field) into the surrounding media. The fluorescence detected within this angular range is provided by coupling of the dipole's *near-field* with the evanescent field. Consequently, for large distances of the dipole from the surface, the evanescent field does not reach the dipole's position. This implies that, due to weak coupling of the evanescent field and the dipole's *near-field*, very little fluorescence is detected above the critical angle for

such large distances.

In the setup employed here, the blue excitation light originates at a large distance from the surface (tip of the optical fibre). Therefore, for the reasons explained above, it could not be coupled into the glass, implying that it would not be detected at angles greater than the critical angle $\theta_c^{as}$. Consequently, considering the divergence of the beam emerging from the tip of the fibre, the increase of the intensity below the angle 43°, shown in Curve 1 in Figure 5.16, was attributed to the blue excitation light and this angle was determined to correspond to the critical angle $\theta_c^{as}$.

The second feature present in the angular fluorescence emission profile is a peak that is found around the angle $\theta_1^e$. This was attributed to scattering of the blue excitation light at either the top or bottom interface of the sol-gel layer or within the layer. This scattering would have effectively acted as a source of light within the layer, resulting in a non-zero intensity within the angular range $\theta \in \langle \theta_c^{es}, \theta_c^{ls} \rangle$, as observed.

In the next step of the experiment, the solution above the sample was changed from air to undoped-ethanol. The corresponding angular profile of the fluorescence intensity is illustrated by curve 2 in Figure 5.16. The slight increase of the measured intensity below $\theta_c^{es}$ was again attributed to the blue excitation light and it was this distinctive feature that was used to determine the absolute angular position of the sample.

Following the undoped-ethanol solution, a doped-ethanol solution was introduced above the sample, resulting in a substantial increase in the fluorescence intensity below $\theta_c^{es}$, compared to the fluorescence detected above this angular position. This is demonstrated by curves 3 and 4 in Figure 5.16 (a). Curve 3 corresponds to the transition ethanol→fluorescent solution and curve 4 corresponds to 100 % fluorescent solution. Once attained, this saturated profile remained constant.

When undoped ethanol was re-introduced above the layer, the fluorescence intensity decreased back to the level it had been at previous to the introduction of the fluorescent solution. This is demonstrated by curves 6 and 7 in Figure 5.16 (b). Similar to curve 3 in graph (a), curve 6 corresponds to the transition fluorescent solution→ethanol.

There is a clear distinction between the angular profiles of the fluorescence

intensity when the bulk solution was non-fluorescent (curves 2 and 7) and when the bulk solution was fluorescent (curves 4 and 5). Replacing the non-fluorescing bulk with a fluorescing bulk resulted in a substantial increase in intensity below the critical angle $\theta_c^{as}$, compared to the effect on the profile above this angle. Thus, this work successfully demonstrated the prediction of the theoretical analysis (see Section 5.1) that it is possible to distinguish between the fluorescence contribution from the bulk and from the surface.

### 5.3.5 Summary

The theoretical analysis discussed in Section 5.1 predicted that it should be possible to distinguish between surface- and bulk-originating fluorescence. In order to experimentally verify this prediction, doped and undoped sol-gel-coated glass slides were fabricated and, using the setup described in Section 5.3.2, doped and undoped bulk solutions were passed above the samples. The resultant angular profiles of the radiated fluorescence intensities were analysed. Examination of particular angular ranges of the radiated fluorescence intensity showed that it is possible to discriminate between surface and bulk fluorescence. In particular, it was shown that changing the bulk solution from non-fluorescing to fluorescing resulted in a substantial increase in the emitted fluorescence below the critical angle $\theta_c^{es}$ but resulted in only a negligible effect above this angle. This was in agreement with theoretical predictions.

## 5.4 Surface Versus Bulk Fluorescence Discrimination Using Enhancement Structure

The custom-designed, structured chip described in Section 5.2 is based on the redirection of SC fluorescence out of the chip and onto a detector placed below. As fluorescence originating from the bulk solution is emitted at a different range of angles to the SC fluorescence (see Section 5.3.2), surface versus bulk fluorescence discrimination should be inherent in the design of the structures. The following sections detail the experimental work undertaken in order to determine the validity of this.

### 5.4.1 Excitation and Detection Systems

Structured chips, each incorporating six frustrated cones, were fabricated as described in Section 5.2.3. Non-fluorescing and fluorescing surfaces were defined by doped and undoped sol-gel layers, respectively, printed onto the top of the frustrated cones. As the frustrated cones were designed for optimum operation in water, the non-fluorescing and fluorescing bulks were defined by water and doped-water passed above the chip surface. The XCAD design used to generate the chips was updated to include a dual-channel flowcell, which, when sealed against the chip surface, enclosed three frustrated cones in each channel. Therefore, using micro-injection moulding, it was possible to simultaneously produce chips and flowcells.

Excitation of the ruthenium dye complex was achieved via a blue LED (emission spectrum shown in Figure 5.6). A schematic of the excitation and detection set-up is shown in Figure 5.17.

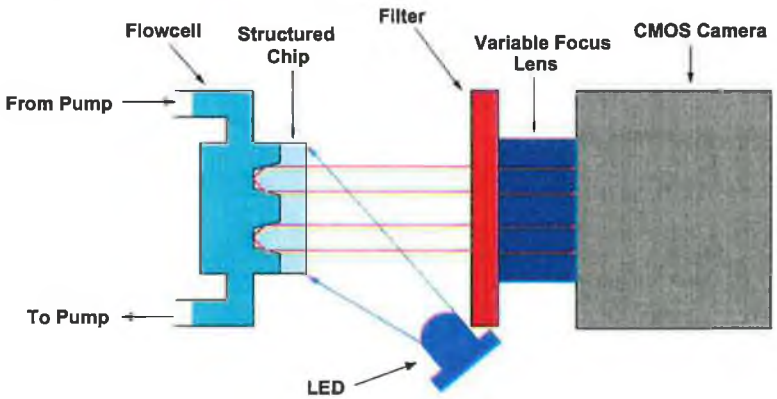


**Figure 5.17:** A schematic of the excitation and detection system employed to determine if the capability to discriminate between surface and bulk fluorescence is inherent in the enhanced fluorescence capture structure design.

The chip and flowcell were positioned in front of a CMOS camera, bandpass filter (centred on 610 nm with FWHM of 10 nm) and variable focal length lens, with the flowcell and lens located on opposite sides of the chip. Excitation of the chip occurred from behind, as it was found that some of the excitation light was absorbed if passed through the flowcell.

### 5.4.2 Experimental Method

Three of the frustrated cones were printed with undoped sol-gel. Doped sol-gel was printed on the top of the other three cones. Three undoped and three doped sol-gel spots were also printed on the planar portion of the chip. Following printing of the sol-gel layers onto the top of cones, a flowcell was sealed to the chip using pressure-sensitive adhesive (optically clear laminating adhesive 8141 from 3M, PLC, United Kingdom). The printed chip and flowcell were then positioned in front of the detector (as described in Section 5.4.1) and a peristaltic pump was connected to the flowcell.

The nonfluorescing and fluorescing bulk solutions (doped and undoped water) were passed over the surface of the chip using the peristaltic pump. The fluorescence emitted from each of the combinations listed in Table 5.4 was recorded.

| Combination | Surface Layer | Bulk Solution |
|---|---|---|
| 1 | Fluorescing | Fluorescing |
| 2 | Fluorescing | Non-fluorescing |
| 3 | Non-fluorescing | Fluorescing |
| 4 | Non-fluorescing | Non-fluorescing |

**Table 5.4:** Bulk solution/surface layer combinations investigated.

### 5.4.3 Image Analysis

The image analysis employed in this work was similar to that described in Section 5.2.5, with the same custom-written C-based Mathematica program being employed. Fluorescence intensity values were recorded for both the frustrated cones and the spots printed on the planar surface of the chips. Background intensities were subtracted from these figures to give true intensity values.

### 5.4.4 Results

Each of the combinations of bulk solution and surface layer listed in Table 5.4 were investigated. As expected, as undoped solution was passed over the frustrated cones printed with undoped sol-gel, no fluorescence was detected. Fluorescence was detected for each of the other bulk solution/surface layer combinations.

Several chips printed with doped sol-gel were investigated. Figure 5.18 shows representative images of the fluorescence profiles obtained. Similar to the images discussed in Section 5.2.6, the spot and ring profile seen on the left-hand-side of both images corresponds to the fluorescence recorded from the frustrated cones. As explained in Section 5.2.6, the ring profile results from the redirection of the substrate-confined fluorescence by the frustrated cones. The spot seen on the right-hand-side of the images corresponds to the fluorescence recorded from the doped sol-gel printed on the planar portion of the chip. Image (a) was obtained when the chip was covered with a non-fluorescing solution and image (b) was obtained when the chip was covered with a fluorescing solution.

(a) (b)

**Figure 5.18:** The spot and ring profile seen on the left-hand-side of both images corresponds to the fluorescence recorded from doped sol-gel printed on the top of the frustrated cone. The spot seen on the right-hand-side of both images corresponds to the fluorescence recorded from doped sol-gel printed on the planar portion of the chip. Image (a) was obtained when the chip was covered by a non-fluorescing bulk solution and image (b) was obtained when the chip was covered by a fluorescing bulk solution.

Table 5.5 shows the intensity values obtained for the spot and ring profiles for both the fluorescing bulk solution and the non-fluorescing bulk solution. It was found that when a non-fluorescing bulk solution was replaced by a fluorescing solution, the intensity of the spots printed on the planar portion of the chip and on the top of the frustrated cones increased. However, this increase in intensity was not observed in the rings. For each chip investigated, changes in the bulk solution had only a negligible effect on the fluorescence intensity of the rings. Calculation of the mean intensities of the spots and rings when covered by fluorescing and non-fluorescing solutions showed that a 85 % increase in spot intensity was

| | Total Intensity [arb. units] | | | | Intensity Increase [%] | |
|---|---|---|---|---|---|---|
| Chip | Spot (NFB) | Spot (FB) | Ring (NFB) | Ring (FB) | Spot | Ring |
| 1 | 17566 | 30365 | 643505 | 692198 | 73 | 7 |
| 2 | 18362 | 34936 | 632219 | 689930 | 90 | 8 |
| 3 | 17406 | 31887 | 630031 | 721371 | 83 | 13 |
| 4 | 19963 | 35558 | 620261 | 670285 | 78 | 7 |
| 5 | 18541 | 34775 | 577218 | 640711 | 88 | 10 |
| 6 | 17926 | 34105 | 589859 | 671479 | 90 | 12 |
| 7 | 18580 | 36476 | 600271 | 648389 | 96 | 7 |
| 8 | 18009 | 32114 | 576615 | 666348 | 78 | 13 |
| 9 | 18634 | 33857 | 630542 | 681686 | 82 | 8 |
| 10 | 17167 | 30843 | 639676 | 687578 | 80 | 7 |
| 11 | 19856 | 37445 | 665685 | 708036 | 89 | 6 |
| 12 | 18225 | 35115 | 612932 | 678462 | 93 | 10 |
| 13 | 17786 | 33364 | 640637 | 665131 | 88 | 4 |
| 14 | 18533 | 34286 | 570930 | 644427 | 85 | 11 |
| 15 | 19887 | 35566 | 602261 | 687698 | 79 | 12 |
| mean | 18429 | 34046 | 615509 | 676915 | 85 | 9 |

**Table 5.5:** Fluorescence intensities and percentage increases of ring and spot profiles, obtained when the chips were surrounded by either a fluorescing bulk solution (FB) or a non-fluorescing bulk solution (NFB).

accompanied by an increase in ring intensity of $< 10\,\%$.

This latter figure indicates a much reduced sensitivity to fluorescence originating from the bulk solution. This in turn suggests that a significant proportion of the fluorescence present in the ring is SC in nature. However, the fact that changes in intensity *were* detected demonstrates that the frustrated cone structure does not facilitate complete discrimination between surface and bulk fluorescence.

## 5.5 Summary

In order to determine the feasibility of discriminating between surface and bulk fluorescence using the frustrated cone structures, chips containing six of these

structures were fabricated and printed with both doped and undoped sol-gel. Spots were printed on top of the frustrated cones and on the planar portion of the chips. Polymer flowcells were used to pass fluorescing and non-fluorescing bulk solutions over the chips. The chips were then excited from behind and the resultant fluorescence was recorded.

It was found that replacing a non-fluorescing bulk solution with a fluorescing bulk solution resulted in a 85 % increase in intensity of the spots printed on the planar portion of the chip but produced an increase in ring intensity of $< 10\,\%$. This result demonstrated that the frustrated cone structures provide an increased insensitivity to bulk fluorescence. However, the small increase in ring intensity showed that they did not provide complete discrimination between the fluorescence originating from the surface and that originating from the bulk.

## 5.6 Conclusions

A theoretical analysis carried out previously described the angular distribution of fluorescence emitted by a radiating dipole at a surface. This chapter detailed the experimental work undertaken to verify two predictions made by the analysis, namely;

1. Redirection of surface-confined fluorescence results in the enhancement of the fluorescence capture efficiency.

2. It is possible to discriminate between fluorescence originating at the surface and fluorescence originating from the bulk above the surface.

Based on the theoretical analysis, polymer chips bearing arrays of frustrated cones were designed and fabricated. These structures redirected the substrate-confined (SC) fluorescence out of the chip and directly onto a detector positioned below. Sol-gel spots doped with a ruthenium dye complex were printed on the top of the cones and on the planar portion of the chips. The spots were then excited and the resultant fluorescence analysed. It was shown that, using the set-up described in Section 5.2.4, up to 40 times more fluorescence was recorded from the frustrated cones than from the planar portion of the chip. This provided

strong experimental verification to the first prediction that redirection of the SC fluorescence results in the enhancement of the fluorescence capture efficiency.

In order to verify the second prediction, a set-up that facilitated the analysis of specific angular ranges was designed and assembled. Employing a sol-gel layer as the surface, various combinations of fluorescing and non-fluorescing layers and bulk solutions were analysed. The angular ranges that corresponded to the surface and bulk solution were identified. It was demonstrated that fluorescence from the bulk and surface were emitted in different angular ranges. Specifically, the majority of the fluorescence originating from the bulk was emitted at angles below the critical angle of the environment/substrate interface.

After providing experimental verification to both predictions, an experiment was carried out to verify the inherent ability of the frustrated cones to discriminate between surface and bulk fluorescence. Sol-gel doped with a ruthenium dye complex was printed on the top of the enhancement structures and on a planar portion of the chips. It was found that substituting a non-fluorescing bulk solution with a fluorescing bulk solution resulted in a large increase in the fluorescence intensity of the spots on the planar portion of the chip but resulted in only a small increase in the intensity of the rings produced by the cones. This demonstrated that the cones provided partial discrimination between surface and bulk fluorescence. However, the fact that there was an increase in intensity implied that the cones are unable to provide complete discrimination between surface and bulk fluorescence. Further optimisation of the structure design would be required in order to achieve complete discrimination.

It was shown in this chapter that the frustrated cones provide increased fluorescence capture compared to conventional planar substrates. Therefore, by incorporating these structures into the chip design, as described in Section 5.2.2, substantially lower limits of detection should be attainable. Accordingly, the next stage of this work involved the replacement of the planar substrate of the immunosensor described in Chapter 4 with the structured chip described in Section 5.2.2.

# Bibliography

[1] L. Polerecky, J. Hamrle, and B. D. MacCraith, "Theory of the radiation of dipoles placed within a multilayer system," *Applied Optics*, vol. 39, no. 22, pp. 3968–3977, 2000.

[2] L. Polerecky, *Optimisation of multimode waveguide platforms for optical chemical sensors and biosensors.* PhD thesis, Dublin City University, 2002.

# Chapter 6

# Development of Enhanced Immunosensor

## 6.1 Introduction

The structured chip described in Chapter 5 was shown to provide enhanced fluorescence capture efficiency compared to planar chips. Therefore, it was decided to replace the glass planar substrate employed in the work described in Chapter 4 with the optimised structured polymer chip. New immobilisation strategies, printing methods and experimental systems were required in order to effectively carry out the replacement. This chapter describes these new systems and presents the results from assays carried out using the new optimised chip.

## 6.2 Antibody Immobilisation

A glass microscope slide was employed as the substrate in the immunosensor described in Chapter 4. One of the major advantages of using glass is its established surface modification procedures [1]. The development of routine, simple polymer surface modification techniques is still in its infancy, with no standard immobilisation strategy for antibodies on polymer surfaces yet established. Therefore, in order to select a strategy for the immunosensor presented here, it was necessary to investigate several different polymer modification methods.

It was decided to immobilise anti-BSA antibodies via the carboxyl groups

present at their C termini (see Section 2.2 for more information). This would leave the antigen-binding sites available and increase the chances of the antibodies being orientated in an upright position. Correct orientation of antibodies on solid substrates is important due to its effect on surface coverage and availability of binding sites. Carboxyl groups readily bind with amine groups (as shown in Section 2.2). Therefore, polymer modifications ultimately resulting in amine groups were required.

The optimised chips described in Chapter 4 were fabricated using polymethyl methacrylate (PMMA). This polymer consists of a carbon chain backbone with methyl ester side chains, as illustrated in Figure 6.1.

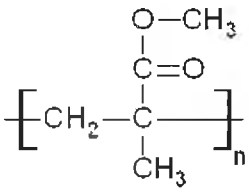

**Figure 6.1:** Illustration of structure of polymethyl methacrylate (PMMA).

As shown in Figure 6.2, there were two possible routes to modify the PMMA surface to produce amine groups on the surface:

1. Convert the methyl ester side chains of the PMMA to useful surface functional groups.

2. Apply a generic surface modification method that is independent of the polymer employed.

Five separate polymer modification strategies were investigated. The first two were specific to the PMMA substrate, while the last three were independent of the chemical nature of the substrate. The specific chemical functionalisations of the PMMA involved a transamidation reaction and a reduction of the surface methyl ester groups. The generic surface modifications involved two radical graft polymerisation processes, the first initiated by oxygen plasma treatment and the second initiated by UV-curing, and a sol-gel coating of hybrid organic-inorganic

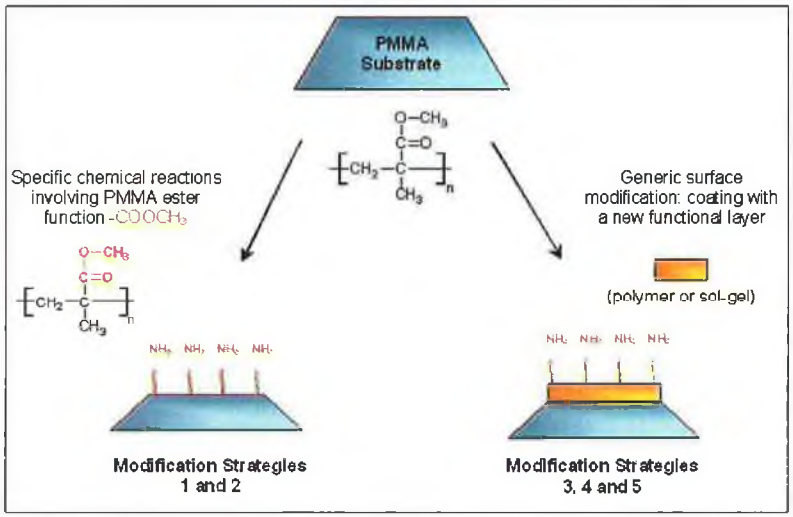


**Figure 6.2:** The two functionalisation routes (specific and generic) of the polymer substrate.

layers on the polymer surface. Each of the 5 different modifications yielded amine-terminated surfaces.

Commercial PMMA sheets were obtained from Goodfellow. The PMMA sheets were machined to a given size to give PMMA slides (35 mm x 10 mm x 1.0 mm) and rinsed with isopropanol, followed by drying with a nitrogen stream. This procedure was followed prior to any of the following chemical treatments on the surface of the PMMA slides.

### 6.2.1 Polymer Modification and Characterisation

#### 1. Amino-Modification

The first polymer modification strategy investigated was that of amino-modification. This involved a transamidation reaction, which is a reaction resulting in the formation of an amide group (structure shown in Figure 6.3).

The first step in the modification exploited the intrinsic reactivity of lithium by reacting 1,3-diaminopropane with n-butyllithium to form N-lithioaminopropane (see Figure 6.4) [2].

Soper et al. reported that the monoanion of N-lithiodiaminopropane (shown in Figure 6.4 as $NH^{-}Li^{+}$) reacts with the surface methyl esters of PMMA to yield

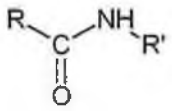


**Figure 6.3:** Structure of amide group. R and R' correspond to hydrogens or alkyl groups.


**Figure 6.4:** Reaction of 1,3 diaminopropane with n-butyllithium to form N-lithiodiaminopropane.

amine-terminated PMMA [3]. Therefore, PMMA slides were immersed in a solution of N-lithiodiaminopropane for less than 3 minutes, after which the reaction was quenched with isopropanol, followed by de-ionised water. The reaction that occurred is illustrated in Figure 6.5.

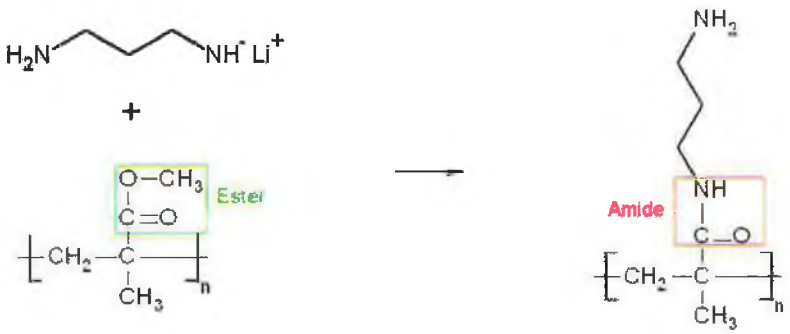


**Figure 6.5:** Illustration of amino-modification of PMMA, using N-lithiodiaminopropane, to form PMMA-$NH_2$.

The amino-modified PMMA slides were then rinsed with copious amounts of isopropanol, followed by de-ionised water and dried under a stream of nitrogen.

### Characterisation of Amino-Modified PMMA

Characterisation of the amino-modificed PMMA slides was achieved using the Perkin Elmer UV/VIS/NIR Lamda 900 Spectrometer. Attenuated total reflectance (ATR) infrared spectra of the slides were obtained both before and after the amino-modification [4]. IR absorption is based on the principle that atoms in molecules vibrate at specific frequencies, which are dependent on the bond type and method of vibration e.g. stretching or bending. Thus, measuring the absorption over a range of frequencies, allows the bonds present in the interrogated sample to be identified. The spectra of the unmodified PMMA and the PMMA-$NH_2$ slides after various reaction times are shown in Figure 6.6.

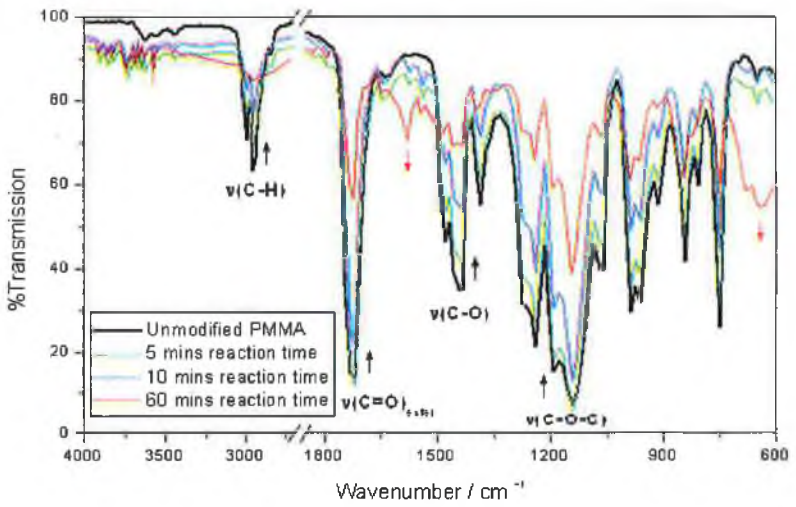


**Figure 6.6:** FT-IR spectra of surface of unmodified PMMA and $NH_2$-modified PMMA.

The unmodified PMMA spectrum correlates well with the transmission spectrum of PMMA documented in the literature [3–5]. The most prominent band is the carbonyl stretch, $\upsilon$(C=O), at $\sim 1730\,\mathrm{cm}^{-1}$. The band maximum is characteristic of methyl esters, particularly those found in PMMA films. The remaining vibrational bands observed are characteristic of the alkane and ester moieties present in the polymer.

With increase of reaction time, a substantial decrease in the intensity of all the ester function bands ($\upsilon$(C=O), $\upsilon$(C-O) and $\upsilon$(C-O-C)) was observed, proving

that a reaction involving this group had occurred. The $NH_2$-modified PMMA spectra display two new peaks at approximately 1540 $cm^{-1}$ and 670-635 $cm^{-1}$ which could be assigned to the amide II stretch ($\delta$(N-H)) and amide IV, V and VI bands respectively. These data are in agreement with the replacement of the ester functionalities by an amide linkage, as described in Figure 6.5.

In order to quantify the number of amines presence on the surface of the PMMA-$NH_2$ slides a ninhydrin test was employed. Fang and Liu described a comprehensive study on the use of ninhydrin for the determination of amines, and their procedure was followed [6]. Firstly, the amide bonds of the amine-terminated PMMA were hydrolysed using HCL, which resulted in PMMA with acid residues and diamine in the reaction solution. The solution was then neutralised and tested with ninhydrin, which reacts with the amines to produce a coloured product. The number of amine molecules present was then determined by comparison with a standard curve (shown in Figure 6.7), which was obtained by measuring the absorbance of varying concentrations of 1,3-diaminopropane at 570 nm.

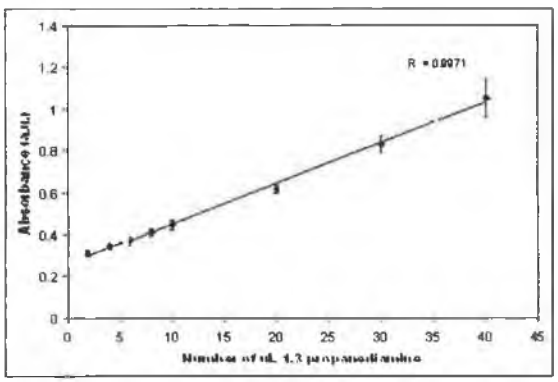


**Figure 6.7:** Standard curve obtained with varying concentrations of 1,3-diaminopropane employing ninhydrin test.

The test proved positive, and the number of amines per $cm^2$ was calculated to be approximately 7 nmol per $cm^2$. This value is slightly higher than that previously reported [3].

In order to confirm whether even surface coverage of amines on the PMMA was obtained, the PMMA-$NH_2$ slides were immersed in a solution containing Cy5 dye, which resulted in the fluorescent labelling of the surface amines. After removal, washing and drying, the slides were examined using using a Genetic

Microsystems (GMS) 418 fluorescence scanner. The scanner excited the Cy5 dye bound to the surface amines using a 635nm laser and the emitted fluorescence was recorded using a microscope and photomultiplier tube. The results were displayed as a 2D false colour image. Analysis of the fluorescence intensity recorded from the PMMA-$NH_2$-Cy5 slides showed that the amino-modification resulted in a reasonably homogenous surface coverage. A representative image is shown in Figure 6.8. The colour scale ranges from black through blue, green, yellow and red to white, where white corresponds to a saturated signal.

**Figure 6.8:** Fluorescence intensity image from PMMA-NH-Cy5 (only bottom portion of slide modified), recorded using a Genetics Microsystems 418 Scanner.

### 2. Hydroxyl-Modification

Hydroxyl-modification was the second strategy examined. Methyl ester side chains of the PMMA were reduced to alcohols using diisobutylaluminium hydride (DIBAL), as illustrated in Figure 6.9.

The machined and cleaned PMMA slides were immersed in a solution of DIBAL in hexane under nitrogen and stirred at room temperature. After the reaction had been completed, the slides were then soaked in isopropanol, followed by extensive rinsing with de-ionised water and were finally dried under a stream of nitrogen.

The next step of the modification technique was the formation of amines on the PMMA surface. Since alcohols are not very reactive towards amines in aqueous solution they were converted to cyano-esters, (which are more reactive

**Figure 6.9:** Schematic of ester reduction to alcohols, using diisobutylaluminium hydride.

to amines) before further modification was possible. Cyanogen bromide, dissolved in acetonitrile, was added to a solution of sodium carbonate containing hydroxyl-modified PMMA slides. The cyanogen bromide was used to react with the alcohols present at the PMMA surface to form highly reactive cyano-ester groups. The slides were then immersed in a solution of 1, 3-diaminopropane in 0.2M carbonate buffer solution (pH9.0), and stored at 4°C overnight. During this time, the cyano-ester groups reacted with the amines present the in solution to form amine groups on the surface, as illustrated in Figure 6.10.

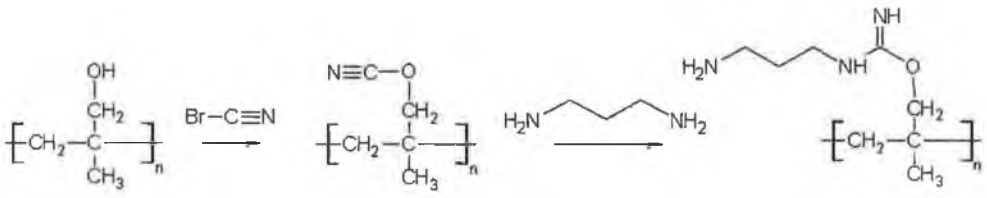

**Figure 6.10:** Schematic of cyano-ester formation and resultant amine-terminated surface.

### Characterisation of Hydroxyl-Modified PMMA

ATR infrared spectra of the PMMA slides were obtained before and after the hydroxyl-modification. The spectra of the unmodified PMMA slides and the modified PMMA-OH slides are shown in Figure 6.11.

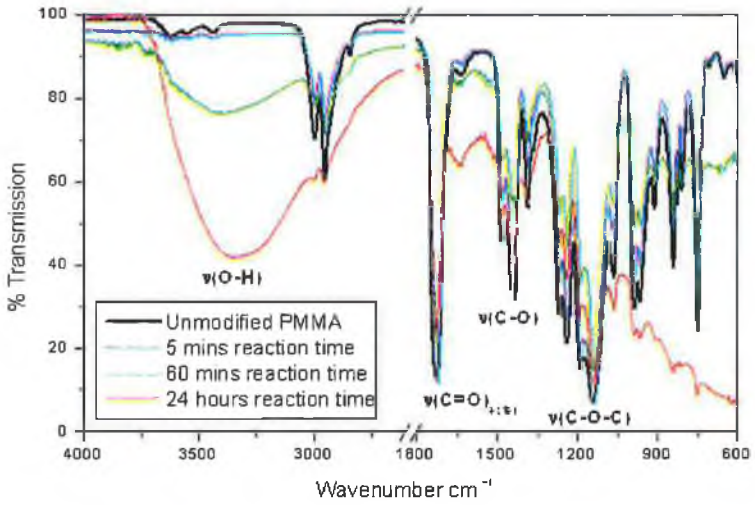


**Figure 6.11:** FT-IR spectra of surface of unmodified PMMA and OH-modified PMMA.

As was observed with the spectra of amino-modified PMMA slides, the hyroxyl-modified PMMA slides show a decrease in intensity of the ester bands ($\upsilon$(C=O), $\upsilon$(C-O) and $\upsilon$(C-O-C)). The emergence of a new large band centered at 3320 $cm^{-1}$, corresponding to OH stretching frequencies of the alcohol from the reduced ester, was also observed [4]. These data confirm the chemical reaction depicted in Figure 6.10. The evolution of the spectra shows that leaving the PMMA slide in DIBAL (hexane) for one hour was adequate time for the reaction to occur.

The surface coverage of the hydroxyl groups was measured using an aniline blue stain, which attached only to hydroxyl groups and was subsequently analysed using optical microscopy. Examination of the slides showed relatively uneven surface coverage of hydroxyls. Unmodified PMMA exposed to the same conditions showed only trace background difference to "blank" PMMA. The results are shown in Figures 6.12 .

Following the modification of the PMMA-OH slides to PMMA-OH-$NH_2$, the amine surface coverage was examined. In order to facilitate comparisons between modification strategies, the method employed to examine the surface coverage in Section 6.2.1 was also employed here. Cy5 dye was bound to the amines on the modified surface and analysed using the fluorescence scanner. A representative fluorescence intensity image is shown in Figure 6.13, illustrating the relatively

(a) (b)

**Figure 6.12:** (a) Surface of unmodified PMMA after staining with aniline blue, (b) Surface of PMMA-OH after staining with aniline blue.

uneven surface coverage, supporting the aniline blue stain test results. Both the amino-modified PMMA slides and the hydroxyl-modified slides resulted in similar values of fluorescence intensity but the hydroxyl-modification produced less homogenous amine coverage.

**Figure 6.13:** Fluorescence intensity image from PMMA-OH-$NH_2$-Cy5 (only bottom portion of slide modified), recorded using a Genetics Microsystems 418 fluorescence scanner.

### 3. Carboxyl-Modification via Oxygen Plasma

The third and fourth modification strategies were based on graft polymerisation, whereby polymers with useful functional groups were grafted onto the PMMA substrate. The polymers were formed from vinyl monomers, which are molecules containing carbon-carbon double bonds. In order to start the polymerisation

process, an initiator was required to break the double bonds of the monomers. These bonds were then used to link the monomers into chains, via chain propagation [7]. In both strategies presented here, free radicals were employed to initiate the polymerisation process. In the first strategy, radicals were generated on the PMMA surface via an oxygen plasma.

Plasmas are ionised gases, which can be generated by applying high temperatures or strong electric or magnetic fields to a gas [8]. In this work, unmodified PMMA slides were inserted into a plasma chamber and an oxygen plasma was generated using an electric field. When placed in a plasma, the polymer surface is exposed to a broad spectrum of ions, electrons, neutral molecules, radicals, and electromagnetic radiation, each of which modify the first few nanometers of the polymer surface. These different species strongly interact with the polymer, resulting in chemical and physical modifications of the surface.

It is not possible to give a precise mechanism of the chemical modification involved in the plasma treatment. This is due to the great reactivity of the compounds involved and the multiplicity of oxidation mechanisms that can be proposed for PMMA. Very few descriptions have been provided in the literature, as the numerous highly-reactive species involved in the surface modifications are not well defined. An example of some of the possible reactions, proposed by Chai et al., are shown in Figure 6.14 [9].

As a result of the plasma treatment, free radicals were formed on the PMMA surface. Upon printing of the monomer, methacrylic acid, onto the surface, these radicals initiated the graft polymerisation, coupling with the active methacrylic acid species to form the co-polymer, as illustrated in Figure 6.15.

The carboxyl-modified PMMA was further treated with N-(3-Dimethylaminopropyl)-N-ethylcarbodiimide hydrochloride (EDC), which acted as a catalyst in the binding of the acid and amine groups, and upon addition of 1,3-diaminopropane, amines were formed on the surface of the PMMA (as shown in Figure 6.16).

### Characterisation of Carboxyl-Modified (via Oxygen Plasma) PMMA

Toluidine blue dye, which contains a free amine group, was used to indicate the presence of carboxyl groups on the PMMA slides [10]. A solution of toluidine blue stain was prepared by dissolving 0.025g toluidine blue in 100mls 0.01 N HCl,

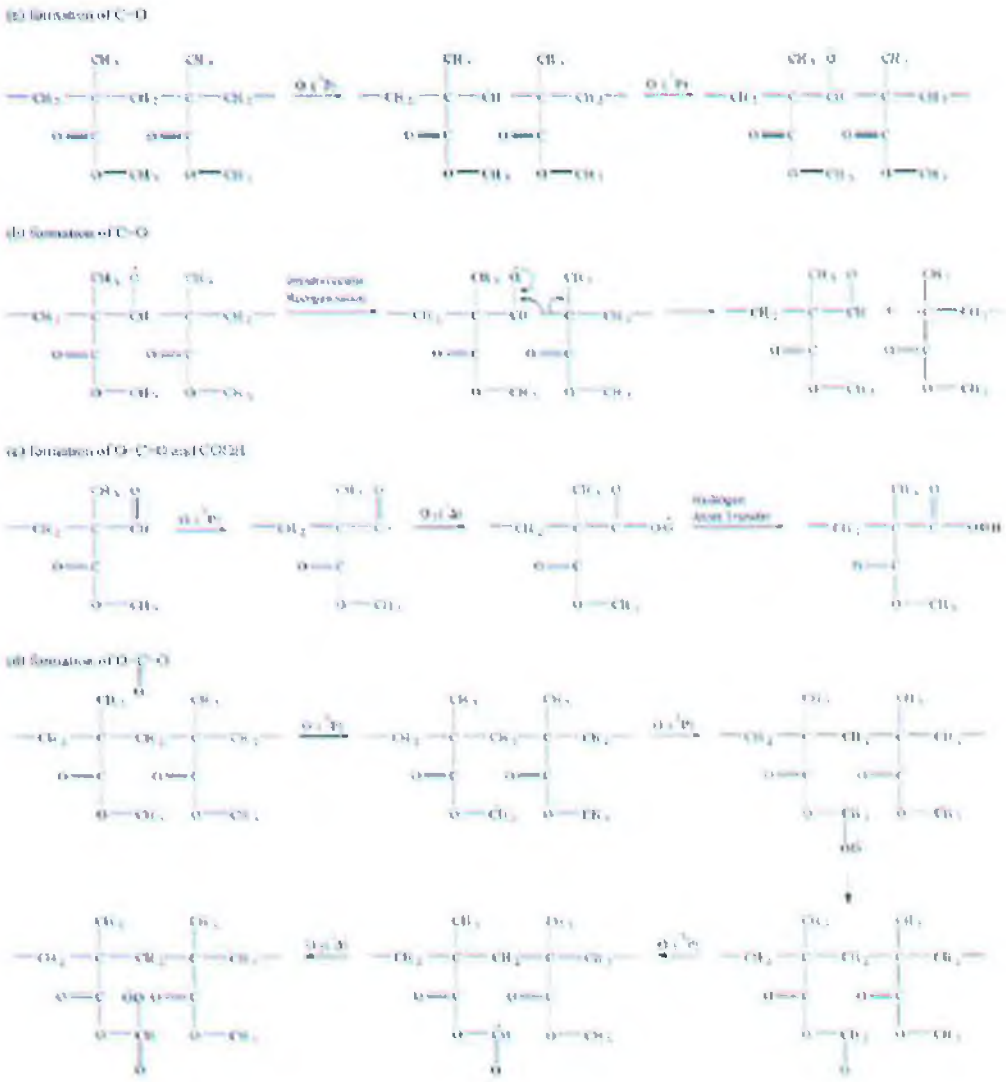

**Figure 6.14:** Examples of possible oxidation schemes for oxygen plasma-treated PMMA.

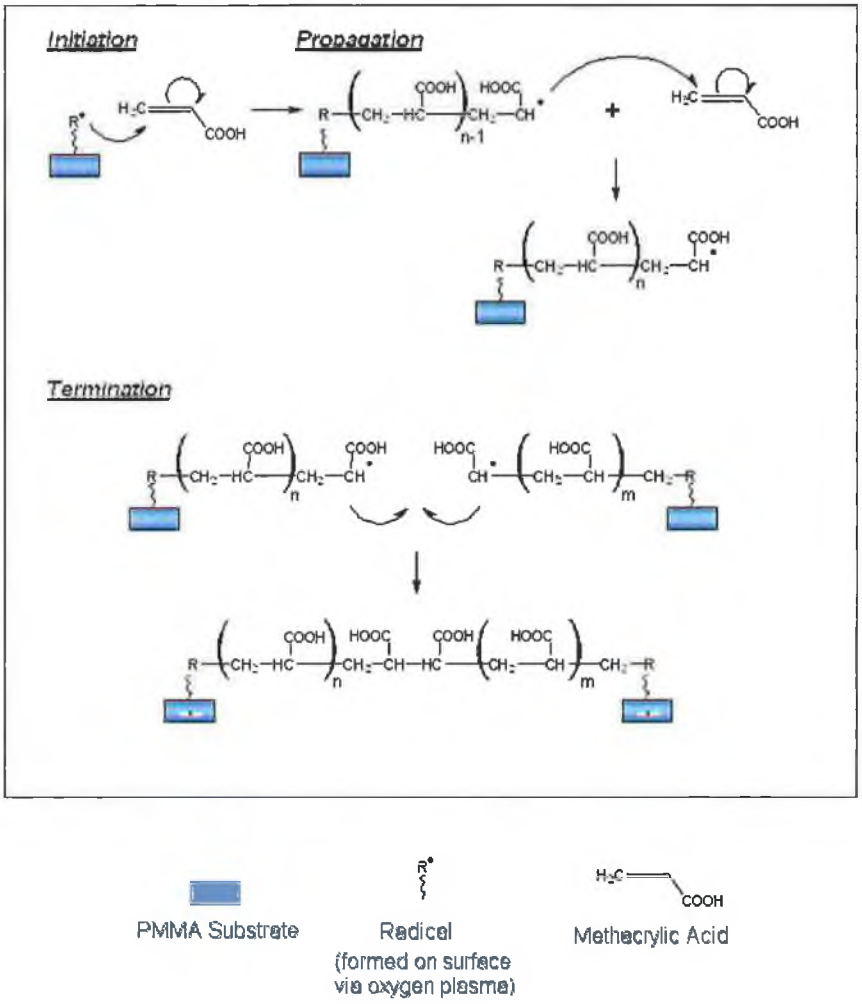


**Figure 6.15:** Reaction of oxygen plasma-treated PMMA with methacrylic acid.

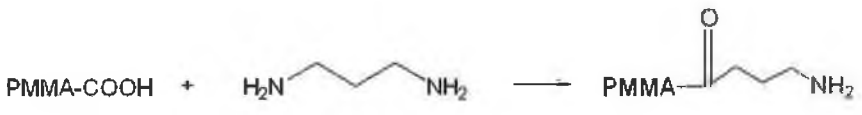


**Figure 6.16:** Formation of PMMA-COOH-$NH_2$.

containing 0.2 % w/v NaCl. The carboxyl-modified PMMA slides were immersed in this solution for 10 minutes, followed by thorough rinsing with de-ionised water and dried under a stream of nitrogen. The toluidine blue dye attached to the carboxyl groups present on the surface of the slide and was imaged using optical microscopy. Figure (a) shows an image of unmodified PMMA stained with toluidine blue and Figure (b) shows an image of carboxyl-modified PMMA stained with toluidine blue. There is a definite increase in carboxyl groups on the surface but the surface coverage is relatively uneven.

(a) (b)

**Figure 6.17:** Image of toluidine blue stained PMMA slides. Image (a) corresponds to unmodified PMMA. Image (b) corresponds to carboxyl-modified (via $O_2$ plasma) PMMA.

To facilitate the comparison of surface coverage of each of the immobilisation techniques, Cy5 dye was attached to the amine-terminated carboxyl-modified PMMA slides and analysed using the fluorescence scanner. A representative fluorescence image obtained is shown in Figure 6.18.

The fluorescence intensity values recorded using the carboxyl-modification via oxygen plasma method were comparable to those from both the hydroxyl-modification and amino-modification. However, as can be seen from Figure 6.18, a relatively uneven surface coverage of amines was obtained. This was in agreement with the toluidine blue test results. A possible explanation for the uneven coverage could lie with the two-step nature of the procedure: first the substrate is activated and subsequently the monomer is printed. As the radicals are highly reactive, several of them could react with one another to form non-reactive compounds before the monomer is printed. This would result in a lack of radicals in some parts of the substrate, leading to an uneven layer.

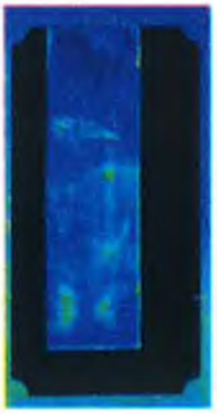

**Figure 6.18:** Fluorescence image of Cy5 dye immobilised on carboxyl-modified (via $O_2$ plasma) PMMA slide. Only the bottom portion of the slide was modified.

### 4. UV-cured Graft Polymerisation

The fourth modification strategy investigated was also based on graft polymerisation. In this case, UV irradiation was employed to promote the free radicals required for initiating the polymerisation process. The photon energy of UV light is high enough to excite and dissociate various organic chemical bonds and form free radicals on the polymer surface. These radicals subsequently react with activated oxygen species simultaneously generated through the photoexcitation of atmospheric oxygen molecules.

In this work, the initiator and monomer, acetophenone and methacrylic acid respectively, were mixed together and printed onto the PMMA surface. The initiator was then split using UV radiation, leaving each initiator fragment with one unpaired electron (free radical). As stated in Section 6.2.1, methacrylic acid contains a carbon-carbon double bond that is easily attacked by the free radical. This results in the addition of the free radical to the monomer. This process repeats itself, resulting in the formation of polymer chains, only terminating when two radical species form. The UV irradiation results in the formation of radicals, not only in the initiator but also on the PMMA substrate (both via the UV-irradiation and via a chemical reaction between the photoinitiator and the polymer substrate), resulting in the anchorage of the reactive layer to the PMMA surface [11, 12]. The process is illustrated in Figure 6.19.

As described in Section 6.2.1, amine groups were formed on the carboxyl-

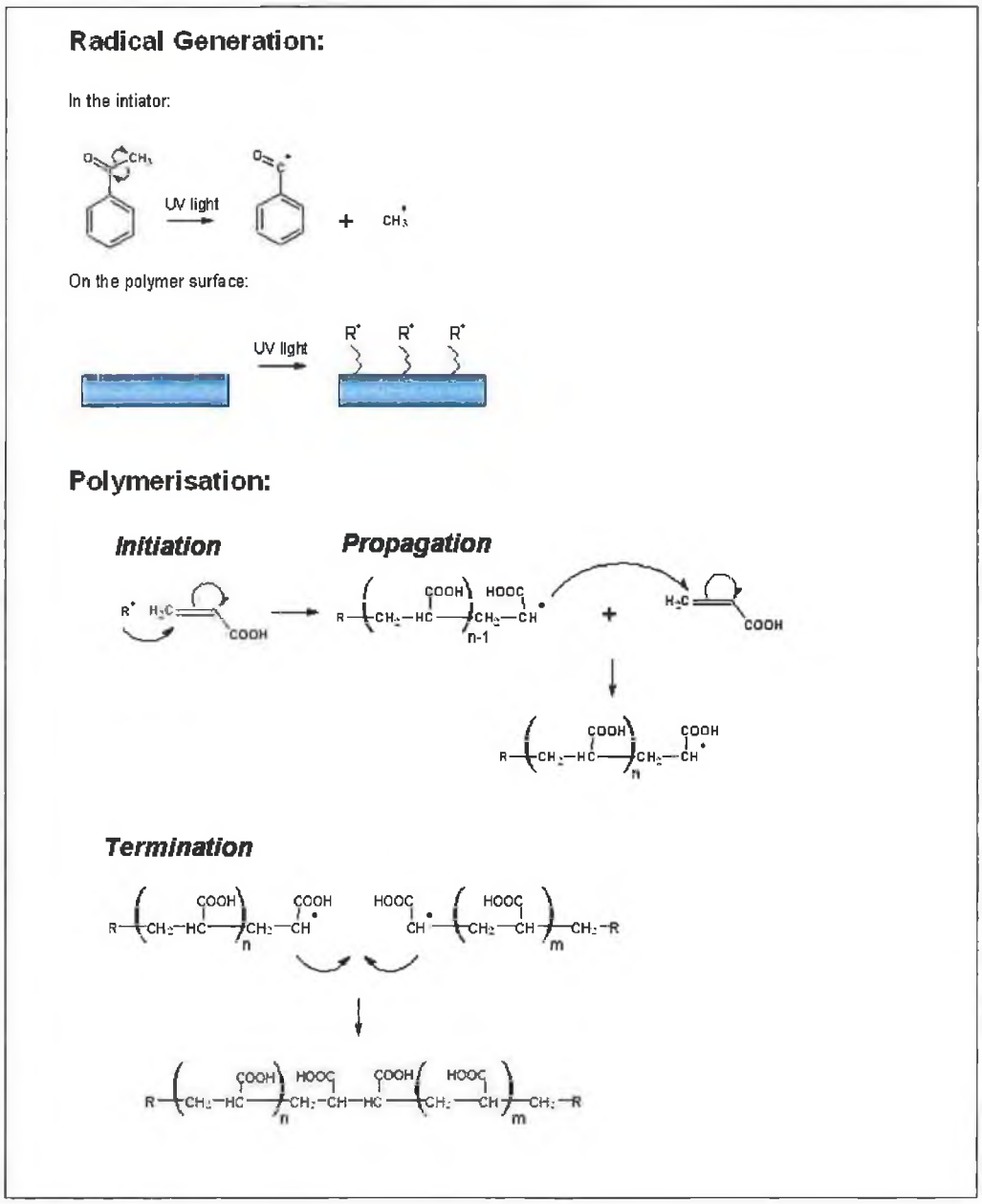


**Figure 6.19:** Mechanism of UV-cured graft polymerisation.

modified PMMA slides via immersion in a solution containing 1,3-diaminopropane and EDC (see Figure 6.16).

### Characterisation of UV-cured Graft Polymerisation Treated PMMA

The toluidine blue test described in Section 6.2.1 was repeated for the carboxyl-modified (via UV-cured graft polymerisation) PMMA slides. The toluidine blue dye attached to carboxyl groups present on the surface of the modified slides and was recorded using optical microscopy.

Examination of the stained slides showed a relatively even surface coverage of carboxyls on the UV-cured carboxylated PMMA and suggests that the UV-cured treatment produces a more homogenous surface carboxyl population than the $O_2$ plasma treatment.

To facilitate comparison between strategies, Cy5 dye was immobilised on the amine-terminated, carboxyl-modified PMMA slides. The labelled slides were subsequently examined using the fluorescence scanner and analysis showed a relatively homogenous surface coverage (see Figure 6.20). A table listing fluorescence intensity values for each of the strategies is included at the end of Section 6.2.1.

**Figure 6.20:** Fluorescence image of Cy5 dye immobilised on carboxyl-modified (via UV-cured graft polymerisation) PMMA slides. Only the bottom portion of the slide was modified.

The fluorescence intensity values obtained via this modification strategy were slightly higher than those recorded from the other strategies, with a relatively even amine surface coverage obtained. A possible explanation for this relatively

homogeneous surface coverage could be that, in this method, the monomer and initiator form an even layer before polymerisation. Polymerisation then occurs simultaneously from the layer to the surface and from the surface to the layer. This is in contrast to the plasma treatment method, where the polymerisation induced by the plasma treatment is rather anisotropic due to the presence of radicals only on the PMMA surface and the two-step process discussed previously.

**5. Silica-Modification**

The final modification strategy investigated was similar to the third and fourth, in that a grafted layer was covalently attached to the PMMA surface. However, in this case, a sol-gel layer, rather than a polymer, was grafted onto the PMMA surface. As explained in Section 5.2.4, the sol-gel process results in the formation of a glass at low temperatures. Therefore, following the formation of the sol-gel layer, well established glass chemistries could be employed to attach antibodies to the substrate surface.

A tetraethyl-orthosilicate (TEOS)-based sol was prepared by mixing TEOS, 0.1 N hydrochloric acid and ethanol absolute and leaving the solution to age overnight. An oxygen plasma was used to generate reactive groups/radicals on the PMMA surface. These treated slides were then coated with the TEOS-based sol via dip-coating, which, as explained in Section 5.3.2, is a process that involves the immersion and withdrawal of the slides from a sol. For this work, a dip-coating rate of 2 mm/s was employed, after which, the chips were cured at 70°C for 6 hours, resulting in a TEOS based layer approximately 500 nm thick.

In order to form amine groups on the surface of the TEOS-coated PMMA slides, the organosilane, 3-aminopropyltriethoxysilane, was employed (see Section 4.3.2 for information on organosilanes). After incubating the slides in this solution, amine functional groups were formed on the surface, as illustrated in Figure 6.21.

**Characterisation of Silica Modified-PMMA**

In order to compare amine surface coverage with that of each of the other immobilisation strategies, Cy5 dye was attached to the amine groups present on the


**Figure 6.21:** Reaction of TEOS-coated PMMA with organic amino-silane, to form PMMA-TEOS-$NH_2$.

surface of the PMMA-TEOS-$NH_2$ slides. After removing the slides from the solution they were washed and dried and the amine surface coverage was examined using the fluorescence scanner. A representative fluorescence image is shown in Figure 6.22.

**Figure 6.22:** Fluorescence image of Cy5 dye immobilised on PMMA slide via sol-gel coating. Sol-gel coated on bottom portion of slide only.

Compared to the previous strategies employed, a relatively high level of fluorescence was obtained using the silica-modified PMMA slides. However, the surface coverage was quite non-homogeneous. Mean fluorescence values obtained via each strategy are presented in Section 6.2.1.

### Attachment of Chains

The main aim of the surface modification was the effective immobilisation of antibodies. Work carried out by Hoffman et al. showed that antibody immobilisation directly onto a polymer surface can result in low levels of antigen binding due to steric crowding and restricted antibody movement [13]. They overcame this problem by employing molecular chain extensions. Antibodies attached via chains

should have greater freedom of movement, thus reducing the steric hindrance and thereby increasing the number of available antigen-binding sites. Hoffman et al. reported the greatest increase in antigen binding and sensor sensitivity when the molecular chains employed were greater than 20 atoms in length.

Therefore, in order to reduce the potential problems of steric hindrance and increase the number of available antigen binding sites, the use of molecular chain extensions was investigated. The chains were formed by immersing the PMMA slides with terminal $NH_2$ functionalities (PMMA-$NH_2$, PMMA-OH-$NH_2$, PMMA-COOH-$NH_2$, PMMA-TEOS-$NH_2$) in 0.2M carbonate buffer solution (pH9.0), to which succinic anhydride was added. The succinic anhydride reacted with the primary amine groups in a ring-opening process, creating an amide bond and forming a terminal carboxylate (see Figure 6.23). This solution was stirred overnight at room temperature to ensure all sites had reacted and the slides were subsequently rinsed with de-ionised water and dried under nitrogen.

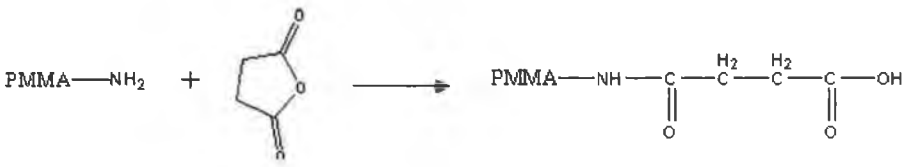


**Figure 6.23:** Formation of amide bond with terminal carboxylate.

As with each of the modification strategies described previously, the modified PMMA slides were immersed in 0.1 M phosphate buffer (pH7.0), to which EDC was added, followed by a 5 % solution of 1,3-diaminopropane in 0.1 M phosphate buffer (pH7.0). The terminal carboxylate reacted with the amines in the solution, creating an amide bond and forming a terminal amine group (see Figure 6.24). This reaction mixture was stirred at room temperature for 4 hours, after which the slides were rinsed with de-ionised water and dried under a stream of nitrogen.

This formation of a terminal carboxyl group, followed by the formation of a terminal amine group was repeated until a chain length away from the surface of the PMMA substrate of greater than 20 atoms was achieved. The final spacer was comprised of 26 atoms (approximately 32 $\AA$), as shown in Figure 6.25.

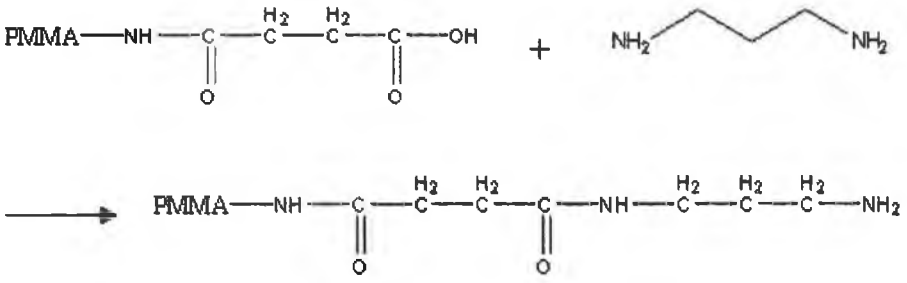


**Figure 6.24:** Formation of amide bond with terminal amine group.

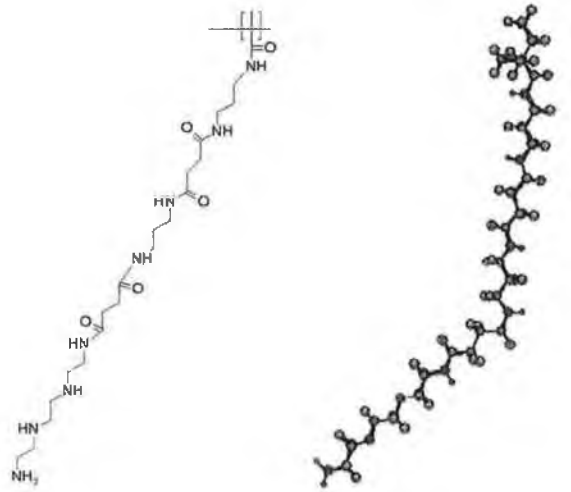


(a) (b)

**Figure 6.25:** (a) Structure of extended chains from surface of PMMA (b) Molecular model of extended chains from surface of PMMA, modelled using Chem-3D.

### Characterisation of PMMA with Chains Extensions

In order to complete the comparison, Cy5 dye was coupled to the PMMA slides modified with molecular chain extensions, terminating in amine groups. PMMA-$NH_2$, PMMA-OH-$NH_2$, PMMA-COOH-$NH_2$ (both $O_2$ plasma and UV-cured) and PMMA-TEOS-$NH_2$ slides were each immersed in 0.2M carbonate buffer solution (pH9.0), to which Cy5 dye was added. This solution was left at room temperature for 30 minutes, after which the slides were rinsed with de-ionised water and then dried under a stream of nitrogen.

Mean intensities for each immobilisation strategy (for both direct immobilisation and via molecular chain extensions) were calculated and are presented in

Table 6.1.

| Cy5 dye Immobilisation Strategy | Mean Intensity Direct (a.u.) | Mean Intensity Chains (a.u.) |
|---|---|---|
| Amino-modification | 23 ± 4 | 40 ± 3 |
| Hydroxyl-modification | 14 ± 7 | 16 ± 2 |
| Carboxyl-modification (via $O_2$ plasma) | 45 ± 14 | 28 ± 11 |
| Carboxyl-modification (UV-cured) | 61 ± 7 | 48 ± 2 |
| Silica-modification | 65 ± 16 | 20 ± 13 |

**Table 6.1:** Mean intensity values recorded from Cy5 dye coupled to PMMA slides using each of the immobilisation strategies, via both direct immobilisation and molecular chain extensions.

Analysis of the fluorescence images showed that there was no significant increase in fluorescence intensity when molecular chain extensions were employed, compared to when the Cy5 dye was attached directly to the modified slides. This was as expected, as the chains were employed specifically for use with the antibody immobilisation, to reduce the problems of steric hindrance and reduced antibody movement. As these are not major issues with the immobilisation of Cy5 dye, the chains were not expected to provide increased dye immobilisation.

### 6.2.2 Antibody Binding

Cy5-labelled anti-BSA antibodies were coupled to PMMA slides via each of the five immobilisation strategies described in Section 6.2.1, using both direct attachment and molecular chain extensions. The slides were analysed using the fluorescence scanner. Representative fluorescence images obtained for each slide are shown in Figure 6.26.

Mean intensities for each immobilisation strategy were calculated and are presented in Table 6.2.

Fluorescently-labelled antibodies were successfully immobilised via each of the five immobilisation strategies. Most of the strategies produced comparable levels of fluorescence signal, indicating that none was significantly better than the others in terms of signal level obtained.

In contrast to the immobilised Cy5 dye, a trend was observed with regards

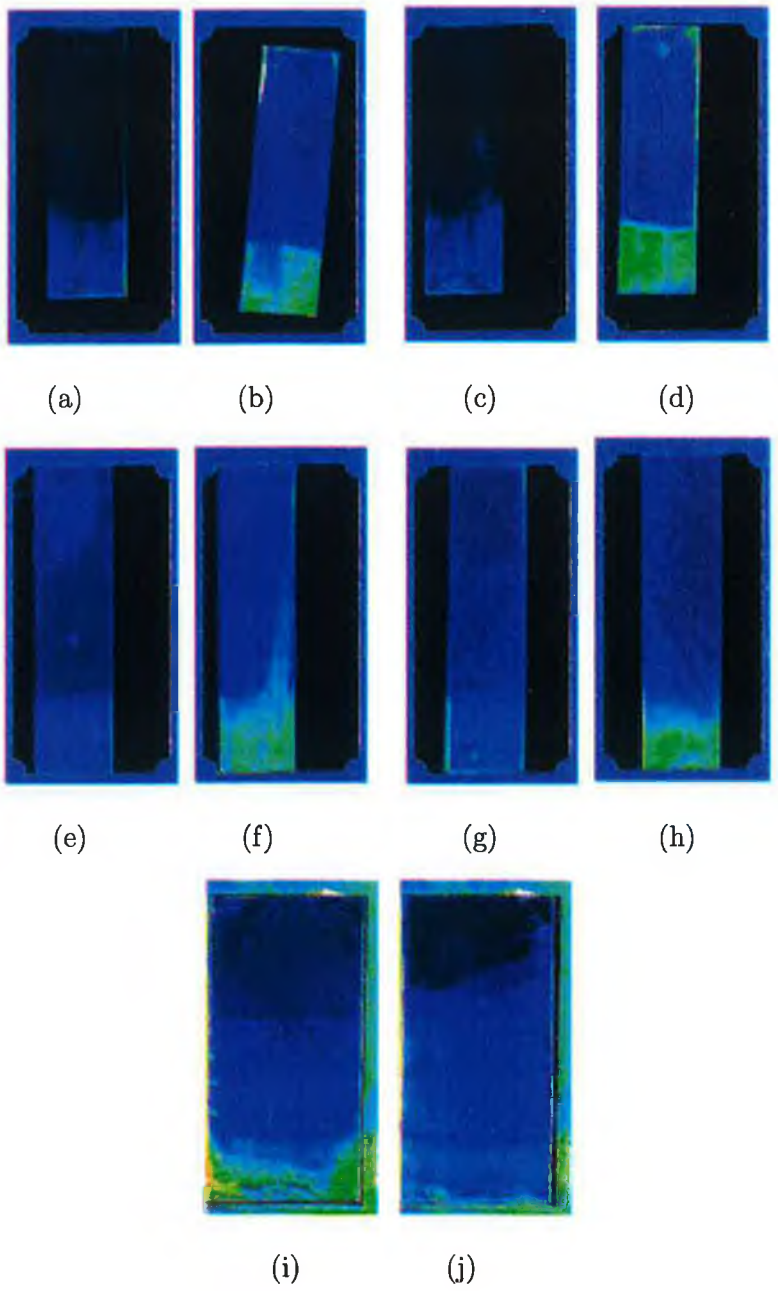


**Figure 6.26:** Fluorescence images of Cy5-labelled anti-BSA antibodies immobilised on PMMA slides. Figures (a) and (b) correspond to PMMA-$NH_2$ direct and chains respectively, (c) and (d) to PMMA-OH direct and chains, (e) and (f) to PMMA-COOH (via $O_2$ plasma) direct and chains, (g) and (h) to PMMA-COOH (UV-cured graft polymerisation) direct and chains and (i) and (j) to PMMA-TEOS direct and chains.

| Cy5 dye-Labelled Antibody Immobilisation Strategy | Mean Intensity Direct (a.u.) | Mean Intensity Chains (a.u.) |
|---|---|---|
| Amino-modification | 21 ± 4 | 80 ± 9 |
| Hydroxyl-modification | 26 ± 4 | 83 ± 4 |
| Carboxyl-modification (via $O_2$ plasma) | 22 ± 3 | 79 ± 4 |
| Carboxyl-modification (UV-cured) | 37 ± 3 | 84 ± 11 |
| Silica-modification | 44 ± 19 | 43 ± 6 |

**Table 6.2:** Mean intensity values (a.u.) recorded from Cy5-labelled anti-BSA antibodies coupled to PMMA slides using five separate immobilisation strategies, via both direct immobilisation and molecular chain extensions.

to higher intensities of fluorescence from antibodies attached via molecular chain extensions when compared to antibodies attached directly to the surface of the PMMA slides. This was as expected, as direct attachment of antibodies would imply restricted movement of the antibody and greater steric crowding, thus lowering the concentration of antibodies at the substrate surface. Antibodies further from the surface should have greater freedom of movement, increasing the potential for enhanced surface coverage. However, immobilisation of antibodies via chains using the TEOS immobilisation strategy resulted in a decrease in the fluorescence signal recorded when compared to that from the direct immobilisation. A possible explanation for this result is that, due to the thickness of the TEOS coating on the PMMA slide, when the dye is bound via molecular extensions it so far from the surface of the substrate that it is no longer in the focus of the fluorescence scanner. This is a likely explanation as the TEOS film is already of the order of 500 nm thick.

Due to the lack of significant variation in surface homogeneity of the labelled antibodies, it was necessary to employ alternative selection criteria in the choosing of an immobilisation strategy for use with the polymer-based immunosensor. Ultimately, the UV-cured graft polymerisation plus chains strategy was selected. This was due to its relatively simple protocol, the non-toxicity of the chemicals required for its implementation and the fact that it is a generic modification strategy that is independent of the polymer employed.

### 6.2.3 Assay on Polymer Substrate

It was necessary to validate the use of the UV-cured graft polymerisation and chains method as an effective antibody immobilisation strategy for a polymer-based immunosensor. Therefore, a BSA/anti-BSA assay was carried out using the sensor system described in Section 4.5, with the glass substrate substituted by a planar PMMA slide.

The PMMA slide was coated with a solution of methacrylic acid and acetophenone and UV-radiated for one hour. Following the radiation, the slide was treated with EDC and 1,3-diaminopropane, resulting in the formation of amines on the surface.

Subsequently, a BSA/antiBSA sandwich assay was carried out as described in Section 4.4, with capture anti-BSA antibodies immobilised on the polymer substrate and decreasing concentrations of BSA passed above. The excitation, detection and analysis systems employed were the same as those employed with the glass substrate (see Section 4.5).

A full dose response curve was successfully obtained and is shown in Figure 6.27.

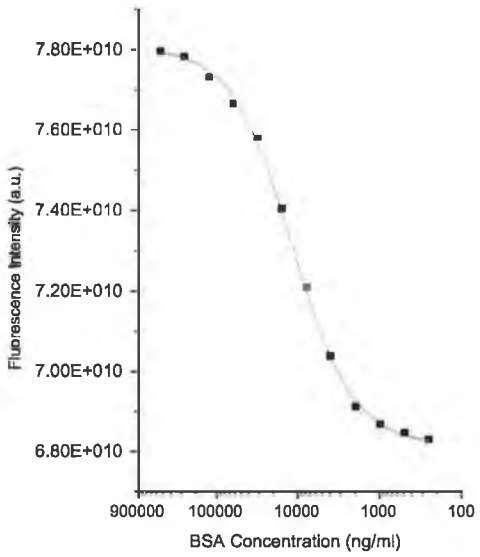


**Figure 6.27:** Dose response curve for BSA/anti-BSA assay (repeated three times), obtained using PMMA-based immunosensor, employing the UV-cured graft polymerisation antibody immobilisation strategy.

As with the glass substrate-based immunosensor described in Chapter 4, as the antigen concentration decreased, so too did the fluorescence intensity. A comparable working range of greater than 100,000 ng/ml of antigen to 100 ng/ml was attained. As before, the data was fitted to a sigmoidal four-parameter logistic equation, with $R^2 = 0.9926$ [14]. The minimal detectable signal (MDS) was calculated from the mean zero response plus $3\sigma$, where $\sigma$ represents the standard deviation and the mean zero response is the intensity value recorded when no antigen is present. The corresponding limit of detection for BSA was approximately 300 ng/ml. This was slightly higher than that achieved using the glass substrate-based immunosensor, which provided a limit of detection of 150 ng/ml. Similar to the glass-based immunosensor, the MDS of the system coincided with the lowest concentrations of BSA detected. Though this meant that it was not possible to state if the limit of detection was due to the sensitivity of the antibodies or due to the MDS of the system, the aim of proving that the UV-cured graft polymerisation and chains method was a viable antibody immobilisation strategy was successfully achieved.

### 6.2.4 Summary

Replacement of the planar glass substrate of the immunosensor described in Chapter 4 with the structured polymer platform presented in Chapter 5 meant that the antibody to glass immobilisation techniques employed previously were no longer applicable. Antibody to polymer immobilisation is a relatively new area of research and consequently, no standardised strategy has been adopted yet. Therefore, several different immobilisation techniques were investigated. Antibodies were successfully immobilised on a polymer substrate via five separate modification strategies, namely, amino-modification, hydroxyl-modification, carboxyl-modification via oxygen plasma, carboxyl-modification via UV-cured graft polymerisation and silica-modification. The effect of molecular chain extensions was also investigated and applied to each of the five strategies.

No significant difference in antibody surface coverage was recorded using each of the methods. Therefore, due to its ease of use and the non-toxicity of the chemicals employed, the UV-cured graft polymerisation plus chains method was selected as the immobilisation strategy for use with the enhanced immunosensor.

To demonstrate its effectiveness, a full BSA/anti-BSA assay was carried out on a planar polymer substrate. A limit of detection for BSA of 300 ng/ml was obtained, which was comparable to the limit of detection for BSA obtained using the planar glass immunosensor.

## 6.3 Patterning

After the antibody immobilisation strategy had been selected, the next area that required development before the optimised immunosensor could be completed was that of the patterning techniques.

### 6.3.1 Pin-Printing

The initial immunosensor (described in Chapter 4) was based on a planar glass substrate and was patterned using an Affymetrix Arrayer. However, the Arrayer is designed specifically for the patterning of arrays of spots onto planar substrates, meaning that it was not readily adaptable for use with the structured substrates of the optimised immunosensor.

In order to efficiently pattern the structured substrates a new patterning technique had to be employed. Several techniques were investigated and a Genomic Solutions OmniGrid Micro Pin-Printer was chosen as the most suitable for this application (see Figure 6.28). The main advantage of the Pin-Printer over the Arrayer was the ease of the z-axis control, which allowed the frustrated cone structures to be easily incorporated into the pattern.

The Pin-Printer is designed to transfer solution from either a 96 or a 384 well plate to defined locations on the substrates. Each part of the printing process is programable, including the wash and dry functions, meaning that once a patterning program was written, it could be run completely automatically, without any manual input required. Split pins, supplied by Telechem (Sunnyvale, CA, USA), were employed to deposit the antibody solutions onto the substrate surface. These pins have defined uptake channels and flat tips, which facilitate the formation of thin drops (approximately 25 $\mu$m) on the tips. The drop is gently transferred to the substrate without the pin coming into contact with the substrate (as illustrated in Figure 6.29).

**Figure 6.28:** Genomic Solutions OmniGrid Micro Pin-Printer.

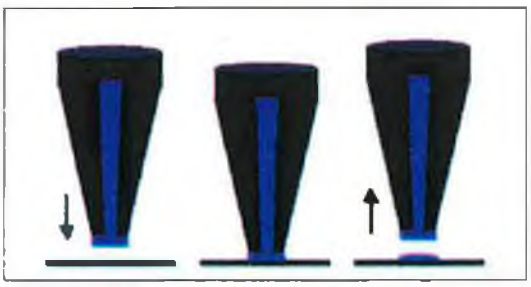

**Figure 6.29:** Split pin printing mechanism.

The split pins provide superior spot size consistency compared to solid pins, with the mean spot diameter of the spots in the work presented here equal to $50\,\mu\text{m} \pm 10\,\mu\text{m}$. The diameter of the spots was affected by several controllable printing parameters such as humidity, dwell time and fill time. Larger spot diameters (100's of $\mu$ms) were achieved by reducing the separation between the spots sufficiently for them to merge to form a single large spot.

The pin-printer was employed to pattern the first level of the antibody assay. Applying the UV-graft polymerisation modification strategy described in Section 6.2.1, $300\,\mu\text{m}$ diameter methacrylic acid spots were formed on the top surface of the optimised immunosensor's frustrated cones. This meant that, after blocking the rest of the immunosensor substrate, each subsequent layer of the antibody assay should attach only at these defined locations.

### 6.3.2 Microfluidics

The pin-printer was used to precisely define the location of the first layer of the antibody assay. Microfluidics were employed to pass the subsequent layers over the immunosensor surface, allowing them to bind to the previous layer. They also facilitated the necessary washing and blocking steps.

The initial planar immunosensor employed a reuseable PDMS flowcell to introduce the antibody assay solutions (see Section 4.4.2). In the case of the optimised immunosensor, PMMA flowcells were employed. The polymer immunosensor was fabricated via micro-injection moulding (as described in Section 5.2.3), with a flowcell incorporated into the design of the brass master. Thus, both substrates and flowcells could simultaneously be fabricated quickly and simply, further leading to a complete single-use, disposable immunosensor biochip.

Once the initial layer had been printed onto the tops of the frustrated cone structures, the immunosensor substrate and flowcell were sealed using pressure sensitive adhesive (PSA). A water-tight seal was formed by simply applying the PSA to the edges of the flowcell and bringing it firmly into contact with the substrate for 5mins.

Similar to the set-up employed for the planar immunosensor (described in Section 4.4.2), a peristaltic pump was employed to pass the antibody assay solutions through the polymer biochip.

## 6.4 Experimental and Analysis Systems

The experimental and analysis systems employed for use with the planar immunosensor (see Section 4.5) were both modified for use with the structured optimised immunosensor. The major difference between the two systems was the replacement of evanescent wave excitation with direct excitation of the biochip. This greatly simplified the optics, removing the need for the line generator, cylindrical lens and the precision alignment required for coupling and evanescent wave generation. The 635nm laser diode, filter and cooled CCD camera were all retained, with only the GRIN lens array being replaced with a variable focus lens. A schematic of the set-up is shown in Figure 6.30.

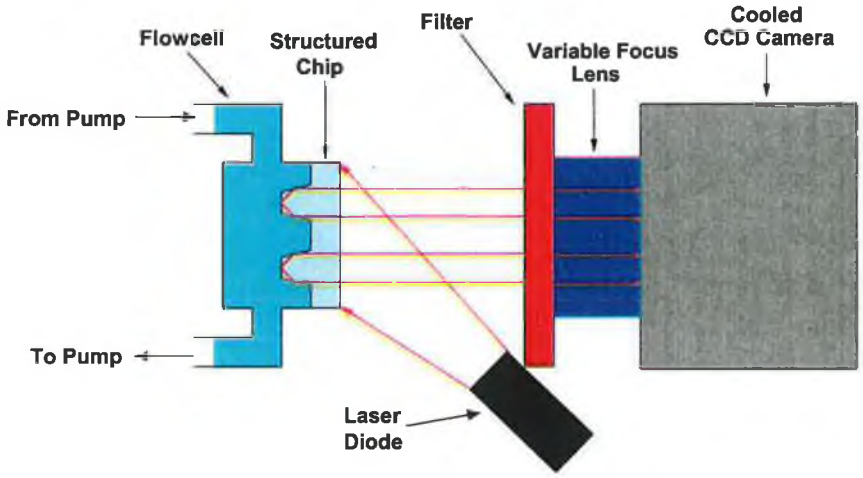


**Figure 6.30:** Schematic of excitation and detection system modified for use with the structured optimised immunosensor.

The custom-written image analysis program employed with the planar immunosensor system (see Section 4.5.3) was modified in-house to include a Visual Basic Interface. The previous version facilitated the comparison of selected rectangular areas of different images to be compared. As the frustrated cone structures resulted in circular intensity profiles, the program was updated (in-house) to allow circular areas of the recorded images to be selected and compared in terms of intensity.

## 6.5 Sensor Performance

### 6.5.1 System Validation

In order to test each of the procedures and systems described in this chapter, a bovine serum albumin (BSA)/anti-BSA competitive assay was carried out on the structured biochips. For ease of comparison, the same stock solutions employed in Section 4.6 were also employed here. The surface of the structured biochips were modified using the graft polymerisation strategy described in Section 6.2.1. Anti-BSA antibodies were subsequently patterned onto the top of the frustrated cones (via molecular chains) using the Genomic Solutions OmniGrid Micro Pin-Printer (see Section 6.3.1). Known quantities of Cy5-labelled and unlabelled BSA were passed above the structured biochip and competed for the antibody binding sites (see Section 2.5.3 for more information on competitve assays). Unbound BSA molecules were washed away and labelled BSA bound to the surface of the biochip were excited using a 635nm laser diode. Fluorescence emitted from the bound labelled BSA molecules was recorded using the CCD camera-based detection system described in the previous section. The custom-written analysis program was used to correlate pixel intensities of the fluorescence images with antigen (BSA) concentration. A representative fluorescence image is shown in Figure 6.31, illustrating the typical spot and ring profile obtained.

**Figure 6.31:** Representative fluorescence image obtained using the enhanced immunosensor.

The spot in the center of the image shown in Figure 6.31 corresponds to the fluorescence emitted from labelled BSA molecules immobilised on the top of the cone. The ring profile corresponds to the SC fluorescence that was redirected onto

the CCD camera by the frustrated cones, which would have been undetected if a planar substrate had been employed. The recording of these images verified that the assay had been successfully carried out and that each of the procedures and systems described in this chapter worked effectively.

### 6.5.2 Dose Response Curve

In order to investigate the sensor performance a full dose response curve was obtained using the enhanced immunosensor. Varying concentrations of Cy5-labelled BSA were mixed with a known concentration of unlabelled BSA. Competitive assays were then carried out on the optimised immunosensor using these solutions. For each concentration of Cy5-labelled BSA, a different fluorescence intensity was recorded. These intensities were plotted against concentration in order to produce the dose response curve shown in Figure 6.32.

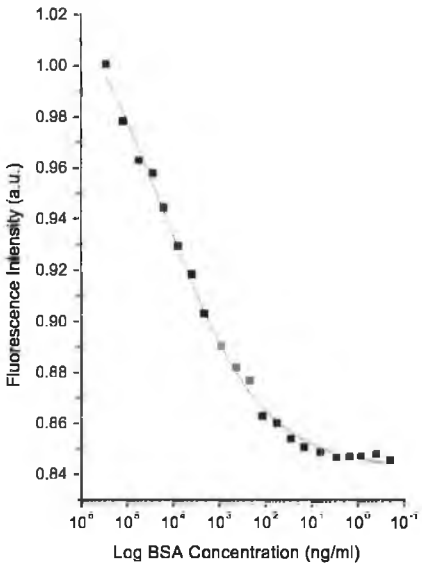


**Figure 6.32:** Dose response curve for BSA/anti-BSA assay carried out using the enhanced immunosensor (assay repeated three times).

As occurred in the data analysis of the planar immunosensor described in Chapter 4, the data was fitted to a sigmoidal four-parameter logistic equation, with $R^2 = 0.9969$ [14]. A minimal detectable signal (MDS) (calculated from the mean zero response plus $3\sigma$) of 0.2745 was calculated. This was significantly lower

than the signal obtained for the lowest BSA concentration measured. Therefore, unlike the planar immunosensor, using the enhanced immunosensor it was possible to determine the antibody sensitivity, as opposed to the limit of detection of the system. The limit of detection for BSA of this stock of antibodies was calculated as approximately 7 ng/ml (mean final plateau response plus $3\sigma$). Both this limit of detection and the working range obtained are comparable to similar immunosensors detailed elsewhere [15, 16]. Furthermore, it should be noted that due to the low MDS obtainable, by employing antibodies with higher sensitivities, the enhanced immunosensor provides the capability to detect significantly lower concentrations of antigens.

## 6.6 Conclusions

This chapter described the integration of the structured chip developed in Chapter 5, with the planar immunosensor presented in Chapter 4. A major challenge of this work resulted from the fact that the antibody immobilisation now took place on a polymer substrate as opposed to a glass substrate. As explained in Chapter 1, this is a very new area of research and consequently, no standard immobilisation strategy for polymer has been adopted.

Therefore, five separate covalent antibody to polymer immobilisation strategies were investigated for use with the immunosensor and the effect of molecular chain linkers was also examined. The UV-cured graft polymerisation strategy was selected and its effectiveness validated by obtaining a full dose response curve using a polymer-based immunosensor.

The patterning, excitation, detection and analysis systems developed for the planar immunosensor presented in Chapter 4 were each optimised for use with the structured polymer platforms. A BSA/anti-BSA assay was subsequently performed, validating each of the components of the optimised immunosensor and a detection limit for BSA of 7 ng/ml was obtained, which is comparable to similar published immunosensors. Most importantly, the minimum detectable signal was significantly lower than that of the planar immunosensor. Consequently, this enhanced immunosensor has the capacity to detect significantly lower concentrations of antigens. This has important implications in the area of medical diagnostics, for example, where often only small quantities of analyte are available and there

exists the need to detect toxins that are fatal at low doses.

# Bibliography

[1] A. Akkoyun and U. Bilitewski, "Optimisation of glass surfaces for optical immunosensors," *Biosensors and Bioelectronics*, vol. 17, no. 8, pp. 655–664, 2002.

[2] C. Baker, K. Green, M. van der Grinten, P. Iaydjiev, S. Ivanov, S. Al-Ayoubi, P. Harris, J. Pendlebury, D. Shiers, and P. Geltenbort, "Development of solid-state silicon devices as ultra cold neutron detectors," *Nuclear Instruments and Methods in Physics Research Section A: Accelerators, Spectrometers, Detectors and Associated Equipment*, vol. 487, no. 3, pp. 511–520, 2002.

[3] S. Soper, A. Henry, B. Vaidya, M. Galloway, M. Wabuyele, and R. McCarley, "Surface modification of polymer-based microfluidic devices," *Analytica Chimica Acta*, vol. 470, pp. 87–99, 2002.

[4] C. Pouchert, *The Aldrich Library of Infrared Spectra.* Milwaukee: Aldrich Chemical Company, ed.3. ed., 1981.

[5] M. Omastova, J. Pavlinec, J. Pionteck, F. Simon, and S. Kosina, "Chemical preparation and characterization of conductive poly(methyl methacrylate)/polypyrrole composites," *Polymer*, vol. 39, no. 25, pp. 6559–6566, 1998.

[6] G. Fang and N. Liu, "Determination of eight essential amino acids in mixtures by chemometrics-spectrophotometry without separation," *Analytica Chimica Acta*, vol. 445, no. 2, pp. 245–253, 2001.

[7] P. Charlesworth, *Polymers.* University Chemistry 1 Michigan: Michigan Technology University, 2004.

[8] J. Terlingen, *Functionalization of Polymer Surfaces.* Europlasma, 2004.

[9] J. Chai, F. Lu, B. Li, and D. Kwok, "Wettability interpretation of oxygen plasma modified poly(methyl methacrylate)," *Langmuir*, vol. 20, no. 25, pp. 10919–10927, 2004.

[10] W. Hinrichs, H. ten Hoopen, M. Wissink, G. Engbers, and J. Feijen, "Design of a new type of coating for the controlled release of heparin," *Journal of Controlled Release*, vol. 45, no. 2, pp. 163–176, 1997.

[11] A. Plonka, J. Bednarek, and K. Pietrucha, "Reaction dynamics in glass transition region: Propagating radicals in ultraviolet-irradiated poly(methyl methacrylate)," *Journal of Chemical Physics*, vol. 104, no. 13, pp. 5279–5283, 1996.

[12] B. Ranby, W. Yang, and O. Tretinnikov, "Surface photografting of polymer fibers, films and sheets," *Nuclear Instruments and Methods in Physics Research Section B-Beam Interactions With Materials and Atoms*, vol. 151, no. 1-4, pp. 301–305, 1999.

[13] W. Hoffman and D. O'Shannessy, "Site-specific immobilization of antibodies by their oligosaccharide moieties to new hydrazide derivatized solid supports," *Journal of Immunological Methods*, vol. 112, no. 1, pp. 113–120, 1988.

[14] M. Ngundi, L. Shriver-Lake, M. Moore, M. Lassman, F. Ligler, and C. Taitt, "Array biosensor for detection of ochratoxin a in cereals and beverages," *Analytical Chemistry*, vol. 77, no. 1, pp. 148–154, 2005.

[15] M. Diaz-Gonzalez, D. Hernandez-Santos, M. Gonzalez-Garcia, and A. Costa-Garcia, "Development of an immunosensor for the determination of rabbit IgG using streptavidin modified screen-printed carbon electrodes," *Talanta*, vol. 65, no. 2, pp. 565–573, 2005.

[16] P. Lin, J. Feng, H. Zheng, H. Yang, and J. Xu, "Preparation of pH-sensitive polymer by thermal initiation polymerization and its application in fluorescence immunoassay," *Talanta*, vol. 65, no. 2, pp. 430–436, 2005.

# Chapter 7

# Conclusions

The need for detection of potential biohazards exists in a wide range of areas, including medical diagnostics, food safety, environmental pollution control and biological warfare agent detection. Biosensors are being developed to fulfill this need, with the selectivity and sensitivity provided by antibodies and their corresponding antigens making them attractive sensing agents. As immunosensor research is still at an early stage, they are not yet fully established in these areas and there is considerable further development required.

Fluorescence-based immunosensors offer several advantages over alternative transducer types, including ease of use, range of application areas and lower costs. Optimisation of these sensors requires a truely multidisciplinary approach, with their fabrication and operation combining areas of biology, chemistry and physics.

The first aim of this thesis was to integrate these fields through the establishment of the techniques and systems required to produce an effective immunosensor. Chapter 4 described how this objective was achieved and provided details of the development of strategies for antibody preparation, immobilisation, patterning, excitation, detection and validation.

Following the establishment of these techniques, the next focus of the work was on enhancement strategies. Consequently, research was carried out on the enhancement of fluorescence signal capture and the discrimination between surface and bulk fluorescence. The ability to detect low fluorescence signals is extremely desirable due to the fact that many analytes are toxic at low concentrations, with often only small quantities of antibodies or analytes available. The ability to

distinguish between surface and bulk fluorescence would eliminate the need to remove fluorescent bulk solution, thus simplifying the immunosensor design and operation. This in turn would reduce the cost and operation time, allowing the performance of rapid testing by unskilled operators (e.g. in the doctor's surgery).

Chapter 5 described the completion of the second objective of this work, namely, the experimental verification of the theoretical prediction that fluorescence signals can be increased via re-direction of substrate-confined modes and also that it is possible to discriminate between surface and bulk fluorescence. Based on this work, structured polymer chips were designed and fabricated. The chips were shown to significantly increase the fluorescence capture of ruthenium-complex dye-doped sol-gel, with mean enhancement factors of 35 achieved. It was demonstrated that the ability to partially discriminate between surface and bulk fluorescence was inherent in these chips but complete discrimination was not possible with this design. Following the demonstration of the fluorescence signal enhancement, the third aim of this thesis was to incorporate this structured chip with the systems presented in Chapter 4, to produce an enhanced immunosensor.

There were several challenges to overcome in the integration of the structured chip with the techniques developed in Chapter 4. The initial immunosensor was based on a glass substrate. However, the structured chips were formed from polymer, which meant that the antibody immobilisation strategy described in Chapter 4 was not applicable to this substrate. The area of antibody to polymer immobilisation is an extremely new area of research and consequently, no standard immobilisation strategy has been adopted as of yet. Therefore, several separate antibody immobilisation strategies were investigated for use with the structured polymer chips. Chapter 6 detailed the implementation and characterisation of each of these strategies and demonstrated the effect of molecular chain extensions. UV-cured graft polymerisation (plus chains) was selected as the immobilisation strategy of choice and was validated through the successful attainment of a full dose response curve for BSA/antiBSA. The adaptation of each of the other systems for use with the structured polymer chip was also detailed in this chapter. Finally, validation of the optimisations and of the enhancement capabilities of the chip were demonstrated via the completion of a BSA/antiBSA assay. A working range and limit of detection for BSA comparable to those of similar published immunosensors was obtained and enhanced fluorescence signal

capture was achieved, with the minimum detectable signal recorded being lower than that of the planar glass-based immunosensor. As stated previously, this ability to increase the fluorescence capture signal has important implications for sensing applications where analytes are toxic in low concentrations or are only available in small quantities, with these situations occurring in a wide range of areas including health care, food safety and early-warning biological warfare agent detection.

The next stage of this work will involve the adaptation of the structured chips to provide complete discrimination of surface versus bulk fluorescence. This will necessitate the use of parabolic, as oppose to conical, structures. As a result, the associated systems, such as the patterning, excitation and detection systems, will require adaptation. The advantages of this discrimination are referred to above and include higher sensitivity and faster test times.

The evolution to polymer moulded microfluidic components will be a natural progression for this work and will facilitate the development of an ultimately portable immunosensor system. Also, due to the numerous advantages it displays over other polymers, including very low background fluorescence and excellent machinablility, Zeonor (Zeon Chemicals L.P., Louisville) will replace PMMA as the substrate polymer.

Further research will be carried out in the area of antibody to polymer immobilisation strategies. A single-step immobilisation strategy using sol-gel-based tunable refractive index films will be researched, which will further simplify the system and increase its application flexibility. Antibody orientation techniques will be developed in order to significantly increase the antigen-binding capacity of the immunosensor. Possible strategies include biotinylation of carbohydrate on the Fc portion of the antibody or cleaving of antibody fragments and immobilising via the available thiol group.

Due to the fact that this is a relatively new area of research and that the need for diagnostics is increasing rapidly, it is predicted that immunosensor research will expand significantly during the next few years. Thus, both the completed work presented in this thesis and the future developments referred to, are relevant and timely and have the potential to have considerable impact in this area.

# List of publications and conference presentations

## Oral presentations

1. "Novel Polymer Platform for Enhanced Biochip Performance", Opto Ireland, April 4-6 2005, Dublin, Ireland.

2. "Plasmonic enhancement of fluorescence for sensor applications", Europt(r)ode VII, April 4-7 2004, Madrid, Spain (presented by supervisor).

3. "Development of a fluorescence-based biochip for multianalyte immunosensing", Sensors and Their Applications XII, September 2-4 2003, Limerick, Ireland.

4. "Groundwater pollutant detection using a three detector-based sensor", ASCOS, September 24-28 2000, Rogaska Slatina, Slovenia (awarded 1st prize).

## Poster presentations

1. "Fluorescence-based biochip for multianalyte immunosensing", Institute of Physics Spring Weekend, April 11-13 2003, Westport, Ireland; BOC Gases poster competition, Feb 27 2003, Dublin, Ireland (awarded 3rd prize); Opto Ireland, September 5-6 2002, Galway, Ireland; Europt(r)ode II, April 7-10 2002, Manchester, England.

2. "Immunosensing through use of Fluorescence Capture", Institute of Physics Irish Branch Annual General Meeting, April 14-16 2000, Tralee, Ireland.

3. "Applications of Soft Lithography in the Optical Sensing Domain", Europt(r)ode V, April 16-19 2000, Lyon - Villeurbanne, France.

4. "Biosensing through Waveguiding and Fluorescence Imaging", BOC Gases poster competition, 2000, Dublin, Ireland (awarded 2nd Prize).

## Peer-Reviewed Publications

1. R. Blue, N. Kent, L. Polerecky, H. M. McEvoy, D. Gray, and B. D. MacCraith, "Novel Platform for Enhanced Detection Efficiency in Luminescence-based Sensors", *Electronic Letters*, Vol. 41, No. 12, 2005.

2. O. Stranik, H.M. McEvoy, C. McDonagh and B.D. MacCraith, "Plasmonic enhancement of fluorescence for sensor applications", *Sensors and Actuators B*, Vol. 101, No. 1, pp.148-153, 2005.

## Conference Proceedings

1. H. M. McEvoy, R. Blue, N. Kent, L. Polerecky, C. McDonagh, B. D. MacCraith, "Novel Polymer Platform for Enhanced Biochip Performance", Opto Ireland 2005: Optical Sensing, *Proc. SPIE*, In Press (accepted March 2005).

2. H. M. McEvoy, P.P. Dillon, C. McDonagh, B. D. MacCraith, R. O'Kennedy, "Development of a fluorescence-based biochip for multianalyte immunosensing", *Sensors and their Applications XII Conference Proceedings*, 2003.